ORGANIC SEMICONDUCTOR BULK HETEROJUNCTION DIODES WITH LOW DARK CURRENT FOR PHOTOVOLTAIC, PHOTODETECTION, AND SCINTILLATOR-FREE IONIZING RADIATION DETECTION APPLICATIONS

A Dissertation
Presented to
The Academic Faculty

by

Talha Mansur Khan

In Partial Fulfillment
of the Requirements for the Degree
Doctor of Philosophy in the
School of Electrical and Computer Engineering,
College of Engineering

Georgia Institute of Technology

May 2016

ORGANIC SEMICONDUCTOR BULK HETEROJUNCTION DIODES WITH LOW DARK CURRENT FOR PHOTOVOLTAIC, PHOTODETECTION, AND SCINTILLATOR-FREE IONIZING RADIATION DETECTION APPLICATIONS

Approved by:

Dr. Bernard Kippelen, Advisor
School of Electrical and Computer Engineering
Georgia Institute of Technology

Dr. Azad Naeemi
School of Electrical and Computer Engineering
Georgia Institute of Technology

Dr. Linda Milor
School of Electrical and Computer Engineering
Georgia Institute of Technology

Dr. Albert B. Frazier
School of Electrical and Computer Engineering
Georgia Institute of Technology

Dr. Samuel Graham
School of Mechanical Engineering
Georgia Institute of Technology

Date Approved: March 28, 2016

To Ab and Mama

ACKNOWLEDGEMENTS

First and foremost, all praise and gratitude belongs to Allah. None of this would have been possible without the prayers and sacrifices of my parents, Dr. Azhar Mansur Khan, and Dr. Naila Azhar. They instilled in me from early childhood, that there was no room for compromise when it came to education. My father, himself a Georgia Tech PhD recipient, expected nothing less from me. I also owe a great deal of gratitude to my sisters, Amna and Sarosh. It goes without saying that I am indebted to my wife, Toni Lynn Cliett, for her endless support.

I would also like to express my sincere appreciation to my doctoral advisor, Dr. Bernard Kippelen. His exceptional technical knowledge and emphasis on a sound approach toward experimental research are qualities that made him an effective doctoral advisor. In addition, he maintained a research laboratory flush with equipment with broad capabilities that aided me tremendously in conducting experimental research. During my graduate studies, I never had to worry about funding, which is a testament to Bernard's leadership and running of this research group.

Special thanks are due to Dr. Linda Milor and Dr. Samuel Graham for serving on my reading committee, as well as Dr. Albert B. Frazier and Dr. Azad Naeemi for serving on my doctoral dissertation defense committee.

I also sincerely appreciate the assistance of our research scientist, Dr. Canek Fuentes-Hernandez who was always available to answer my scientific queries, and provide valuable guidance on experiments, presentations, and papers.

In addition, I would like to acknowledge the support of our administrative managers Angela Hughes and Tina Moseley for ensuring that operations ran smoothly.

Finally, I have had the pleasure of making the acquaintance of numerous colleagues during my doctoral tenure from whom I have learned a great deal, and would like to recognize Dr. Dengke Cai, Dr. Hyeunseok Cheun, Mr. Sangmoo Choi, Dr. Seungkeun Choi, Ms. Wen-Fang Chou, Dr. Claudiu Cirloganu, Dr. Amir Dindar, Mr. Alfred Ernst, Dr. Mathieu Fenoll, Dr. Michael Gaj, Dr. Wojciech Haske, Dr. James Hsu, Dr. Do Kyung Hwang, Dr. Jungbae Kim, Dr. Keith Knauer, Mr. Vladimir Kolesov, Mr. Felipe Larrain, Dr. Ehsan Najafabadi, Dr. William Potscavage, Mr. Victor Rodriguez, Dr. Asha Sharma, Dr. Jae Won Shim, Dr. Sanjeev Singh, Mr. Sinan Sutcu, Dr. Shree Prakash Tiwari, Mr. Lukas Wagner, Mr. Cheng-Yin Wang, Ms. Amanda West, Dr. Minseong Yun, Ms. Xiaoqing Zhang, and Dr. Yinhua Zhou.

TABLE OF CONTENTS

Page

LIST OF TABLES

Page

LIST OF FIGURES

Page

LIST OF ABBREVIATIONS AND SYMBOLS

Al	Aluminum
Å	Angstrom
R_PA	Area-Scaled Parallel Resistance
R_SA	Area-Scaled Series Resistance
k	Boltzmann Constant
BHJ	Bulk Heterojunction
CdTe	Cadmium Telluride
Ca	Calcium
CIGS	Copper Indium Gallium Selenide
CuPc	Copper Phthalocyanine
J	Current Density
J_{MPP}	Current Density at the Maximum Power Point
EMF	Electromotive Force
q	Elementary Charge
PEIE	Ethoxylated Polyethylenimine
EQE	External Quantum Efficiency
FF	Fill Factor
GW	Giga Watt
Au	Gold
HIT	Heterojunction with Intrinsic Thin Layer
HOMO	Highest Occupied Molecular Orbital
HCl	Hydrochloric Acid
S:H	Hydrogenated Amorphous Silicon

ICBA	Indene C_{60}-Bisadduct
ITO	Indium Tin Oxide
P_{in}	Input Power
IPES	Inverse Photoelectron Spectroscopy
IE	Ionization Energy
LiF	Lithium Fluoride
LUMO	Lowest Unoccupied Molecular Orbital
MgPc	Magnesium Phthalocyanine
mA cm^{-2}	Milliampere per Square Centimeter
mW cm^{-2}	Milliwatt per Square Centimeter
MoO_3	Molybdenum Oxide
NiO	Nickel Oxide
HNO_3	Nitric Acid
Ω	Ohm
V_{OC}	Open-Circuit Voltage
OPV	Organic Photovoltaic(s)
O_2	Oxygen
$PC_{61}BM$	Phenyl-C_{61}-Butyric Acid Methyl Ester
$PC_{71}BM$	Phenyl-C_{71}-Butyric Acid Methyl Ester
PV	Photovoltaic(s)
Pu-239	Plutonium 239
MDMO-PPV	Poly[2-methoxy-5-(3′,7′-dimethyloctyloxy)-1,4-phenylenevinylene]
MEH-PPV	Poly[2-methoxy-5-(2′-ethyl-hexyloxy)-1,4-phenylene vinylene]
P3HT	Poly[3-hexylthiophene]

PDTP-DFBT	Poly[2,7-(5,5-bis-(3,7-dimethyloctyl)-5H-dithieno[3,2-b:2′,3′-d]pyran)-alt-4,7-(5,6-difluoro-2,1,3-benzothiadiazole)]
PEDOT:PSS	Poly[3,4-ethylenedioxythiophene] polystyrene sulfonate
PEN	Poly[ethylene 2,6-naphthalate]
PET	Polyethylene Terephthalate
PFN	Poly[(9,9-bis(3'-(N,N-dimethylamino)propyl)-2,7-fluorene)-alt-2,7-(9,9–dioctylfluorene)]
PTB7-Th	Poly[4,8-bis(5-(2-ethylhexyl)thiophen-2-yl)benzo[1,2-b:4,5-b′]dithiophene- co -3-fluorothieno[3,4-b] thiophene-2-carboxylate]
P	Power
P_{MPP}	Power at the Maximum Power Point
PCE	Power Conversion Efficiency
J_0	Reverse Saturation Current Density
RPM	Revolutions per Minute
s	Seconds
J_{SC}	Short-Circuit Current Density
Ag	Silver
D^*	Specific Detectivity
T	Temperature
TWh	Terawatt Hours
TiO_2	Titanium Oxide
UV	Ultraviolet
UPS	Ultraviolet Photoelectron Spectroscopy
V	Voltage or Volts
V	Volts

V_{MPP}	Voltage at the Maximum Power Point
λ	Wavelength
ZnO	Zinc Oxide

SUMMARY

Solid-state organic semiconductor-based photovoltaics (OPV) are an emerging technology being developed to generate clean and sustainable electricity in light weight, flexible and shatter-proof form factors. In this dissertation, firstly, a method to enhance the environmental stability of OPV is developed. Previous work has shown that the physical adsorption of the polymer polyethylenimine on the surface of conductors results in a significant reduction of the conductor work function. In this work, it is demonstrated that the reduction in work function of the conductors using polyethylenimine is independent of the order of deposition and can also be achieved by depositing the conductors on top of polyethylenimine. Consequently, novel OPV architectures are developed in which the commonly used but particularly air unstable calcium electrode is replaced by polyethylenimine in conjunction with various air stable metals as top electron-collecting electrodes. The performance of the novel calcium-free OPV is found to be comparable to reference OPV containing calcium electrodes.

Secondly, it is experimentally demonstrated that the energy of the charge-transfer complex formed by molecular interactions between the donor and acceptor components of the photoactive layer in OPV is the energy gap relevant for the thermal generation of carriers that leads to the reverse saturation current. Organic photodetectors that define the state-of-the-art in terms of dark current density (J_{Dark} on the order of 6 pA/cm^2) and specific detectivity ($D^* > 10^{14}$ Jones at visible wavelengths) are demonstrated by employing a donor-acceptor pair with a large charge-transfer complex energy, in conjunction with devices with large shunt resistance. The approach to reproducibly

fabricate high shunt resistance devices is detailed, which includes the optimization of the photoactive layer morphology, the photoactive layer thickness, and the work function of the charge collecting-electrodes. A proof of concept for scintillator-free organic semiconductor detectors of ionizing radiation enabled by this approach is also demonstrated.

CHAPTER 1

INTRODUCTION AND OBJECTIVES

In this chapter, the current state of electricity generation in the United States is discussed, including the pros and cons of power generation from various sources. Then, the role of photovoltaics (hereby referred to as PV) is examined, with particular attention paid to the motivation for the emerging class of PV, known as organic PV (OPV). Thereafter, the history and development of the field of OPV is discussed, up to the current state of the art. Finally, the objectives of the research conducted as part of this dissertation are outlined.

1.1 Electricity Generation in the United States

The means by which electricity is generated is of utmost importance in any society. Modern lifestyles and global population growth fuel an ever-increasing demand for energy at the lowest possible cost. However, the true cost of electricity generation is not always straightforward to identify. In addition to the direct cost of raw materials and their processing, the cost to the natural environment and public health are important externalities that must be considered but are difficult to quantify. Therefore, the energy policy of any country is one of the most important yet often divisive pieces of legislation.

The United States is the second largest producer of electricity in the world behind China. The contribution of different sources to electricity generation in the United States, along with the trends from recent years, is shown in Table 1 [1]:

Table 1.1 Electricity Generation by Source in the United States at Utility Scale Facilities

Source	Energy Generated in 2010 (TWh)	Energy Generated in 2014 (TWh)	Percentage of Energy Generation in 2014	Percentage Change (2010 to 2014)
Coal	1847	1582	38.6%	-14%
Gas	999	1139	27.8%	+14%
Nuclear	807	797	19.5%	-1.2%
Hydropower	260	259	6.3%	-0.3%
Wind	95	182	4.4%	+92%
Biopower	56	64	1.6%	+14%
Geothermal	15	16	0.4%	+4%
PV	0.4	15	0.4%	+3505%
TOTAL GENERATION	4125	4094	100%	-0.8%

By far, coal-based thermal power plants are the leading source of electricity generation in the United States. Coal is inexpensive, has a high energy density, and is easy to mine, store, and transport. However, the major disadvantage of generating electricity from coal is the generation of greenhouse gases and particulates that result from the combustion of the non-renewable fossil fuel. In the United States, the contribution toward power generation from coal has been decreasing as older plants are decommissioned.

Natural gas is another thermal-powered source of electricity generation. Although the combustion of natural gas results in less carbon dioxide emissions than coal, electricity generation from natural gas led to 440 million metric tons of carbon dioxide equivalent in 2014 [2]. The increase in electricity generated from natural gas in the United States has stemmed from developments in hydraulic fracturing technology to extract subsurface shale gas. The environmental impact of injecting high pressure fracturing fluid beneath the earth surface is actively under debate. Criticisms of hydraulic

fracturing including the risk of groundwater contamination by the fracturing fluid, the danger of chemical spills, and the large amount of water required for the process.

Nuclear power accounts for nearly one-fifth of electricity generation in the United States. Although generally considered cleaner than coal or gas-based technologies, some of the major disadvantages of nuclear power generation include the sourcing of uranium, disposal of radioactive waste, and high initial investment cost. Therefore, electricity generation from nuclear power plants in the United States has remained flat over the past few years.

Hydropower is the largest renewable source of electricity in the United States in terms of power generation. Hydroelectricity involves power generation by the use of falling water to drive turbines. The environmental impact caused by the damming of rivers is one of the major drawbacks of generation hydropower. In addition, there is low potential for growth since dams have already been erected at the most optimal river sites. As is the case with electricity generated from nuclear powered plants, there has not been growth in the generation of hydroelectric power between 2010 and 2014.

Industrial wind electricity generation harnesses the energy of wind to drive turbines. Wind is a clean and renewable source of energy but is intermittent in nature, therefore requiring backup sources of energy. In addition to aesthetic complaints, the low energy density of wind is a disadvantage that requires larger area coverage than competing technologies such as coal-powered plants. Nonetheless, the amount of energy generated from wind has doubled since 2010.

Biopower involves the energy provided by burning of agricultural by-products, such as sugarcane fiber. The disadvantage of biomass is the low energy density of the

agricultural inputs and that the methodology, as in fossil fuels, involves combustion of the input.

PV is different from any of the previously described sources of power generation in that they do not involve rotating turbines to generate power. PV involves the direct conversion of sunlight into electricity using semiconductor materials. Although the cumulative contribution of PV to electricity generation in the United States was miniscule at 0.4% in 2014, it has seen the strongest percentage growth over the last few years of any source of electricity by far. One of the major challenges of PV is the intermittent nature of sunlight, which necessitates reliance on storage technologies and backup sources. A second disadvantage is the relatively low power conversion efficiency from incident light to electrical power in the range of 15% - 20% in most deployed PV modules. Nonetheless, PV is actively being developed in industry as well as academia, and is considered to be one of the most promising renewable sources of energy. Unlike fossil fuels, sunlight is abundant, free, and available everywhere. More importantly, power generation from PV does not result in greenhouse gas emissions during operation. However, the amount of energy required for the manufacturing, installation, maintenance, and recovery of PV systems is an important factor that needs to be considered when comparing different PV technologies.

1.2 Current Status of Photovoltaic Technologies

It is important to distinguish between research level PV cells and commercially deployed PV modules. A single PV cell is the basic PV unit. PV modules are composed of multiple PV cells connected in series and parallel combinations so as to increase the

output current, voltage, and power. Multple PV modules are combined to form a PV panel. Multiple PV panels are then integrated into a PV system with other electronics, such as the inverter, battery, and cabling. In the context of this dissertation, the individual PV cell is relevant.

The state-of-the-art for various PV technologies at the research cell level is shown in Table 1.2 [3]. The relevant metric for PV is the power conversion efficiency (PCE) in converting incident optical power to output electrical power. As can be seen from the table, there is a broad spectrum of PV technologies, with the power conversion efficiency varying according to the choice of semiconductor material and PV cell structure. Work is ongoing in industry and at different research laboratories across the different PV platforms simultaneously.

Table 1.2. State-of-the Art in Various PV Technologies at the Research Cell Level

PV Technology	Power Conversion Efficiency	Company/Laboratory
Multi-Junction PV (2-terminal, monolithic)		
Four-junction or more (Concentrator)	46.0%	Fraunhofer ISE / Soitec / CEA Leti
Four-junction or more (Non-Concentrator)	38.8%	Boeing-Spectrolab (5-J)
Three-junction (Concentrator)	44.4%	Sharp (302x)
Three-junction (Non-Concentrator)	37.9%	Sharp
Two-junction (Concentrator)	34.1%	National Renewable Energy Laboratory (467x)
Two-junction (Non-Concentrator)	31.6%	Alta Devices
Single-Junction GaAs		
Single Crystal	27.5%	LG Electronics
Concentrator	29.1%	Franhofer ISE (117x)
Thin-Film Crystal	28.8%	Alta Devices
Crystalline Silicon PV		
Single Crystal (Concentrator)	27.6%	Amonix (92x)
Single Crystal (Non-Concentrator)	25.0%	SunPower (large-area)
Multicrystalline	21.3%	Trina Solar
Silicon hetero-structures (Heterojunction with Intrinsic Thin Layer)	25.6%	Panasonic
Thin-Film Crystal	21.2%	Solexel
Thin-Film Technologies (Inorganic)		
Copper Indium Gallium Selenide	22.3%	Solar Frontier
Cadmium Telluride	21.5%	First Solar
Hydrogenated Amorphous Silicon	13.6%	National Institute of Advanced Industrial Science and Technology
Emerging PV		
Dye-Sensitized PV	11.9%	Sharp
Perovskite PV	21.0%	École Polytechnique Fédérale de Lausanne
Organic PV	11.5%	Hong Kong University of Science and Technology

Brief descriptions of some of these important classes of PV are provided in the next sections.

1.2.1 Crystalline Silicon PV

The current commercial market for PV is dominated by crystalline silicon wafer-based modules. Crystalline silicon accounted for 92% of the total global PV production in 2014 [4]. Because of the sizable initial investment required to establish large-scale manufacturing, crystalline silicon has benefitted enormously from existing know-how from the microelectronics industry and is the most mature PV technology.

Crystalline silicon-based PV primarily falls under either the category of mono-crystalline or multi-crystalline PV cells. Mono-crystalline silicon PV are composed of wafers produced from the Czochralski process and are more efficient than multi-crystalline silicon PV because of the absence of grain boundaries which reduce the power conversion efficiency. However, multi-crystalline silicon PV modules are less expensive to produce, and as a result, have been deployed more widely (55% of global annual PV production in 2014) than mono-crystalline PV (36% of global annual PV production in 2014) [4].

1.2.2 Multi-Junction Compound Semiconductor PV

Inorganic multi-junction PV based on III-V compound semiconductors are the most efficient class of PV. This PV technology contains multiple photoactive junctions that absorb light from different parts of the solar spectrum. The PV architectures can be fairly complex and are consequently expensive. As a result, this PV technology is

suitable for space applications where the cost of the PV system is not the primary consideration, in addition to terrestrial concentrator systems. This class of PV is unlikely to be deployed for large-area power generation applications.

1.2.3 Inorganic Thin Film PV

This category comprises PV that are composed of inorganic films with thickness on the order of tens of micrometers deposited on various substrates. Inorganic thin film PV primarily refers to PV based on cadmium telluride (CdTe), copper indium gallium selenide (CIGS), and amorphous silicon (a-Si). This technology was envisioned to be competitive with crystalline silicon PV owing to reasonable power conversion efficiency and the need for less material. In fact, the market share for thin-film PV peaked at around 17% in 2009 coinciding with shortages in the supply of poly-crystalline silicon. Thin-film PV technologies accounted for 4.4 GW peak production in 2014 globally, which accounted for 9% of the global PV production [4].

1.2.4 Emerging PV Technologies

A number of emerging novel PV technologies are currently in the laboratory phase or on the cusp of commercialization. These technologies present a new low-cost fabrication paradigm and aim to disrupt the dominance of conventional silicon-based PV. It is to be seen how the emerging PV will overcome challenges including unproven operational lifetimes, difficulties in transitioning from the laboratory to commercial scale, and yield issues.

1.2.4.1 Dye-Sensitized PV

Dye-sensitized PV typically contain a ruthenium-based dye that sensitizes nanoparticles of porous TiO_2. The TiO_2 acts as a wide bandgap electron collector that contacts the transparent electron-collecting electrode. The dye is also in contact with a liquid electrolyte to which the holes flow. The circuit is completed through an iodide redox couple in contact with the counter electrode. The main criticism of dye-sensitized PV has been the presence of the liquid electrolyte that could be detrimental to lifetime.

1.2.4.2 Perovskite PV

Perovskite-based PV is a newly emerging technology that has gained much recent attention by virtue of reports of very high laboratory power conversion efficiency values (up to 21.0% at the research cell level [3]. Perovskite refers to the specific cubic unit cell crystal structure of the photoactive material, such as the prototypical methyl ammonium lead iodide, $CH_3NH_3PbI_3$. Since the perovskite PV class is still under active research, a number of areas need to be studied further, such as hysteresis effects. In addition, the presence of lead in the perovskite is an area of concern due to its toxicity.

1.2.4.3 Solid-State Organic Semiconductor PV

Finally, another emerging class of PV is that of solid-state organic semiconductor PV. These PV are composed of a blend of organic semiconductor materials that is sandwiched between electron and hole-collecting electrodes. Organic materials possess a number of unique characteristics which make them desirable to be used in solid-state PV.

Firstly, the optical and electrical properties of the materials making up the photoactive layer can be tuned through modifications of the chemical structure by the synthesis of new compounds.

Secondly, organic semiconductors possess high absorption coefficients. For example, the prototypical organic semiconductor poly(3-hexylthiophene) (P3HT) has an absorption coefficient of 10^5 cm^{-1} at the peak of the solar spectrum around 500 nm [5]. The large absorption coefficients allow OPV to be fabricated with photoactive layer film thicknesses on the order of hundreds of nm. The low film thicknesses allow films to be coated onto thin flexible substrates such as plastics. As a consequence, OPV can be produced in a light weight, flexible and shatter-proof form factor. The ability to easily tune the thickness of the photoactive layer in OPV also opens up niche applications such as semi-transparent OPV for use in building-integrated PV as energy-harvesting windows.

Thirdly, organic semiconductors can be processed at room temperature by deposition methodologies such as spin-coating or vacuum thermal evaporation. The deposition of organic materials via vacuum thermal evaporation has been successfully commercialized in volume manufacturing in the organic light-emitting diode industry. OPV are typically fabricated by all additive processing, and are envisioned to be mass-produced either in a roll-to-roll or plate-to-plate process analogous to a printing press, or by an assembly line of sequential coating processes such as dip-coating, thereby substantially reducing the investment required to establish manufacturing lines.

1.3 Development of the Field

1.3.1 The Photovoltaic Effect

In 1839, Becquerel [6] demonstrated the generation of current and voltage between metal plates coated with silver halides, which were submerged in various electrolytes, upon exposure to solar illumination. This discovery of the photovoltaic effect laid the foundation for a number of applications, including PV and photodetectors.

1.3.2 Electrical Semiconductivity in Organic Materials

Pioneering investigations of the semiconductivity in organic materials involved studying changes in electrical resistance with temperature. As the temperature of a semiconductor is raised, more electrons are excited across the bandgap, and are able to contribute to conduction.

Vartanyan, in 1946 [7], and Eley, in 1948, [8] studied the electrical conductivity of various phthalocyanines. In 1950, Akamatu and Inokuchi [9] measured electrical resistance in violanthrone, iso-violanthrone, and pyranthrone, as a function of temperature. Besides confirming exponential decreases in resistance as a function of temperature, authors concluded that the materials acted as intrinsic semiconductors since the temperature dependence of resistivity was observed even after repeated sublimation purifications, therefore meaning the role of impurities was insignificant.

1.3.3 The First Inorganic Semiconductor *p-n* Junction PV Cell

Soon afterwards, in 1954, Chapin, Fuller, and Pearson announced the first practical PV cell at Bell Laboratories [10], designating it the “Bell Solar Battery”. Based on silicon doped *p*-and *n*-type respectively by boron and arsenic, the authors claimed initial power conversion efficiency of around 6%.

1.3.4 Organic Semiconductor Single Material Schottky-Barrier Type PV

Much of the initial focus on OPV was on Schottky-barrier type PV. These cells display the photovoltaic behavior associated with the junction between an organic compound and a conductor, which produces a photogenerated current and voltage under illumination. Most frequently, Schottky-barrier junctions were formed between *p*-type organic semiconductors and low work function electrodes, while the other contact was chosen so as to form an Ohmic contact with the semiconductor.

In 1961, Inokuchi et al. [11] first described Schottky-barrier type OPV cells comprising the organic materials perylene, violanthrene, violanthrone, and coronene. For junctions between alkali metals and the organic semiconductors, the authors found maximum photogenerated power of 10^{-8} W. Many other researchers developed Schottky-barrier type OPV in the subsequent years [12-20]. Notably, in 1978, Morel et al. [21] demonstrated Schottky-barrier type OPV with power conversion efficiency of 0.7% under 78 mW/cm^2 illumination in the structure Al / Al_2O_3 / merocyanine dye / Ag.

1.3.5 Organic Semiconductor Bilayer Heterojunction PV Consisting of *n*-and *p*-Type Materials

One of the important breakthroughs in OPV research was the use of a heterojunction of different organic materials to split photogenerated excitons. Bilayer OPV based on an electron donor and acceptor material were the precursors to the modern bulk heterojunction type mixed donor:acceptor materials.

In 1958, Kearns and Calvin [22] created the first solid state organic semiconductor heterojunction using pressed powdered magnesium phthalocyanine (donor) and air-oxidized tetramethyl *p*-phenylenediamine (acceptor). The authors recorded a 2 pW power output and a maximum photovoltage of 200 mV under illumination by a projection lamp, but remarked that a high internal resistance was limiting PV performance.

After much intermediate work [23-26], Tang applied the donor-acceptor heterojunction concept and demonstrated some of the most efficient OPV cells of the time in 1986 [27]. He used copper phthalocyanine (CuPc) as the donor material and a perylene tetracarboxylic derivative (PTCD) as the acceptor. OPV with the structure glass / indium tin oxide (ITO) / CuPc (30 nm) / PTCD (50 nm) / Ag showed power conversion efficiency of 0.9% under 75 mW/cm^2 AM2 illumination. Tang is widely considered to be the father of the OPV field by virtue of his demonstration of a two material OPV cell with PCE around 1% under broadband illumination. Since Tang's publication, the vast majority of OPV that have been fabricated employed the heterojunction of a donor and acceptor type material.

1.3.6 Polymer-Based OPV

Sariciftci et al. [28] presented a major advance in 1993, by incorporating a solution-processed polymer, poly[2-methoxy-5-(2-ethylhexyloxy)-1,4-phenylenevinylene] (MEH-PPV) in OPV. The OPV structure was glass / ITO / MEH-PPV / C_{60} / Au. The solution-processed polymer MEH-PPV was spin-coated from xylene, while C_{60} was vacuum evaporated. The diodes showed a rectification ratio of around 10^4 and dark current less than 100 pA/cm^2 at an applied bias of 0 V. The authors reported a PCE of 0.04% under 1 mW/cm^2 monochromatic illumination at 514.5 nm.

1.3.7 Advances in Bulk Heterojunction OPV

The next notable advance came through the research of Alan Heeger's group in 1995, when Yu et al. [29] blended the semiconducting polymer MEH-PPV with the fullerene derivative [6,6]-phenyl C_{61} butyric acid methyl ester ($PC_{61}BM$) to form the photoactive layer. By this approach, the interfacial area between the donor and acceptor was enhanced, forming a heterojunction throughout the bulk of the film. The OPV structure that showed the highest PCE in their report was: glass / ITO / MEH-PPC:$PC_{61}BM$ (1:4 w/w) / Ca. The authors reported PCE of 2.9% under 20 mW/cm^2 monochromatic illumination of 430 nm.

In 2001, Shaheen et al. [30] demonstrated the importance of the choice of solvent and its effects on the film morphology of a bulk heterojunction of the donor poly[2-methoxy-5-(3′,7′-dimethyloctyloxy)-1,4-phenylenevinylene] (MDMO-PPV) with the acceptor $PC_{61}BM$, as they demonstrated 2.5% efficient cells under 80 mW/cm^2 AM1.5 illumination, using the bulk heterojunction concept. The OPV structure demonstrated was

glass / ITO / poly(3,4-ethylenedioxythiophene)-poly(styrenesulfonate) (PEDOT:PSS) / MDMO-PPV:$PC_{61}BM$ / lithium fluoride (LiF) / Al.

In 2003, the group of Sariciftci [31] introduced postproduction annealing treatment at a temperature above the glass transition temperature of the polymer in the donor:acceptor bulk heterojunction to yield 3.5% PCE cells with structure glass / ITO / PEDOT:PSS / poly(3-hexylthiophene) (P3HT):$PC_{61}BM$ / LiF / Al.

In 2005, Yang Yang et al. [32] optimized the active layer thickness and thermal annealing to yield 4% efficient OPV. Postproduction thermal annealing of OPV in the structure glass / ITO / PEDOT:PSS / P3HT:$PC_{61}BM$ / Ca / Al resulted in the highest efficiency at the time for that materials system.

Soon afterward, also in 2005, the Heeger group reported [33] PCE higher than 5% in the structure glass / ITO / PEDOT:PSS / P3HT:$PC_{61}BM$ / Al, illuminated under AM1.5 80 mW/cm^2 irradiance. The authors attributed the performance improvements to a number of effects stemming from the post-Al-metallization thermal annealing step, including morphology optimization, enhanced crystallization, and an improved electron-collecting contact.

In 2008, the group of Marks [34] also reported OPV with PCE higher than 5% in the P3HT:$PC_{61}BM$ materials system by replacing the prototypical PEDOT:PSS hole-collecting electrode by a 10 nm thick film of nickel oxide (NiO) deposited by pulsed laser deposition. The full structure of the OPV was glass / ITO / NiO / P3HT:$PC_{61}BM$ / Al.

Following numerous advances in P3HT-based OPV, in 2009, the Heeger group optimized the polymer PCDTBT [35], based on poly(2,7-carbazole), originally synthesized in the group of Mario Leclerc [36]. The authors reported internal quantum efficiency values approaching 100% in the visible spectrum and an NREL certified 5.96% efficient cell. In-house testing yielded PCE of 6.1% for OPV in the structure glass / ITO / PEDOT:PSS / PCDTBT:$PC_{71}BM$ / TiO_X / Al. Neither thermal annealing nor solvent additives were used during active layer processing.

Toward the end of 2009, a new family of high efficiency polymers was developed. These were low band gap polymers based on thieno[3,4-*b*]thiophene and benzodithiophene [37]. A collaborative effort between Solarmer Energy, UCLA, and the University of Chicago produced the polymers PBDTTT-E, PBDTTT-C, and PBDTTT-CF. The team reported an in-house champion OPV cell with PCE of 7.73% in the structure glass / ITO / PEDOT:PSS / PBDTTT-CF:$PC_{71}BM$ (with 1,8-diiodooctane additive) / Ca / Al. An OPV cell sent to NREL was certified at a PCE of 6.77%.

In 2010, another polymer, PTB7, from the thieno[3,4-*b*]thiophene - benzodithiophene family was synthesized by Luping Yu and Gang Li [38]. In the structure glass / ITO / PEDOT:PSS / PTB7:$PC_{71}BM$ / Ca / Al, the authors reported a PCE of 7.4% under AM1.5G 100 mW/cm^2 illumination.

In 2011, the group of Yong Cao utilized the polymer PTB7 to break the 8% mark [39], using it in conjunction with the polymer poly[(9,9-bis(3'-(N,N-dimethylamino)propyl)-2,7-fluorene)-alt-2,7-(9,9–dioctylfluorene)] (PFN) as a cathode interlayer. An OPV cell with structure glass / ITO / PEDOT:PSS / PTB7:$PC_{71}BM$ / PFN /

Ca / Al was certified at 8.37% PCE by the National Center of Supervision & Inspection on Solar Photovoltaic Products Quality, China (CPVT).

In 2012, the same group broke the 9% PCE mark in OPV by employing PTB7 and PFN in an inverted OPV architecture [40]: glass / ITO / PFN / PTB7:$PC_{71}BM$ (1:1.5 w/w) / MoO_3 / Ag. Under AM1.5G 100 mW/cm^2, the authors achieved a CPVT certified PCE of 9.214%.

In 2015, Harald Ade of NCSU and He Yan of HKUST broke the 10% PCE mark [41] in single-junction BHJ based OPV, reporting on versatile polymers that could be used with a variety of acceptors and retain their high efficiency, even in thick active layer films. The highest PCE polymer they used, poly[(5,6-difluoro-2,1,3-benzothiadiazol-4,7-diyl)-alt-(3,3’’’-di(2-octyldodecyl)-2,2’;5’,2’’;5’’,2’’’-quaterthiophen-5,5’’’-diyl)] (PffBT4T-2OD), contained 2-octyldodecyl (2OD) alkyl chains in conjunction with a quaterthiophene backbone. The champion cell with OPV structure glass / ITO / ZnO / PffBT4T-2OD : $TC_{71}BM$ / MoO_3 / Al was 10.8% efficient.

In February 2016, Heliatek reported a verified multi-junction OPV cell based on thermally evaporated small molecules, with PCE of 13.2%. The contents remain undisclosed for proprietary reasons [42].

In addition to the select milestones outlined in this section, numerous researchers across the world have made contributions toward the development of the field of OPV. Figure 1.1 (a) and (b) respectively show bar charts of the number of publications and citations within the field of OPV within the last 20 years.

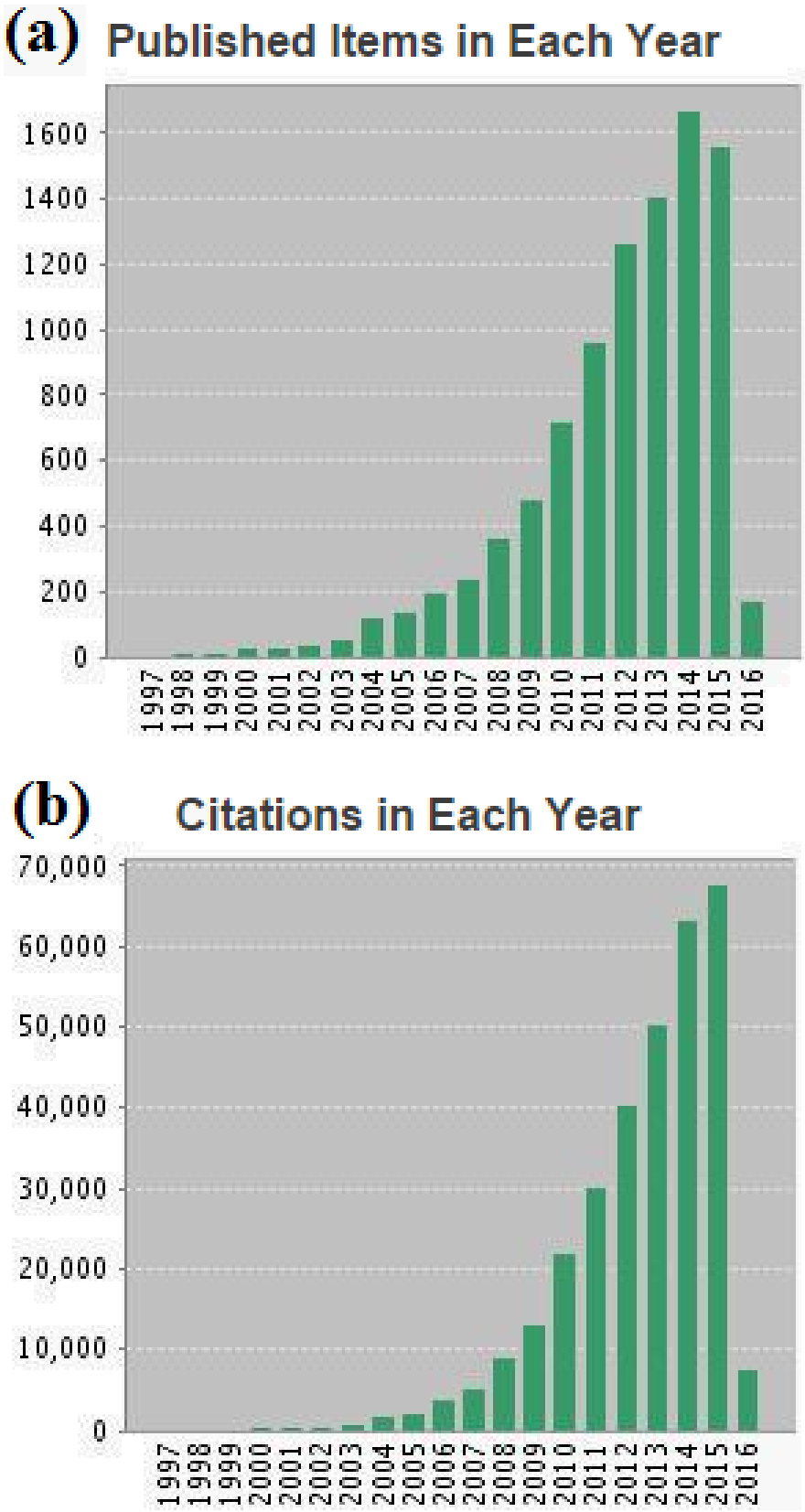

Figure 1.1. Number of (a) publications and (b) citations by year in the field of OPV.

1.4 Objectives of the Conducted Research

The first objective of the work presented in this dissertation is the enhancement of the environmental stability of OPV. Novel OPV cell architectures are investigated in which the commonly used but particularly unstable calcium electrode is replaced by a polymeric substituent that leads to the formation of an efficient electron-collecting electrode in conjunction with various air stable metals including silver and gold. The performance of the novel calcium-free OPV is found to be comparable to the reference cells that contain calcium electrodes.

The second objective of this work is the development of OPV-inspired design rules for organic photodetectors. The conventional approach in developing organic photodetectors focuses on the importance of so-called charge blocking layers at the electrodes that minimize recombination and reduce the dark leakage current that defines the sensitivity of the detector. This work highlights the significance of the interaction between the components of the photoactive layer in defining the limit of sensitivity of the photodetector, rather than the use of charge blocking layers. Thereafter, by optimizing the choice of semiconductor materials, the morphology and thickness of the photoactive layer, and the charge collecting-electrodes, organic semiconductor-based photodetectors that exhibited comparable performance to silicon photodetectors are demonstrated with high specific detectivity ($D^* > 10^{14}$ Jones) at visible and near infrared wavelengths. Novel applications enabled by the detectors are also explored, such as scintillator-free detectors for ionizing radiation.

1.5 Structure of the Dissertation

Chapter 2 discusses technical information relevant to OPV, including the origin of semiconductivity in certain organic materials, semiconductor device physics, the characterization of PV, the design of OPV, the operation of OPV, and the equivalent circuit model for PV.

Chapter 3 contains a detailed description of the experimental procedures that were employed in the fabrication and characterization of the OPV and photodetectors developed in the course of the research.

Chapter 4 describes one of the major sources of degradation in OPV, the use of calcium electrodes, and the methodology developed to enhance the operating lifetime of OPV.

Chapter 5 details the novel design rules developed for the fabrication of high detectivity organic photodetectors inspired by OPV.

Chapter 6 presents the conclusions arrived to in the course of the research and suggests possible avenues in which the scope of the research can be furthered.

CHAPTER 2

BACKGROUND

Pertinent technical details are furnished in this chapter of the dissertation, including the origin of semiconductivity in certain organic materials, relevant semiconductor device physics, the design and operation of OPV, and the equivalent circuit model for PV cells.

2.1 Semiconductivity in π-Conjugated Organic Materials

Organic semiconductors are carbon-based polymeric or molecular materials that possess electrical conductivity intermediate to metals and insulators. The conductivity of such materials varies as a function of conditions such as temperature or illumination. The origin of electrical semiconductivity in organic semiconductors lies in the nature of how carbon atoms bond with other atoms. Organic materials that show semiconductivity contain alternating single and double bonds between carbon atoms that give rise to a so-called π-conjugated system. The chemical structure of a common organic semiconductor, poly(3-hexylthiophene), is shown in Figure 2.1.

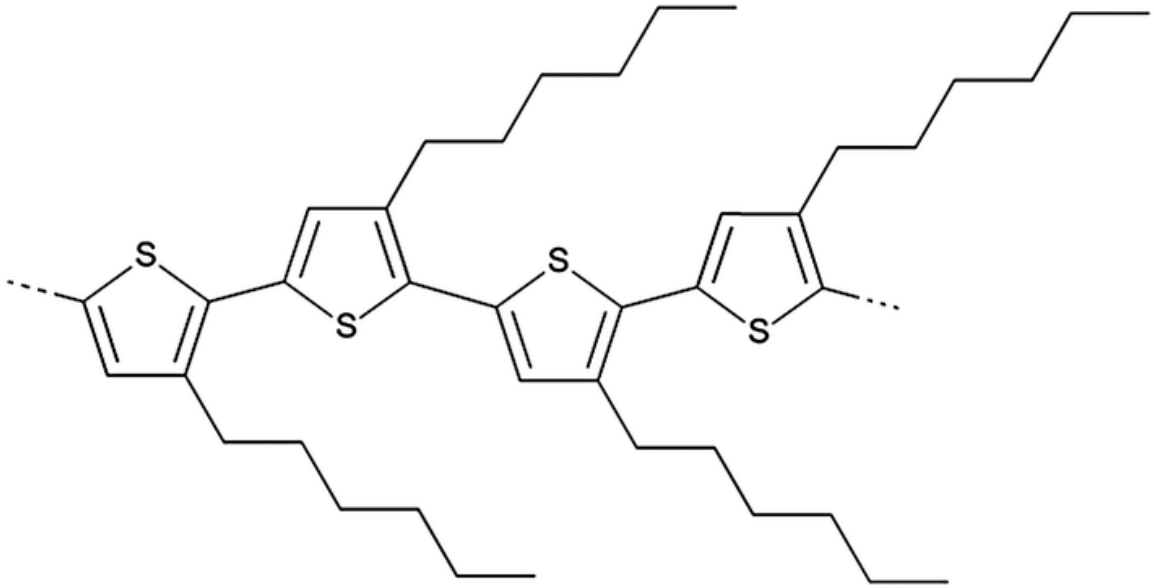

Figure 2.1 Chemical structure of poly(3-hexylthiophene), a common organic semiconductor.

2.1.1 Atomic Orbitals

According to the wave-like nature of electrons described by quantum mechanics, an electronic wave function, ψ, exists such that the square of the wave function, $\psi^2(x, y, z)$, expresses the probability of finding an electron at that position. Atomic orbitals are regions of space in which electrons have a high probability of being present. The atomic orbital shapes, such as the spherical *s* orbitals or the dumbbell-shaped *p* orbitals, are a graphical representation of $\psi^2(x, y, z)$, as shown in Figure 2.2. Each atomic orbital can accommodate either one or at most, two electrons of opposite spin. In the case of *p* orbitals, a maximum of 6 electrons can be accommodated in three distinct *p* orbitals, the p_x, p_y, and p_z orbitals, which are perpendicular to each other, and lie along the coordinate axis indicated in their respective subscripts. Being closer to the nucleus, the *s* orbitals are more stabilized in energy as compared to the *p* orbitals. A neutral atom of carbon has 6

electrons, with the ground state configuration $1s^2$, $2s^2$, $2p^2$. The $2p$ electrons do not occupy the same atomic orbital, so as to maximize their distance, in accordance with Hund's rule. In Figure 2.2, the arrows represent electrons, with the direction of the arrow indicating the electronic spin.

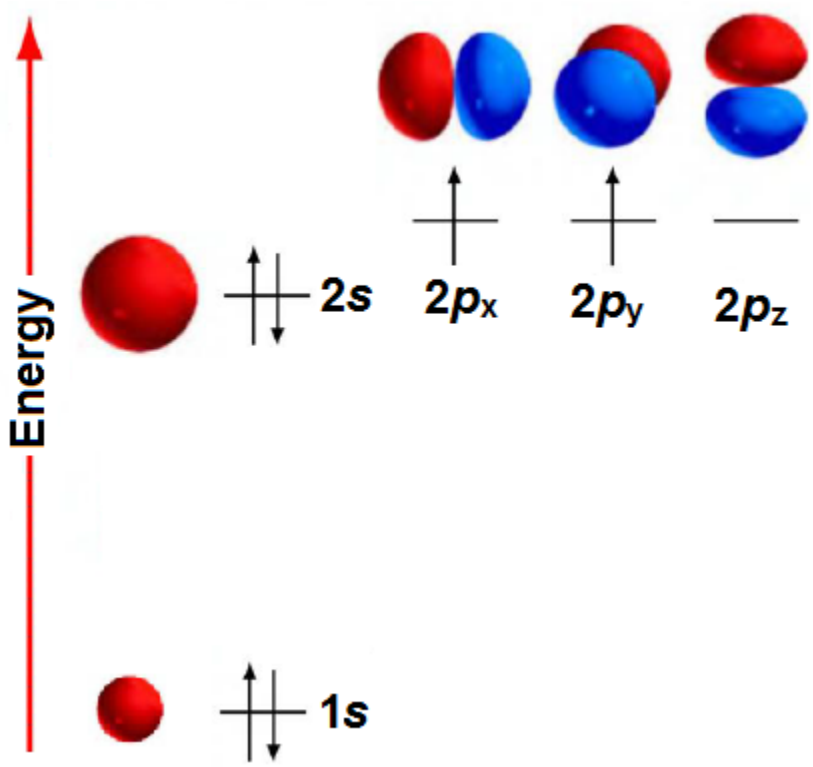

Figure 2.2. Atomic orbitals in a neutral atom of carbon in the ground state.

2.1.2 Hybrid Atomic Orbitals

The formation of chemical bonds between atoms results in the release of energy such that the total energy of the bonded system is lower than the total energy of the

system of separate atoms. Covalent bonding, as is relevant for carbon, involves the sharing of valence electrons between the bonding atoms. In carbon, these are the electrons in the 2*s* and 2*p* atomic orbitals. As shown in Figure 2.2, a neutral atom of carbon in the ground state has only two unpaired electrons. Carbon can form a larger number of bonds, and consequently yield a lower energy system by mixing the 2*s* and 2*p* atomic orbitals in a process known as atomic orbital hybridization.

2.1.2.1 sp^3 Hybridization

The 2*s* and $2p_x$, $2p_y$, and $2p_z$ orbitals, being close in energy, can combine to create four equivalent sp^3 hybrid atomic orbitals, in what is known as sp^3 hybridization. The four hybrid atomic orbitals allow a carbon atom to bond with four other atoms. A simple example of sp^3 hybridization is that found in the methane molecule with chemical structure CH_4.

2.1.2.2 sp^2 Hybridization

The 2*s* atomic orbital can combine with two of the 2*p* atomic orbitals to create three sp^2 hybrid atomic orbitals. The remaining 2*p* atomic orbital remains unhybridized and lies perpendicular to the plane containing the sp^2 hybrid atomic orbitals. The unhybridized *p* orbital is the source of semiconductivity in conjugated organic materials, as discussed ahead.

A simple example of sp^2 hybridization is exhibited in the ethene molecule with chemical structure C_2H_4. The sp^2 hybrid atomic orbitals associated with each carbon atom overlap to form a strong sigma (σ)-bond, where two electrons are shared. The

unhybridized *p* orbitals from each carbon atom overlap in a sideways fashion above and below the plane containing the σ-bond, to form a so-called pi (π)-bond. The π-electrons, being further away from the nuclei, are loosely held and more delocalized in space. Figure 2.3 (adapted from [43]) shows a schematic of the bonding molecular orbitals in ethene. The different colored lobes represent opposite phase signs in the molecular orbital.

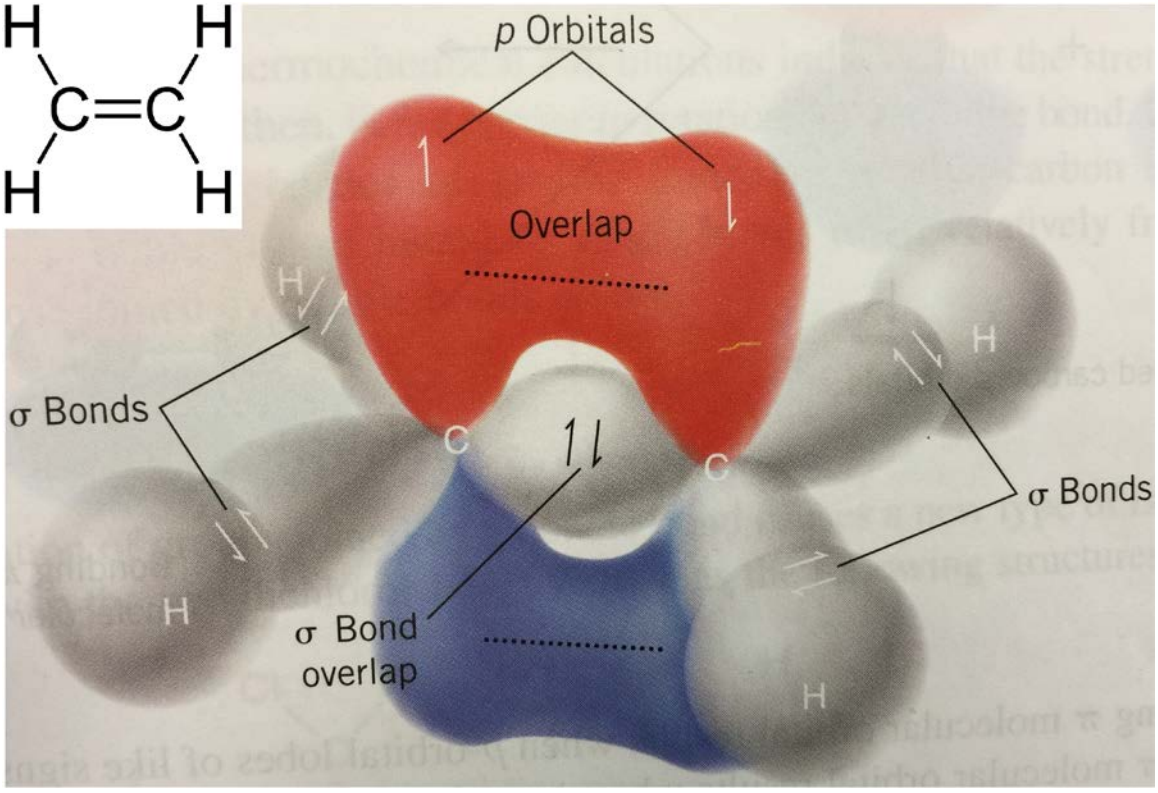

Figure 2.3. Bonding molecular orbitals in the ethene molecule, C_2H_4.

2.1.3 Molecular Orbitals

When multiple carbon atoms bond together, such as the two carbon atoms of ethene, as shown in Figure 2.3, their wave functions overlap, resulting in the creation of molecular orbitals that extend over multiple atoms. Molecular orbitals are regions of space where, as in atomic orbitals, either one or at most, two spin-paired electrons can be accommodated. Molecular orbitals are treated mathematically by the linear combination of atomic orbitals. Wave functions describing the molecular orbitals are obtained by adding or subtracting the wave functions of the atomic orbitals. The orbitals obtained by adding the atomic wave functions are known as bonding molecular orbitals and represent levels distributed in energy, known as π levels. The orbitals obtained by subtracting the atomic wave functions are known as anti-bonding molecular orbitals and represent levels distributed in energy, known as π^* levels. The bonding molecular orbitals are lower in energy than the anti-bonding molecular orbitals. At temperature $T = 0$ K, the ground state is defined by π levels that are full (containing electrons) and π^* levels that are empty. In the case of ethene, the bonding molecular orbital is referred to as the highest occupied molecular orbital (HOMO) and the anti-bonding molecular orbital is referred to as the lowest unoccupied molecular orbital (LUMO).

Figure 2.3 showed the bonding molecular orbital in ethene. Similarly, the anti-bonding molecular orbital can be calculated from the difference of the π-atomic orbitals as illustrated in Figure 2.4 [44]. The anti-bonding molecular orbital is higher in energy than the bonding molecular orbital and contains a node, at which the electronic wave function, and consequently the probability of finding an electron, is zero. The right hand side of the figure shows a representation of the unhybridized *p* orbitals that make up the

π-system in the molecule, with the shading representing the difference in phase in the orbitals.

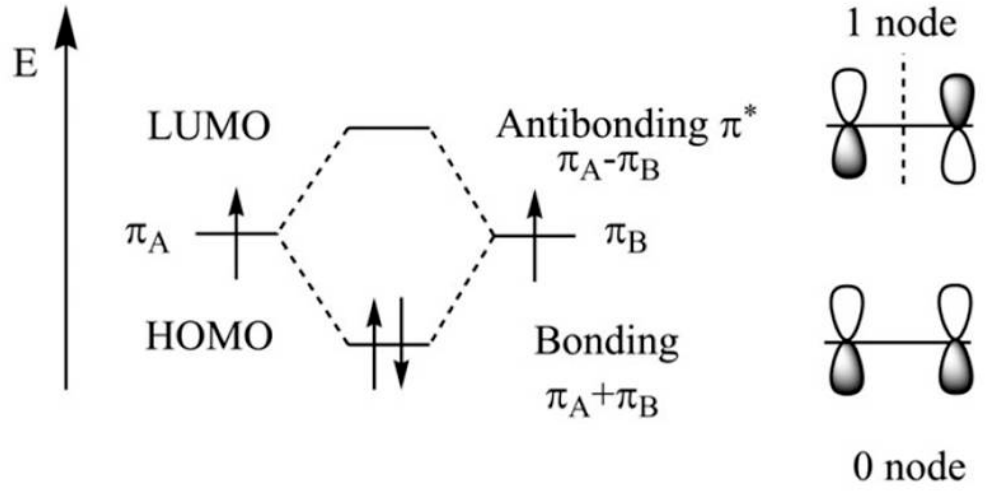

Figure 2.4. The linear combination of atomic orbitals πA and πB atomic orbitals in ethene yields the anti-bonding and bonding molecular orbitals πA - πB and πA + πB respectively.

2.1.4 Formation of Transport Bands

The π-system can be extended by increasing the number of carbon atoms in the conjugation chain. As the number of carbon atoms in the chain increases, more atomic orbitals overlap to form molecular orbitals, to the limit of the polymer polyethyne, where the difference in energy between successive discrete π (and π^*) levels becomes infinitesimally small, such that individual molecular orbitals approach bands distributed in energy, analogously to the well-known valence and conduction bands found in inorganic semiconductors, such as silicon. This situation is depicted in Figure 2.5.

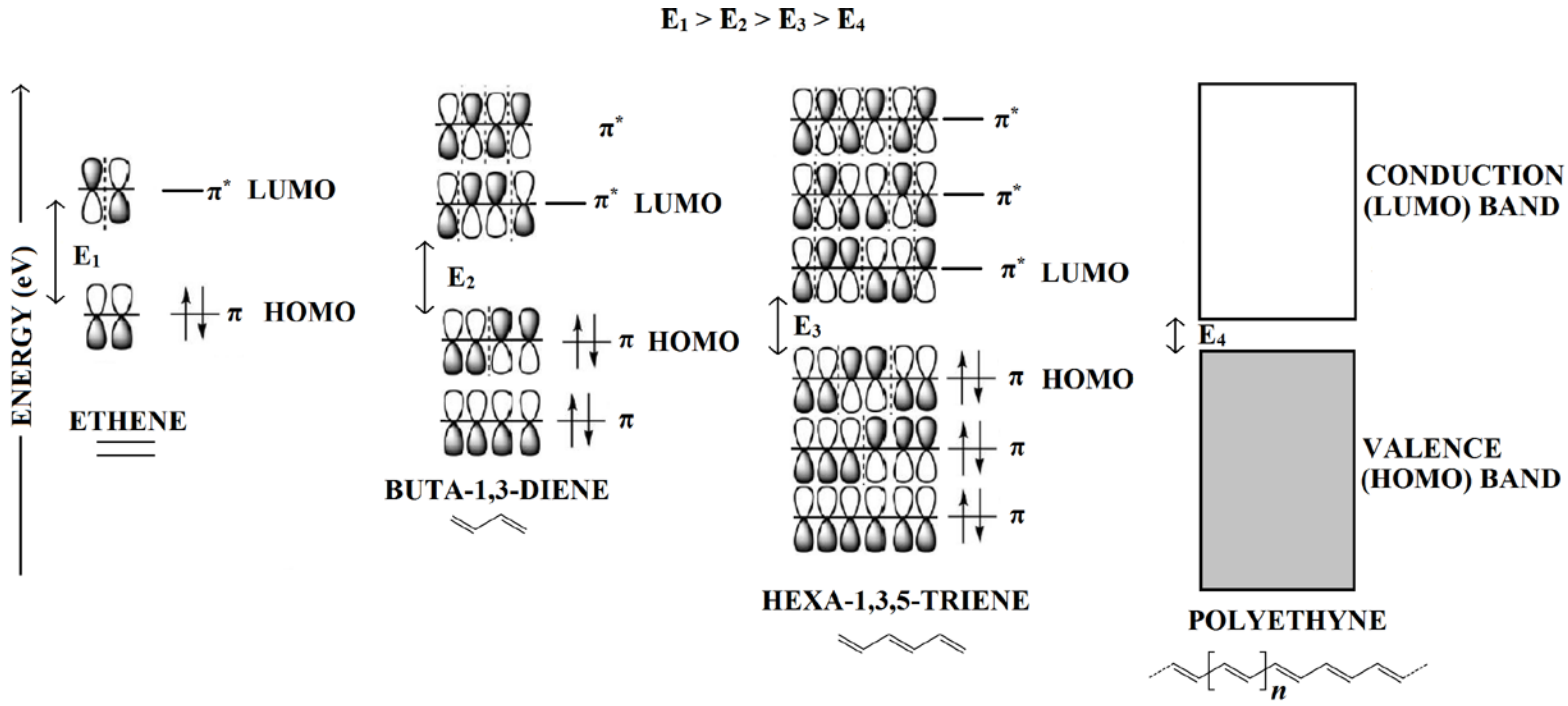

Figure 2.5. Formation of transport bands in an organic semiconductor.

The band formed by the π levels can be called the π band or valence band or HOMO band. The band formed by the π^* levels can be called the π^* band or conduction band or LUMO band.

2.1.5 Energetics and Optical Excitations in Organic Solids

The energy of molecular orbitals is usually calculated using computational chemistry approaches to solve the Schrödinger equation. For thin films of organic semiconductors, as relevant in OPV cells, a distinction arises in the energetics of the organic solid as opposed to the energetics at the molecular level due to intermolecular interactions.

For optoelectronics, such as PV cells or photodetectors, the optical gap is of particular significance. The optical gap is defined by the lowest optical transition from the ground state to the singly excited state, and is different than the transport gap, where the transport gap is the difference between the minimum energy required to remove an electron, the ionization energy (IE), and the energy gained by adding an electron, the electron affinity (EA). The difference lies in the electrostatic exciton binding energy found between an electron and hole after excitation. Coulomb's Law describes the electrostatic interaction between charged particles and can be used to describe the binding energy of an exciton:

$$E_{\text{Binding}} \propto \frac{q^4}{2\left(4\pi\varepsilon\varepsilon_0\right)^2 \hbar^2} \tag{2.1}$$

where q is the elementary charge, ε is the relative permittivity of the material (unitless), ε_0 is the vacuum permittivity, and $\hbar$ is the reduced Plank constant. Due to the low dielectric

constant (in the denominator of the exciton binding energy expression) in organic solids, which do not screen the charges effectively, and other effects associated with molecular geometry relaxation, the exciton binding energy is non-negligible in organic materials, and can be on the order of 400 meV [45]. As a result, when the electron is excited, it continues to feel the attraction to the hole that it left behind. In inorganic solids, the exciton binding energy is typically less than the thermal energy at room temperature.

In organic solids, unoccupied electronic levels can be experimentally probed in a thin film by means of techniques such as inverse photoelectron spectroscopy (IPES), which measures the electron affinity (EA) of a material, giving an estimate for the bottom of the LUMO band. In IPES, the material of interest is subjected to an electron beam. The unoccupied electronic levels can be determined by detecting the photons that are emitted due to the radiative relaxation of the electrons. Occupied states can also be probed experimentally, using a technique such as ultraviolet photoelectron spectroscopy (UPS), which measures the ionization energy (IE) of a material, providing an estimate for the top of the HOMO band. UPS is the complementary method to IPES wherein the energy of ejected electrons is detected after excitation from the ultraviolet photon source.

2.2 Semiconductor Device Physics

2.2.1 Fermi Level Energy

The Fermi level energy is the electrochemical potential, that is, the ability to do work, of a particle that is part of a system of a large number of particles at thermal equilibrium. Thermal equilibrium refers to conditions in which no energy is exchanged within different parts of a system or with the surroundings of the system. The Fermi

level energy can be calculated from a statistical distribution of electronic levels in energy, known as the Fermi-Dirac distribution function, $f(E)$:

$$f(E) = \frac{1}{1 + e^{\frac{E - E_F}{kT}}} \tag{2.2}$$

where E is the energy (typically in units of eV), E_F is the Fermi level energy (typically in units of eV), k is Boltzmann's constant (typically in units of eV/K), and T is the temperature (in units of K). From equation 2.2, the Fermi level energy, E_F, is the reference energy at which the probability of occupation by an electron is ½. The Fermi level energy does not necessarily correspond to an actual electronic level, and for semiconductors lies within the bandgap. Under equilibrium conditions in a semiconductor, where no external perturbations, such as applied voltage, magnetic field, or illumination act upon the system, the Fermi level energy for holes and electrons does not vary as a function of position across the semiconductor.

The Fermi level energy can be related to carrier concentrations through the following equations [46]:

$$E_F = E_C + kT \ln\left(\frac{n_0}{N_C}\right) \tag{2.3}$$

$$E_F = E_V - kT \ln\left(\frac{p_0}{N_V}\right) \tag{2.4}$$

where E_C (E_V) is the energy at the conduction (valence) band edge (typically in units of eV), N_C (N_V) is the effective density of states per unit volume in the conduction (valence)

band (in units of cm^{-3}), and n_0 (p_0) is the equilibrium density of electrons (holes) (in units of cm^{-3}).

2.2.2 Quasi-Fermi Levels under Non-Equilibrium Conditions

Under non-equilibrium conditions in a semiconductor, for example, under illumination, extra holes and electrons are generated such that the non-equilibrium carrier concentrations of electrons and holes can be expressed as the sum of the carrier density at equilibrium and the extra carriers generated because of the perturbation:

$$n = n_0 + \Delta n \tag{2.5}$$

$$p = p_0 + \Delta p \tag{2.6}$$

where n (p) is the total carrier concentration of electrons (holes) (in units of cm^{-3}) and Δn (Δp) is the additional concentration of electrons (holes) generated by the perturbation.

The generated carriers also have an equal rate of relaxation, leading to a so-called quasi-equilibrium situation where Fermi-Dirac statistics are applicable. The non-equilibrium carrier concentrations can be linked to so-called quasi-Fermi energy levels. A semiconductor under illumination displays distinct quasi-Fermi levels for electrons in the conduction band and holes in the valence band, such that:

$$n = n_0 + \Delta n = n_i e^{\frac{F_N - E_i}{kT}} \tag{2.7}$$

$$F_N = E_i + kT \ln\left(\frac{n_0 + \Delta n}{n_i}\right) \tag{2.8}$$

$$p = p_0 + \Delta p = p_i e^{\frac{E_i - F_P}{kT}} \tag{2.9}$$

$$F_P = E_i - kT \ln\left(\frac{p_0 + \Delta p}{p_i}\right) \tag{2.10}$$

where n_i (p_i) is the intrinsic carrier concentration of electrons (holes), F_N (F_P) is the quasi-Fermi level energy for electrons (holes), and E_i is the intrinsic Fermi energy level (in eV).

Of specific relevance to PV cells is that the Gibbs free energy delivered to a load by dN electrons and holes in a semiconductor under illumination is (F_N- F_P) dN [47].

2.2.3 Carrier Transport

The transport of carriers through the photoactive layer to the respective electrodes is a critical process in PV operation, and impacts the photogenerated current. Carrier transport can occur by two processes. The first is drift under the influence of an electric field, such as that created by the difference in work function of electrodes in an OPV cell. The second is diffusion by virtue of a gradient in carrier concentration.

2.2.3.1 Drift

Free electrons drift in the direction opposite of an applied electric field. Drift is categorized by an important film property known as the field-effect mobility, μ, measured in units of cm^2 / (V s). The field effect mobility in an organic film is dependent upon how the film is processed. Therefore, the processing solvent, film drying method, thermal annealing time, and presence of solvent additives, can all impact the mobility.

The one dimensional drift current density (in units of mA/cm^2) can be expressed as [46]:

$$J_{\text{drift, n}} = qn\mu_{\text{n}}E \tag{2.11}$$

where q is the elementary charge, n is the charge carrier concentration of electrons, μ_{n} is the field-effect mobility for electrons, and E is the electric field. Analogously for holes, the drift current is:

$$J_{\text{drift, p}} = qp\mu_{p}E \tag{2.12}$$

2.2.3.2 Diffusion

Charge carriers in semiconductors diffuse from regions of high concentration to regions of low concentration. Their movement gives rise to a consequent diffusion current. For electrons, this current can be expressed as [46]:

$$J_{\text{diffusion, n}} = qD_{\text{n}}\frac{dn}{dx} \tag{2.13}$$

where D_{n} is the diffusion constant for electrons (in units of $\text{cm}^2\ \text{s}^{-1}$) and x represents the one-dimensional position. Analogously for holes, the diffusion current is:

$$J_{\text{diffusion, p}} = -qD_{\text{p}}\frac{dp}{dx} \tag{2.14}$$

where D_{p} is the diffusion constant for holes.

A relationship can be established between drift and diffusion processes by virtue of the Einstein relationships for electrons and holes:

$$D_{\text{n}} = \frac{kT}{q}\mu_{\text{n}} \tag{2.15}$$

$$D_{\text{p}} = \frac{kT}{q}\mu_{\text{p}} \tag{2.16}$$

2.2.3.3 Total Current

The total current can be obtained by summing the contributions from drift and diffusion, such that, in one direction:

$$J_{\text{Total, n}} = qn\mu_{\text{n}}E + qD_{\text{n}}\frac{dn}{dx} \tag{2.17}$$

$$J_{\text{Total, p}} = qp\mu_{\text{p}}E - qD_{\text{p}}\frac{dp}{dx} \tag{2.18}$$

The drift and diffusion expressions can be unified using the quasi-Fermi level expressions for electrons and holes to yield:

$$J_{\text{Total, n}} = n\mu_{\text{n}}\frac{dF_{\text{N}}}{dx} \tag{2.19}$$

$$J_{\text{Total, p}} = p\mu_{\text{p}}\frac{dF_{\text{P}}}{dx} \tag{2.20}$$

The unified expression for the total current will have implications when the photogenerated current in an OPV cell is discussed ahead.

2.2.4 Carrier Recombination / Thermal Generation

Carrier recombination and generation are important processes that occur in semiconductors and have an impact on OPV performance. Recombination refers to the relaxation of carriers back toward an equilibrium state after the removal of a perturbation, such as incident light. Generation is the reverse process of recombination and is usually considered in the context of thermal generation of carriers.

2.2.4.1 Radiative Recombination

Radiative recombination is the process by which an excited carrier relaxes from its excited state to a lower energy state, along with the emission of a photon with energy corresponding to the difference in the energy between the states. Since radiative recombination is related to the relaxation of excited carriers, it is intuitive that the radiative recombination rate depends on the concentration of electrons in the excited state or conduction band, *n*, and holes in the unexcited state, or valence band, *p*. Radiative recombination is described by a radiative recombination rate given by [48]:

$$R_{\text{Radiative}} = Bnp \tag{2.21}$$

where *B* is a material dependent recombination coefficient.

2.2.4.2 Auger Recombination

Auger recombination is a non-radiative recombination process, in which a recombining electron transfers its energy to a secondary electron rather than emitting a photon of light (as in radiative recombination). The secondary excited electron then relaxes with the emission of phonons that are exchanged with the system as thermal energy.

2.2.4.3 Shockley-Read-Hall (Trap-Assisted) Recombination

Shockley-Read-Hall refers to a two-step recombination process that occurs through trap centers located within the bandgap of a material. An excited electron can relax down to a trap, where it is annihilated by a hole from the valence band.

According to the principle of detailed balance, every recombination process has a corresponding generation process under equilibrium. Under equilibrium conditions, the thermal generation rate equals the recombination rate. In relation to PV cells, the thermal generation of carriers manifests itself in the reverse saturation current density.

2.3 Characterization, Design, and Operation of OPV

2.3.1 Electrical Characterization

PV cells are two terminal devices that produce a photo-generated voltage and current under illumination, the product of which, is power ($P = I \times V$). The key metric of interest in PV cells is the power conversion efficiency (PCE) of converting incident optical power into output electrical power. The PCE of a PV cell can be determined by plotting the current generated by the PV cell under illumination against the applied bias. An illumination irradiance of 1 sun or 100 mW/cm^2 is typically used as the optical input in order to make meaningful comparisons across PV cells. The standard AM1.5G spectrum is shown in Figure 2.6 [49]:

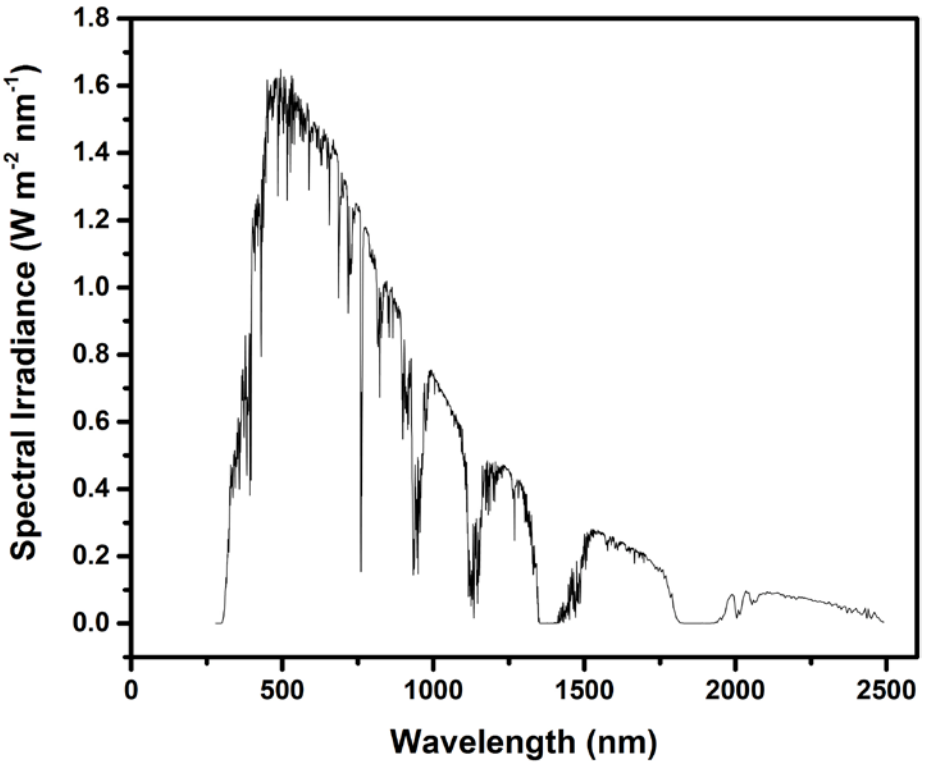

Figure 2.6. AM1.5G spectrum.

From Figure 2.6, it can be seen that PV cells need to have large absorption in the visible and near infrared portion of the electromagnetic spectrum.

When plotting the electrical characterization of a solar cell, the current is frequently normalized by the cell area and presented as a current density. Representative current density-voltage and power-voltage curves at an arbitrary level of illumination are shown in Figure 2.7. The fourth quadrant is of interest since the product of the current density (negative) and voltage (positive) results in a negative or generated power.

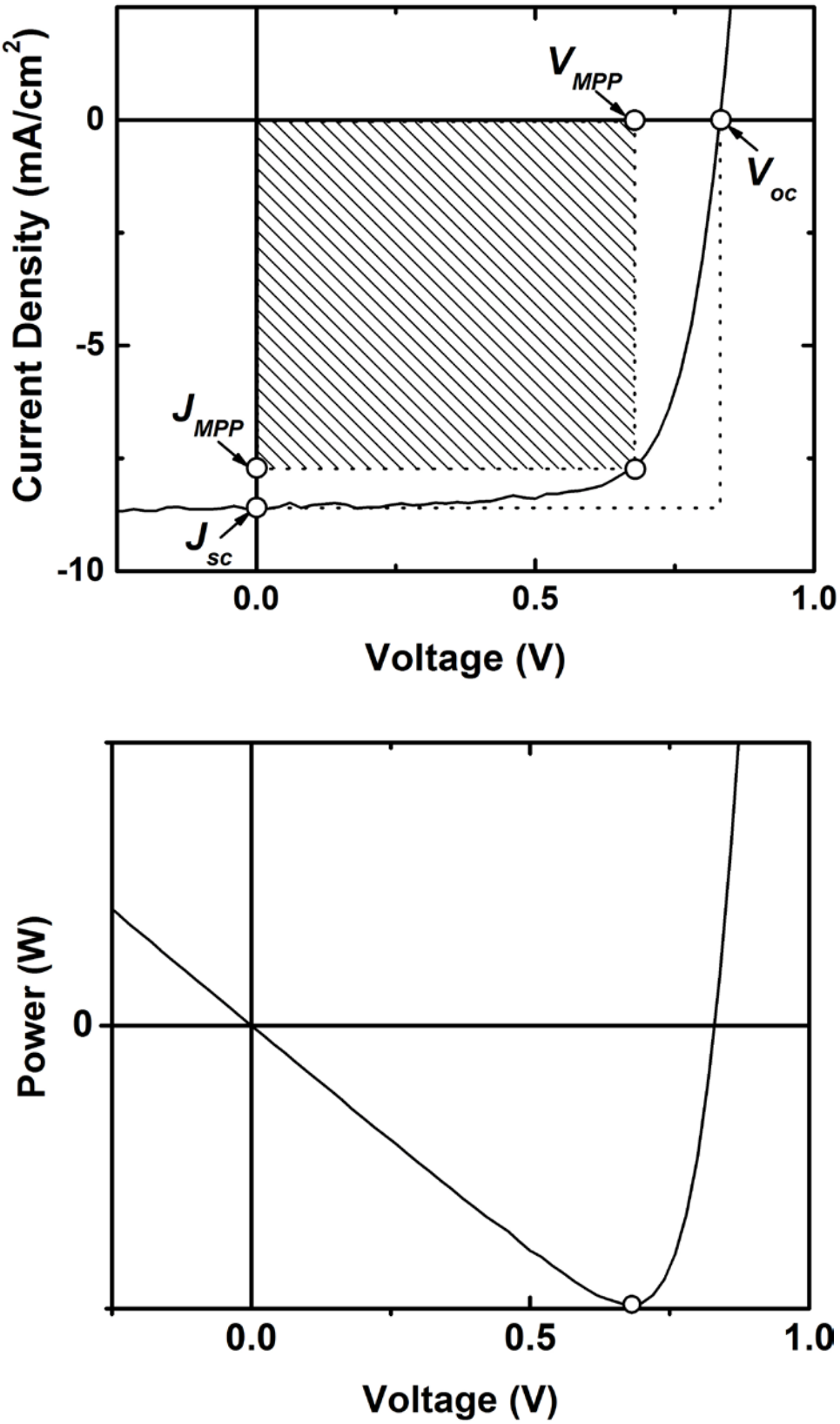

Figure 2.7. Power and current density as a function of voltage for a PV cell under an arbitrary level of illumination.

In the *J-V* curve shown under illumination (top panel in Figure 2.7), J_{SC} represents the short-circuit current density. J_{SC} is the maximum current density that the cell generates at that particular irradiance, and occurs when the voltage is zero, i.e. the two terminals are shorted.

V_{OC} represents the open-circuit voltage. V_{OC} is the maximum EMF the cell generates at that particular irradiance, and occurs when the current in the cell is zero, i.e. the two terminals are at open circuit.

Since power is the product of current and voltage, there is no power generated at either J_{SC} or V_{OC}. Instead, the PV cell is operated at the maximum power point, at which the $J \times V$ product is maximized, and is represented by (V_{MPP}, J_{MPP}) in Figure 2.7. The deviation of the maximum power point from the (V_{OC}, J_{SC}) point is reflected in the fill factor (FF), defined as:

$$\mathrm{FF} = \frac{V_{\mathrm{MPP}} \times J_{\mathrm{MPP}}}{V_{\mathrm{OC}} \times J_{\mathrm{SC}}} \tag{2.22}$$

Graphically, the FF can be visualized as the ratio of the area of the rectangle defined by the shaded region to the area of the rectangle defined by the dotted boundary and coordinate axes in the top panel of Figure 2.7.

From the curve under illumination, the PCE can then be calculated from:

$$\mathrm{PCE} = \frac{V_{\mathrm{OC}} \times J_{\mathrm{SC}} \times \mathrm{FF}}{P_{\mathrm{in}}} \times 100\% \tag{2.23}$$

2.3.2 Design of OPV

Most OPV have the following general structure:

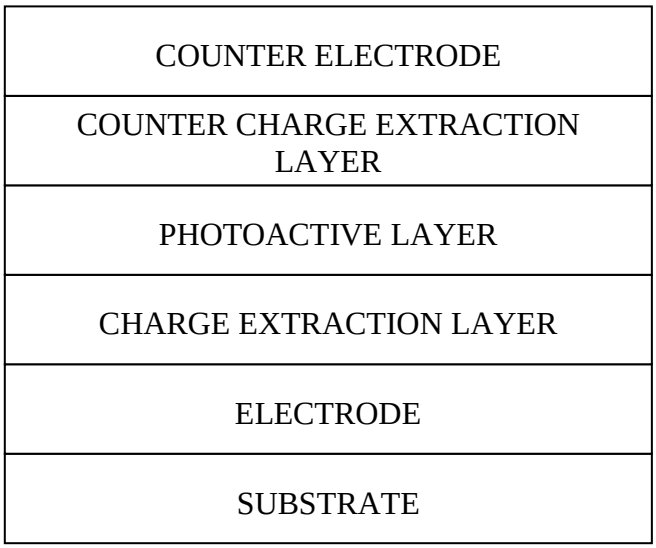

Figure 2.8. General structure of an OPV cell.

2.3.2.1 Substrate

The substrate is the carrier, upon which, the rest of the functional layers are deposited to build up the OPV cell. Glass is most frequently used as the substrate in OPV. Reports that communicate high power conversion efficiency OPV results with novel photoactive layer polymers almost invariably contain glass as the substrate. However, since glass is not compatible with flexible OPV, researchers often fabricate samples on various plastics such as polyethylene terephthalate (PET) or polyethylene naphthalate (PEN). Since light passes through the substrate to reach the photoactive layer, the optical transparency of the substrate needs to be maximized. The optical transparency of glass is above 90% for visible and higher wavelengths. In addition, since other functional layers are coated on the substrate, the surface roughness is important. If the surface roughness is on the order of the film thickness, the yield will suffer.

2.3.2.2 Electrode

The bottom electrode makes up one of the two terminals of the OPV cell. Just as the substrate, the bottom electrode needs to have a high optical transmittance to allow the maximum number of photons to reach the photoactive layer. However, in addition, the transparent electrode also needs to have a high electrical conductivity to effectively collect charge carriers. Electrical conductivity and optical transmittance are usually competing quantities since electrical conductivity is enhanced by doping the electrode material, typically an oxide, with charge carriers, which can absorb light. By far, tin-doped indium oxide (ITO) is the most commonly used transparent conductor with an optical transparency above 85% in the visible spectrum, coupled with sheet resistance of 5 - 15 Ω/□.

2.3.2.3 Charge Extraction Layer

The transparent electrode, such as ITO, is usually coated with a charge extraction layer. The charge extraction layer forms the contact with the photoactive layer, so its work function can be tailored so as not to form a barrier to the collection of the appropriate charge carrier. A charge extraction layer with an appropriate work function is selected based on the geometry of the cell, i.e., whether the bottom electrode collects holes (as in the so-called conventional geometry) or collects electrons (as in the so-called inverted geometry).

The hole extraction layer is chosen such that is has a work function that is larger than the Fermi level energy of the donor component of the photoactive layer (described in the next sub-section). The difference in work function of the electrodes acts as an upper limit to the maximum V_{OC} extracted from the cell, so a high work function electrode is

used for hole collection. Typical hole extraction layers, such as PEDOT:PSS or MoO_3, have a work function higher than 5 eV and are more stable than ITO, the work function of which, decreases upon exposure to UV irradiation [50].

For the charge extraction layer in the OPV geometry where the bottom electrode collects electrons, ZnO is the typical material of choice because of its low work function of around 4.3 eV [51].

2.3.2.4 Photoactive Layer

The photoactive layer is the organic semiconductor film that absorbs light and leads to the generation of holes and electrons.

2.3.2.4.1 Use of Donor and Acceptor Materials

As a result of the photo-generation of excitons in organic materials, the photoactive layer in OPV and photodetectors is typically made up of a so-called donor material in conjunction with a so-called acceptor material. The donor material is typically a conjugated polymer (large molecules containing a distribution of repeat units) or a small molecule (compounds with a well-defined molecular weight). The acceptor material is most commonly (but not necessarily) a fullerene-derivative.

The photogenerated exciton can gain sufficient energy at the interface between the donor and acceptor material to split into free charges that can be transported to the respective electrodes for collection. For the donor-acceptor pair, the component with the higher electron affinity is known as the electron acceptor, while the material with the lower ionization energy is known as the electron donor. The donor material will usually

have a high mobility for holes, and the acceptor for electrons. The combination of a donor and acceptor material is needed since the bound excitons can only acquire enough energy to be split into free carriers at the donor-acceptor interface. Early OPV designs relied upon bilayers of donor and acceptor materials.

2.3.2.4.2 Bulk Heterojunction

The early donor-acceptor bilayer OPV architectures had a limitation because of the exciton diffusion length in organic semiconductors. The exciton diffusion length is the average length after which the exciton recombines and can be on the order of tens of nm [52]. The photogenerated excitons not generated near the donor acceptor interface in a donor-acceptor bilayer photoactive layer recombined, resulting in a wasted photon, and low PCE. Simply reducing the thickness of the donor and acceptor bilayers would lead to incomplete absorption of photons leading to a diminished J_{SC}. The solution to this problem was the development of the bulk heterojunction.

Mixing the donor and acceptor components led to the distribution of a heterojunction throughout the volume of the film, called a bulk heterojunction (BHJ). The BHJ allows photogenerated excitons to reach a donor: acceptor heterojunction and be split close to the location in which they are generated before recombining.

Morphology studies [53] have shown that the bulk heterojunction consists of three phases, where one is rich in the donor type material, one is rich in the acceptor type material, and a third mixed phase. After the photo-generation and splitting of excitons in the mixed phase, the electrons and holes respectively accumulate in the acceptor and

donor rich phases, and are transported to the electron- and hole-collecting electrodes, respectively.

2.3.2.5 Counter Charge Extraction Layer

The counter charge extraction layer above the photoactive layer serves the same function as the charge extraction layer except for the opposite sign charge carrier. For OPV in which electrons are collected at the top electrode, a low work function material, such as Ca is typically used as the extraction layer, while for inverted geometry OPV in which holes are collected at the top electrode, PEDOT:PSS or MoO_3 are the materials of choice.

2.3.2.6 Counter Electrode

The counter electrode makes contact with the counter charge extraction layer. After the charge extraction layer delivers the charge carriers generated in the transverse direction through the photoactive layer, the counter electrode then transports the collected charges across the plane of the top surface of the PV cell to external leads. Frequently, the counter electrode in OPV will be a reflective metal, the nature of which, allows a second pass through the photoactive layer for photons not absorbed during the first pass. However, OPV cells can also be designed to contain semi-transparent rather than reflective counter electrodes for applications such as energy-harvesting smart windows.

2.3.3 Operation of OPV

2.3.3.1 Photovoltage

Photovoltage refers to the electromotive force produced upon exposure of the PV cell to light. The carrier concentration of holes and electrons under illumination can be related to the respective quasi-Fermi level energies for the carriers. The splitting of the quasi-Fermi levels for holes and electrons at their respective collection electrodes defines the photovoltage generated by the cell:

$$qV_{\mathrm{ph}} = F_{\mathrm{N}}\left(\text{at the Electron Collecting Electrode}\right) - F_{\mathrm{P}}\left(\text{at the Hole Collecting Electrode}\right) \tag{2.24}$$

Recall from equations 2.8 and 2.10 that the quasi-Fermi level energy is a logarithmic function of the illumination charge carrier density. Consequently, the photovoltage is also a logarithmic function of carrier density. The difference in work function of the electron and hole collecting-electrodes, defines the co-called built in potential V_{BI}. The photovoltage cannot exceed V_{BI}.

2.3.3.2 Photocurrent

The photocurrent is the current that is produced by the OPV cell under illumination.

Previously, the unified expressions for the total electron and hole current were stated:

$$J_{Total,\,n} = n\mu_e \frac{dF_{\mathrm{N}}}{dx} \tag{2.25}$$

$$J_{Total,\,p} = p\mu_p \frac{dF_{\mathrm{P}}}{dx} \tag{2.26}$$

The photocurrent is linearly dependent on carrier concentration, and is proportional to the slope of the quasi-Fermi levels versus position. The quasi-Fermi level varies as a function of position when an electric field is acting on the semiconductor, as is the case with the built in potential due to electrodes of different work function.

2.3.3.3 Operation in the Dark

The energy band diagram of an OPV cell in the dark under thermal equilibrium conditions is shown in Figure 2.9.

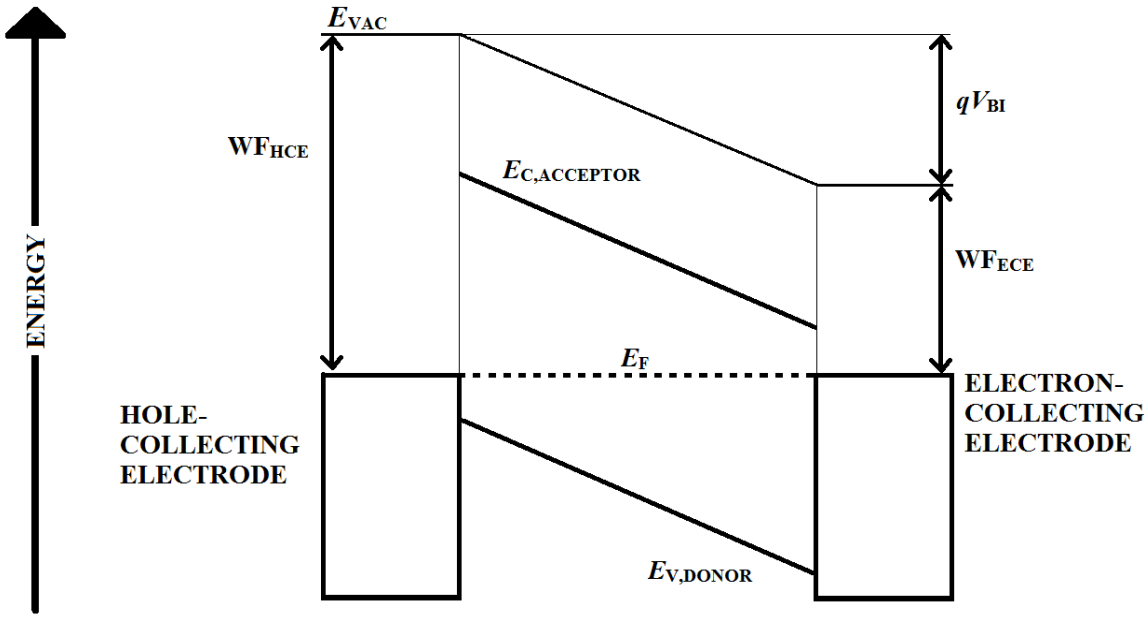

Figure 2.9. Energy band diagram of an OPV cell under equilibrium conditions in the dark.

Under equilibrium conditions in the dark, the Fermi level energy, E_F, is independent of position throughout the PV cell, and aligned across the hole-collecting electrode, the photoactive layer, and the electron-collecting electrode. Also, the difference in the work function of the electron-collecting electrode, WF_{ECE}, and the work

function of the hole-collecting electrode, WF_{HCE}, leads to the built in potential, qV_{BI}, and is reflected in the tilted donor valence band, $E_{V,\,DONOR}$, and acceptor conduction band, $E_{C,\,ACCEPTOR}$.

Since the quasi-Fermi level energy for holes and electrons is identical throughout the PV cell, ($E_F = F_N = F_P$) there is no photovoltage generated in the dark. Also, since there is no gradient in the quasi-Fermi level (flat Fermi level energy) there is no photocurrent generated in the dark.

2.3.3.4 Operation under Illumination

Under illumination, equilibrium conditions no longer hold. However, when the rate of carrier generation equals the rate of carrier recombination, the system reaches a so-called quasi-equilibrium, where the energy band diagram shown in Figure 2.10 can describe the system.

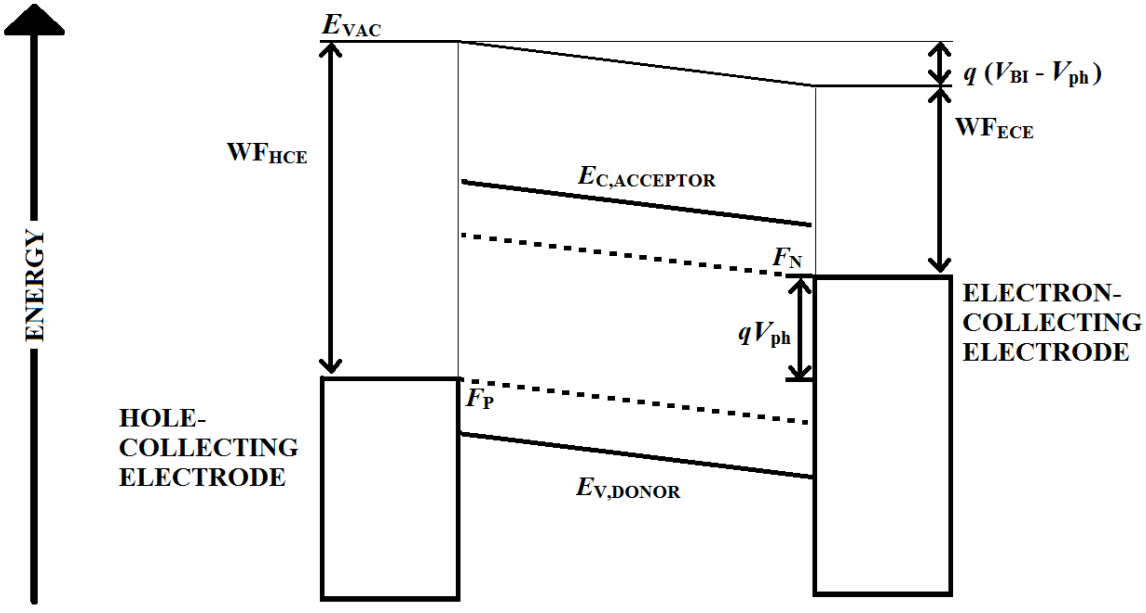

Figure 2.10. Energy band diagram of an OPV cell under quasi-equilibrium conditions under illumination.

Unlike the situation in the dark, the Fermi level energy in the photoactive layer is distinct for electrons and holes under illumination. The difference in the quasi-Fermi level energy of holes at the hole-collecting electrode and the quasi-Fermi level energy of electrons at the electron-collecting electrode defines the photovoltage generated at that particular level of illumination. In addition, the gradient in the quasi-Fermi level defines the photocurrent under that level of illumination

Under illumination, at short circuit, the energy band diagram looks as shown in Figure 2.11.

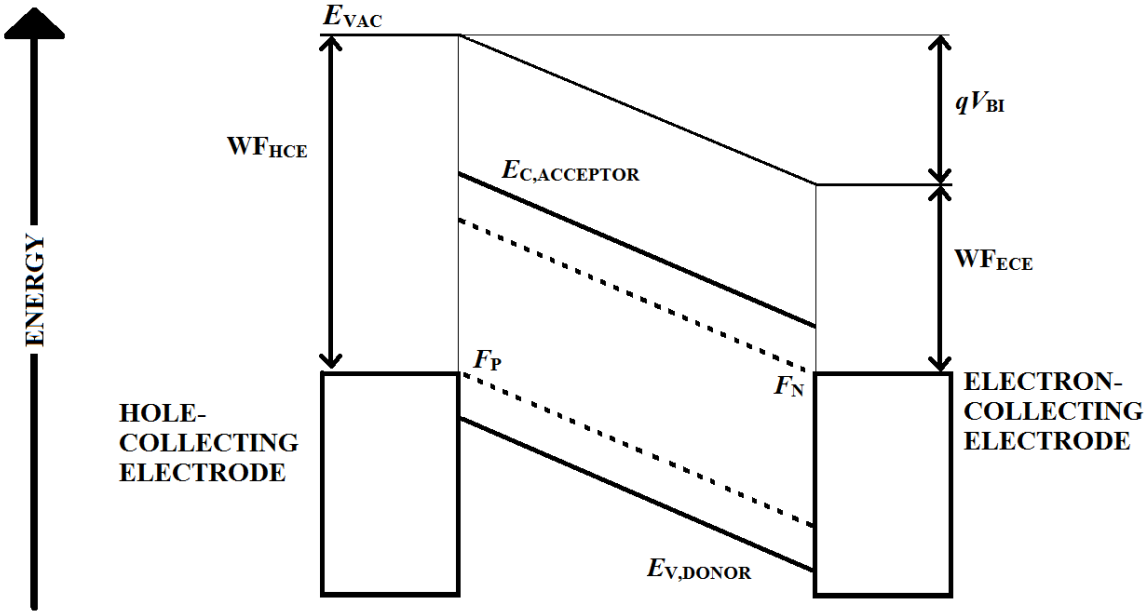

Figure 2.11. Energy band diagram of an OPV cell under quasi-equilibrium conditions under illumination at short-circuit.

At short circuit, the difference between the quasi-Fermi energy level for holes at the hole-collecting electrode and electrons at the electron-collecting electrode is zero, resulting in

no open-circuit voltage. However, the gradient of the quasi-Fermi levels is maximized, therefore yielding the maximum photocurrent for that particular level of irradiance.

Under illumination, at open circuit, the energy band diagram looks as shown in Figure 2.12.

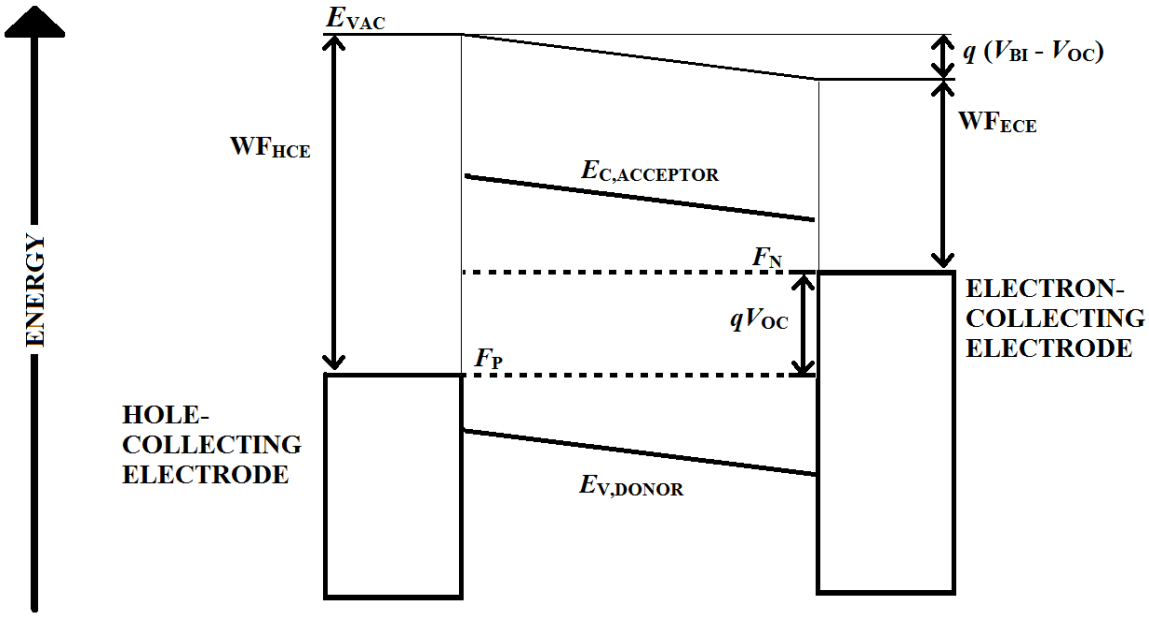

Figure 2.12. Energy band diagram of an OPV cell under quasi-equilibrium conditions under illumination at open-circuit.

At open circuit, the difference between the quasi-Fermi energy level for holes at the hole-collecting electrode and electrons at the electron-collecting electrode is maximized for that particular irradiance. However, since the quasi-Fermi levels are flat with respect to position, the photocurrent is zero.

2.4 Equivalent Circuit Model of a PV Cell

The equivalent circuit model, shown in Figure 2.13 [54], provides a simple methodology to simulate the current-voltage characteristics of PV in the dark and under

illumination. In addition, experimental data can be fit to the model, allowing relationships to be derived between various circuit parameters, which represent physical processes occurring within the PV cell.

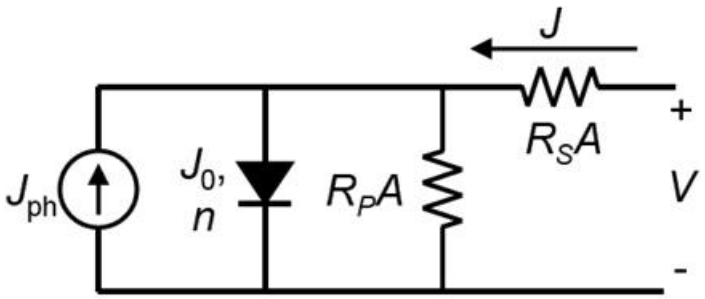

Figure 2.13. Equivalent circuit model of a photodiode.

In this model, the voltage across the PV cell terminals is represented by *V*. The current density through the terminals is represented by *J*. The rectifying nature of PV cells is conveyed by the diode element. The photogenerated current density of the PV cell in response to illumination is represented by the current source J_{ph}. Effects such as contact resistances and the bulk resistance of the photoactive layer are lumped into the area-scaled series resistance R_SA. The lumped area-scaled shunt resistance, R_PA, accounts for leakage current bypassing the diode through shunt paths between the electrodes due to imperfections in the film, such as pinholes.

Equating the current density entering and leaving the top node shown in the circuit leads to the equation:

$$J = J_0\left[\exp\left(\frac{V - JR_SA}{\frac{nkT}{q}}\right) - 1\right] + \frac{V - JR_SA}{R_PA} - J_{ph} \tag{2.27}$$

where J is the current density (typically in units of A cm^{-2}), J_0 is the reverse saturation current density (typically in units of A cm^{-2}), V is the voltage (typically in units of V), $R_S A$ is the area-scaled series resistance (typically in units of Ω cm^2), n is the diode ideality factor (unitless), k is Boltzmann's constant (typically in units of eV K^{-1}), T is the temperature (in units of K), $R_P A$ is the area-scaled parallel resistance (typically in units of Ω cm^2), and J_{ph} s the photogenerated current density (in units of mA cm^{-2}).

2.4.1 Diode Ideality Factor *n*

The diode ideality factor n provides insight into the dominant recombination mechanism within the photodiode. Physical values for n are between 1 and 2. These limits represent band-to-band and trap-assisted recombination, respectively. Changes in n influence the current in the photodiode under forward bias as shown in Figure 2.14.

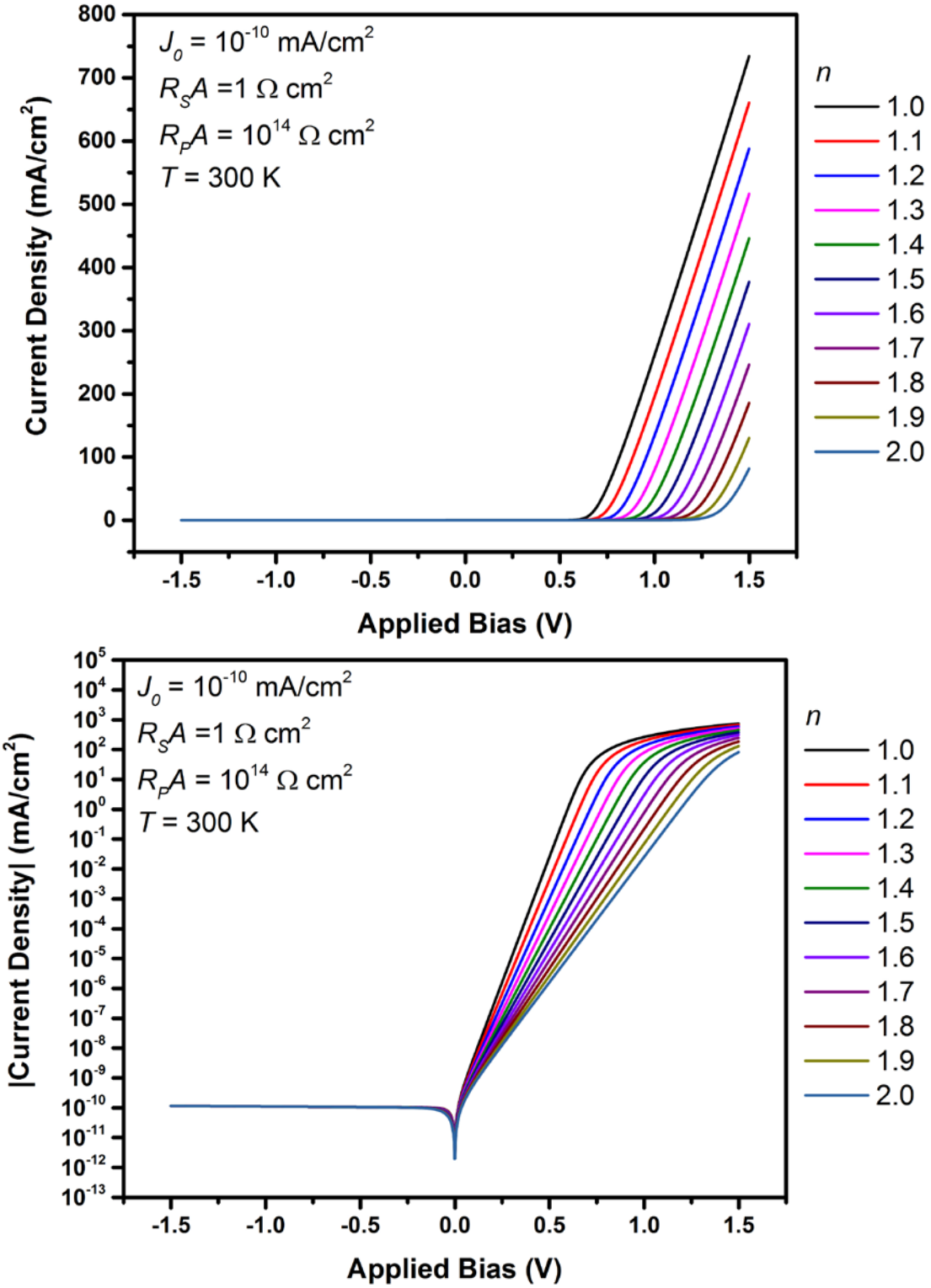

Figure 2.14. *J*–*V* curves in the dark generated from the equivalent circuit model, showing the effect of varying *n* in linear (top) and semilogarithmic (bottom) scales.

2.4.2 Reverse Saturation Current Density J_0

The current measured in an ideal diode under reverse bias in the dark approaches the reverse saturation current. Carriers that are thermally excited across the band gap contribute to J_0. Therefore, J_0 increases with temperature, since more carriers possess sufficient energy to cross the gap. In organic photodiodes, J_0 is related to the energetics of both the donor and acceptor materials. J_0 influences the current in the photodiode both under forward and reverse bias, as shown in Figure 2.15.

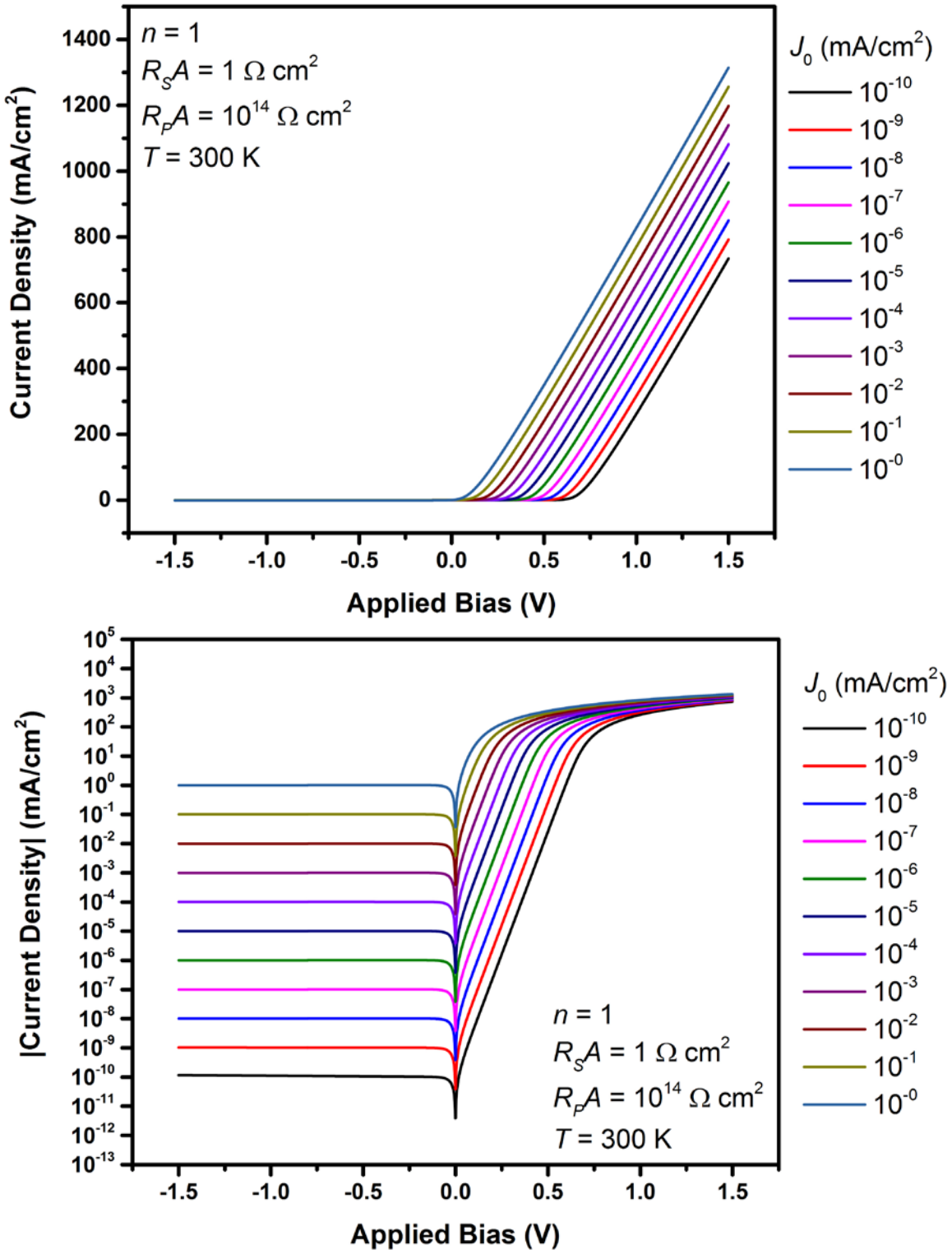

Figure 2.15. *J*–*V* curves in the dark generated from the equivalent circuit model, showing the effect of varying J_0 in linear (top) and semilogarithmic (bottom) scales.

2.4.3 Area-Scaled Series Resistance R_SA

The area-scaled series resistance, R_SA, is a measure of the resistance between the two electrodes as a result of effects such as the resistance within the electrodes, the contact resistance between the electrode and the semiconductor film, and the bulk resistance of the semiconductor film. The effects of series resistance begin to dominate at high applied bias. In an ideal photodiode, $R_SA = 0$. R_SA primarily influences the current in the PV cell under forward, as shown in Figure 2.16.

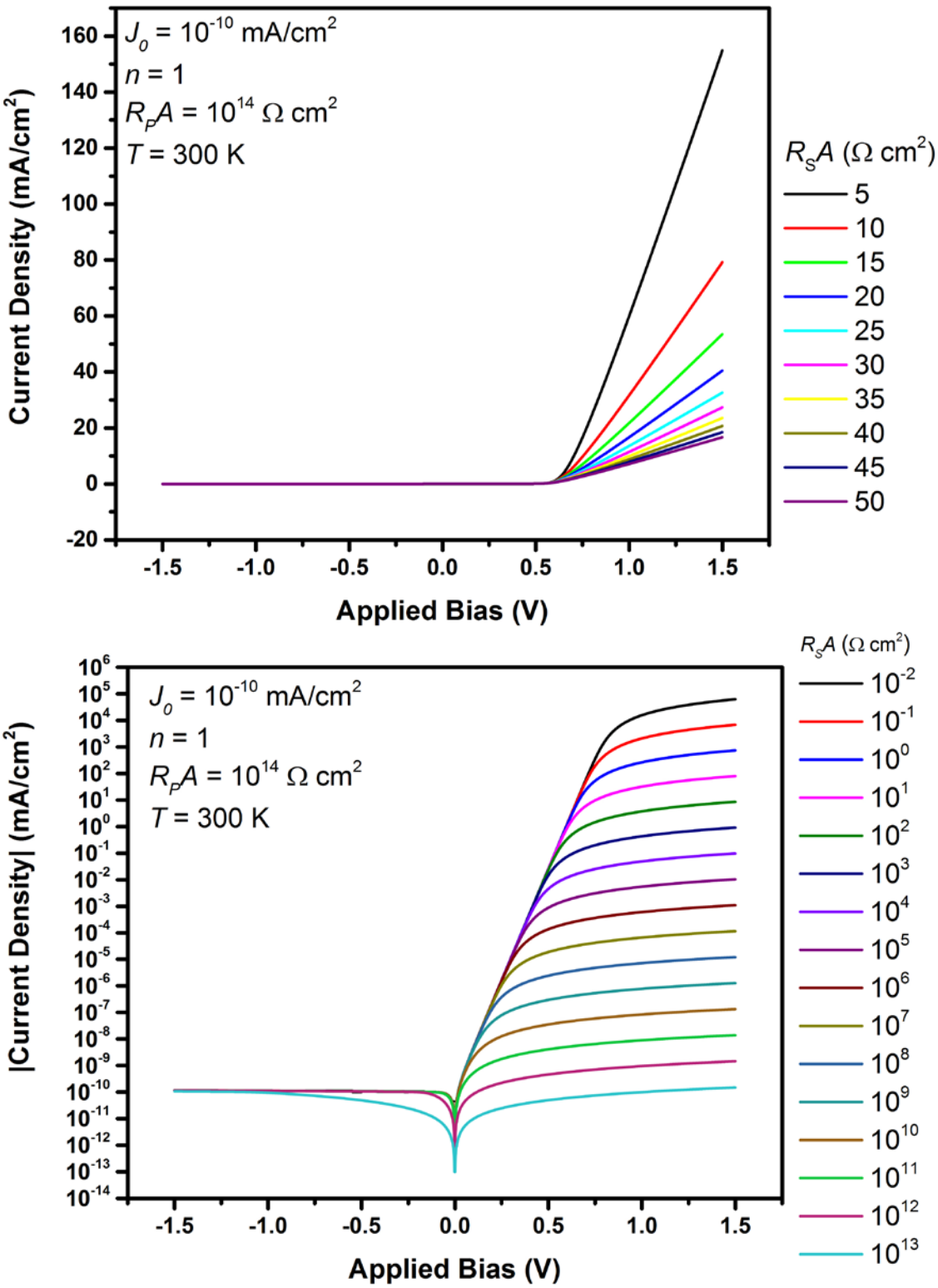

Figure 2.16. *J*–*V* curves in the dark generated from the equivalent circuit model, showing the effect of varying R_SA in linear (top) and semilogarithmic (bottom) scales.

2.4.4 Area-Scaled Parallel Resistance R_PA

In addition to J_0, the parallel resistance R_PA also relates to the current measured in the dark under reverse bias. In the limit of R_PA approaching infinity, the current under reverse bias saturates to J_0. However, as R_PA becomes smaller, a substantial leakage current begins to bypass the photodiode and flow through the leakage channels, which will dominate J_0 under reverse bias, as demonstrated below in Figure 2.17.

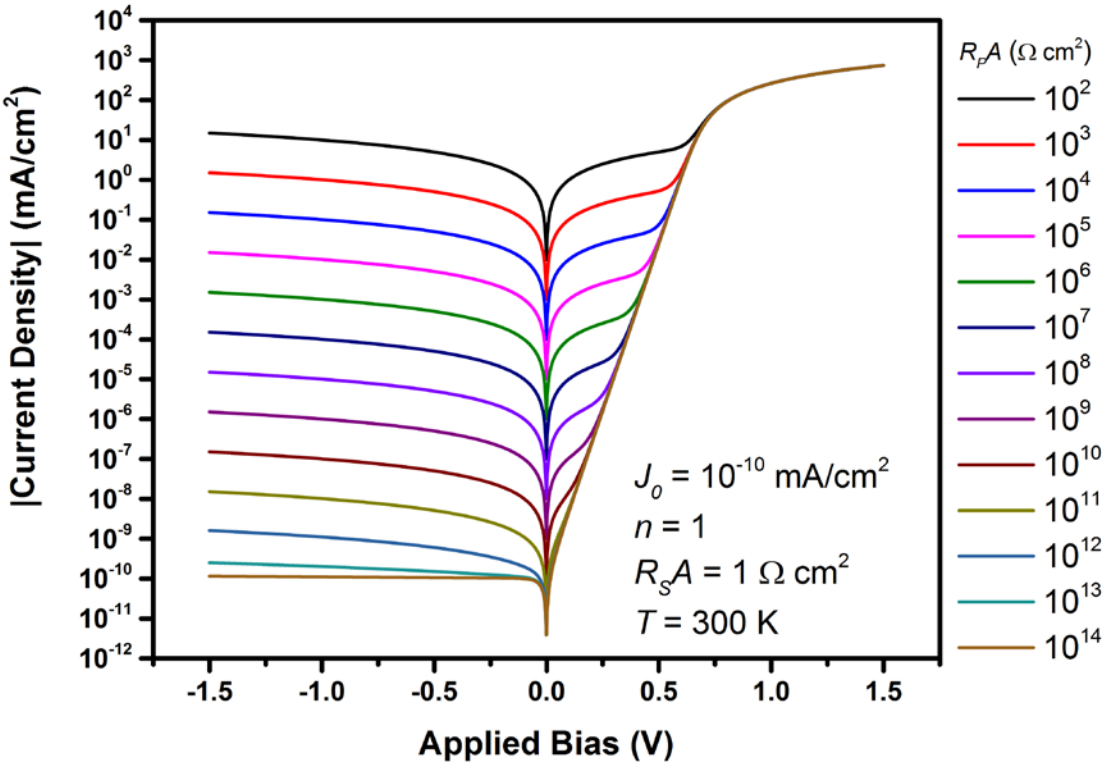

Figure 2.17. *J*−*V* curves in the dark generated from the equivalent circuit model, showing the effect of varying R_PA in semilogarithmic scale.

The parallel resistance-limited reverse bias leakage current also has an influence on the $J-V$ characteristics of the photodiode under illumination. The current measured in the dark under reverse bias acts as the bottom limit on the illumination detection, since the detection of photons is manifested in an increase in current. If the dark leakage current of a PV cell is high, the contribution of absorbed photons at low illumination levels may remain masked in the leakage current, thereby resulting in the photons going undetected. Figure 2.18 shows $J-V$ curves calculated using the equivalent circuit model of a photodiode, for a PV cell in which the parasitic $R_P A$ is limiting the current in reverse bias. In reverse bias, the current does not approach J_0. In addition, for the cases where J_{ph} is less than 10^{-5} mA/cm^2, all curves overlap, meaning that the PV cell is not sensitive enough to detect those levels of illumination, since the photogenerated current is smaller than the leakage current.

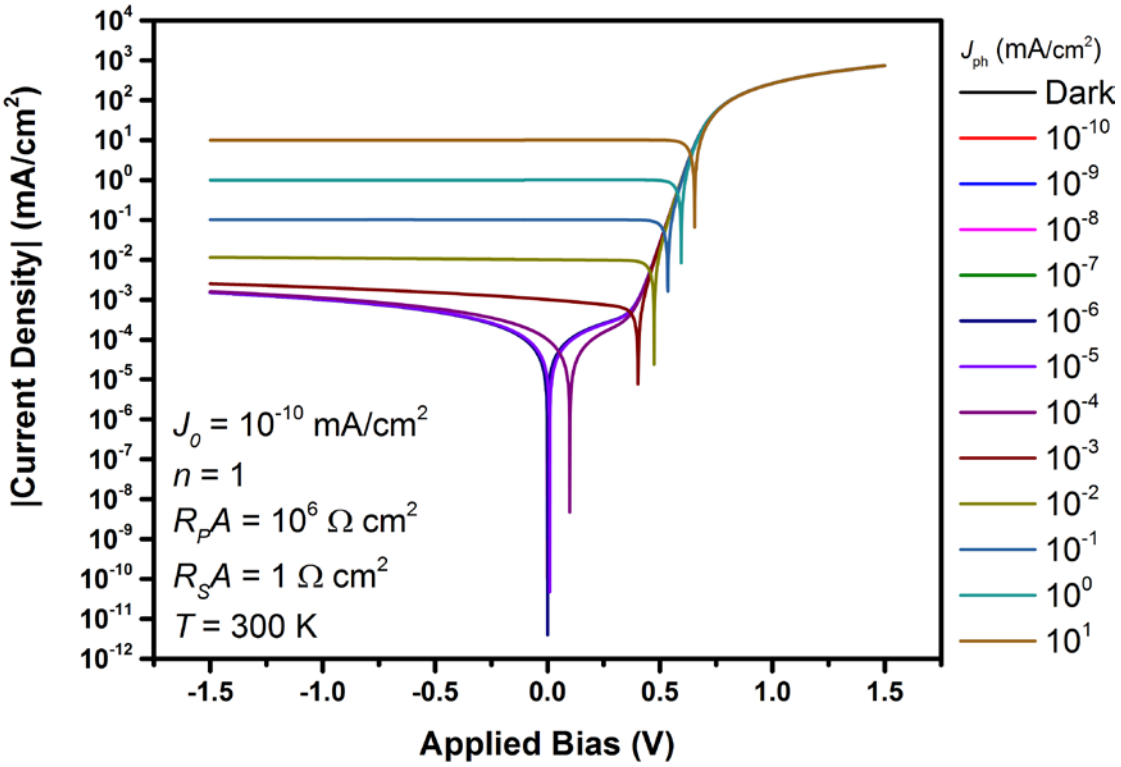

Figure 2.18. *J*−*V* curves under illumination generated from the equivalent circuit model, showing the effect of varying J_{ph} for a PV cell in which the parasitic R_PA limits the current in reverse bias, as shown in semilogarithmic scale.

This data can also be visualized as a collapse in linearity of the V_{OC} at lower irradiances when V_{OC} is plotted against J_{SC} on a semilogarithmic scale as shown in Figure 2.19.

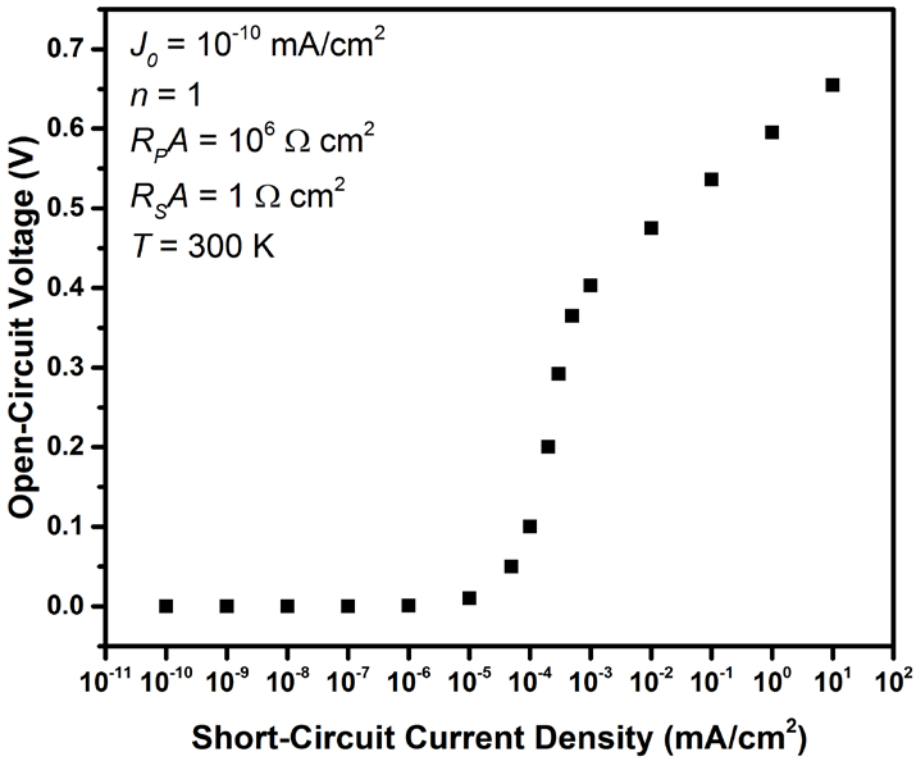

Figure 2.19. Collapse of the linearity in V_{OC} as a function of J_{SC} for a PV cell with low R_PA, as calculated by the equivalent circuit model and shown in semilogarithmic scale.

The other extreme case, where the parasitic R_PA does not limit the current in reverse bias is presented in Figure 2.20.

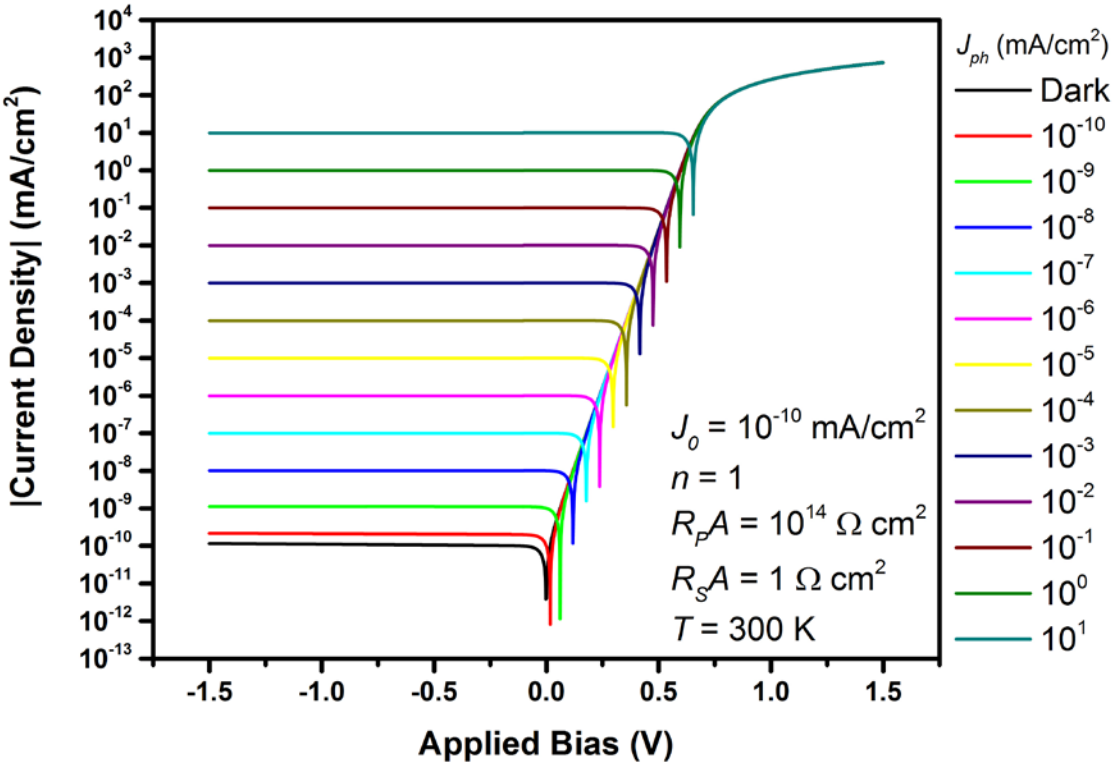

Figure 2.20. *J*−*V* curves under illumination, generated from the equivalent circuit model, showing the effect of varying J_{ph} for a PV cell in which the parasitic R_PA does not limit the current in reverse bias, as shown in semilogarithmic scale.

The high shunt resistance value means that the PV cell is sensitive to very small levels of illumination. A distinct response is visible even for $J_{ph} = 10^{-10}$ mA/cm^2.

CHAPTER 3

EXPERIMENTAL METHODS

In this chapter, experimental methods, including fabrication and characterization procedures for OPV and photodetectors, are discussed. While the OPV and photodetectors share many common fabrication steps, variations are distinguished as appropriate.

3.1 Fabrication Procedures

The OPV and photodetectors described in this dissertation were fabricated by an all-additive approach, wherein the various functional layers were sequentially deposited on top of the bottom indium tin oxide (ITO)-coated glass substrate. All functional layers were deposited by spin-coating from solution, other than the top metal electrodes, which were deposited by vacuum thermal evaporation.

OPV and photodetector samples were fabricated on 1” by 1” glass slides pre-coated with ITO. Each slide comprised of five individual OPV cells or photodetectors, as shown in the top view schematic of the completed samples in Figure 3.1, where the dotted region represents the active area, as described ahead.

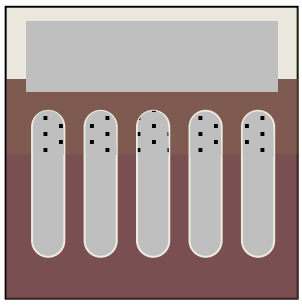

Figure 3.1. Top view schematic showing five samples on a single slide.

The active area of the OPV / photodetectors is the region where all of the functional layers intersect. In the case of OPV, these are the substrate (glass), the transparent conducting electrode (indium tin oxide (ITO)), the hole extraction layer (poly[3,4-ethylenedioxythiophene] polystyrene sulfonate (PEDOT:PSS)), the photoactive layer (poly[3-hexylthiophene]:indene C_{60}-bisadduct (P3HT:ICBA) or P3HT: phenyl-C_{61}-butyric acid methyl ester ($PC_{61}BM$) or P3HT:$PC_{71}BM$), the work function reducing interlayer (ethoxylated polyethylenimine (PEIE)), and the top metal electrode (aluminum (Al) or silver (Ag) or gold (Au)), as shown in Figure 3.2. For the photodetectors, the active area is composed of the substrate (glass), the transparent conducting electrode (ITO), the work function reducing interlayer (PEIE), the photoactive layer (P3HT:ICBA), the hole extraction layer (molybdenum oxide (MoO_3)), and the top metal electrode (Ag), as shown in Figure 3.2.

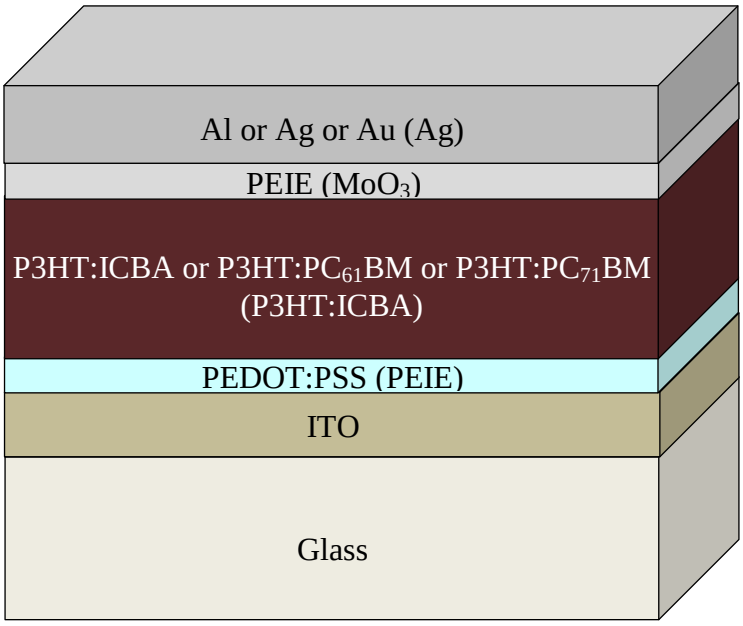

Figure 3.2. Cross section of the active area in OPV (photodetectors) showing the functional layers.

3.1.1 Substrate Preparation

Starting with commercially obtained ITO-coated glass sheets, substrate preparation involved cleaving of the sheets into smaller strips of a more manageable size, patterning of the bottom ITO electrode, and then thorough substrate cleaning.

ITO-coated polished soda lime float glass sheets (Colorado Concept Coatings, 130 nm thick ITO, 15 Ω/□, 14” by 14” by 0.043” sheet size) were cleaved into 4” by 1” strips using a table-top glass cutter (The Fletcher-Terry Company, 38WSCB-C-09/03) positioned above a cutting mat (Alvin BM 2436).

After cutting the ITO-coated glass sheets down to 4” by 1” strips, the ITO coating was then patterned. A portion of the ITO was removed in a defined pattern in order to produce a well-defined active area. An additional reason for patterning the ITO was that the top metal contacts of the completed OPV / photodetectors were electrically probed in the region where the conductive ITO had been removed, thereby eliminating the risk of shorting by punching through.

The glass / ITO strips were then covered lengthwise with 0.5” wide tape (Kapton) along one edge of the strip and etched in $HCl:HNO_3$ (3:1 v/v, 5 min, 80 °C). Following etching, the glass / ITO strips were then submerged in distilled water and visually inspected to ensure no ITO remained on the exposed portion.

After removing the tape, the patterned strips were thoroughly scrubbed with detergent (Alconox Liqui-Nox). The patterned ITO strips were then cut into 1” x 1” pieces after rinsing in distilled water and drying under a stream of nitrogen. Then, the glass / ITO pieces were ultrasonically solvent cleaned (Branson 5510, 20 min, 45 °C) in sequential baths of detergent in distilled water, distilled water alone, 2-propanone, and 2-

propanol. Finally, each glass / ITO slide was individually dried under a stream of nitrogen.

3.1.2 Hole Extraction Layer Deposition (for OPV)

After substrate patterning and cleaning, the glass / ITO slides were subjected to oxygen plasma (Plasmatic Systems PlasmaPreen #862, 2 min) in order to improve the wetting of subsequent layers by increasing the surface energy. Following the oxygen plasma treatment, the glass / ITO slides were immediately spin-coated (Laurell Technologies WS-400B-6NPP-Lite) with a low-conductivity grade conducting polymer dispersion PEDOT:PSS (Heraeus CLEVIOS P VP AI 4083, 5000 RPM, 60 s, 928 RPM/s) through a 13 mm filter of pore size 0.45 µm, in ambient air atmosphere. The slides were then thermally annealed on a hot plate (140 °C, 10 min). This recipe yielded PEDOT:PSS films 45 nm in thickness, as measured by variable angle spectroscopic ellipsometry. Following cool down, the glass / ITO / PEDOT:PSS slides were transferred to a nitrogen-filled glovebox for further processing.

3.1.3 Work Function Reducing Polymer Deposition (for photodetectors)

After substrate patterning and cleaning, the glass / ITO slides were spin-coated with a solution of PEIE (Sigma-Aldrich 423475, 35-40 wt. % in H_2O, average M_W ~ 70,000). PEIE had previously been diluted in 2-methoxyethanol (Sigma-Aldrich 284467, anhydrous, 99.8%) to a concentration of 0.4 wt. % and magnetically stirred overnight. PEIE was then dispensed onto the patterned ITO substrates through 0.2 µm pore size filters and spin-coated at a spin speed of 5,000 RPM, with acceleration of 928 RPM/s for

60 s, followed by thermal annealing on a hot plate at 100 °C for 10 min. The PEIE-coated ITO substrates were then transferred into a nitrogen-containing glovebox for further processing.

3.1.4 Photoactive Layer Deposition

The photoactive layers studied as part of the research were based on the donor polymer poly(3-hexylthiophene) (P3HT) and three different fullerene-derivative acceptor molecules, phenyl-C_{61}-butyric acid methyl ester ($PC_{61}BM$), phenyl-C_{71}-butyric acid methyl ester ($PC_{71}BM$), or indene C_{60}-bisadduct (ICBA). All photoactive layers presented in this dissertation were spin-coated from solution.

Prior to deposition of the photoactive layers, solutions of the donor and acceptor components were prepared. P3HT (Rieke Metals Inc. 4002-E, Average molecular weight 50,000 - 70,000 g/mol) was weighed out on weighing paper on a digital scale (Sartorius TE124S) and added to a vial in air. Then, the fullerene-derivative acceptors (ICBA: Luminescence Technology Corp. S9030, or $PC_{61}BM$: Nano-C, or $PC_{71}BM$: Nano-C) were weighed out in the same manner and added to the vial. The masses and weight ratios of the donor and acceptor components varied depending upon the desired film thickness. The OPV were fabricated using P3HT:ICBA, P3HT:$PC_{61}BM$, or P3HT:$PC_{71}BM$ solutions in the weight ratio 1:1 with concentration 40 mg/ml to yield 200 nm thick films. The photodetectors were made using two different concentrations of P3HT:ICBA. 80 mg/ml P3HT:ICBA solutions yielded films of thickness 500 nm, whereas, 120 mg/ml solutions resulted in 1 μm-thick films. Finally, a magnetic stir bar was added to the vial and the vial was transferred into a nitrogen-filled glovebox.

After transferring to the glovebox, 1,2-dichlorobenzene (Sigma-Aldrich 240664) solvent was added to the vial using a micropipette. The solutions were stirred overnight on a magnetic hotplate set to 70 °C and stirring at 500 rpm.

The photoactive layer solutions were then spin-coated on the glass / ITO / PEDOT:PSS (for OPV) or glass / ITO / PEIE (for photodetectors) slides. Solution was dispensed onto the slides through a 13 mm diameter filter of pore size 0.20 µm. After covering the entire slide with drops of the solution, the slides were spin-coated at 800 RPM for 30 s at an acceleration of 10000 RPM/s.

To produce crystalline films, the freshly spin-coated still wet films were placed in covered glass Petri dishes to slowly dry for more than 6 h in the atmosphere of the solvent vapors in a so-called solvent annealing process. The photodetector samples were then thermally annealed on a hot plate set to 150 °C for 10 min.

3.1.5 Work Function Reducing Polymer Deposition (for OPV)

After spin-coating and solvent annealing the photoactive layer, the glass / ITO / PEDOT:PSS / P3HT:(ICBA or $PC_{61}BM$ or $PC_{71}BM$) slides were removed from the glovebox and exposed to a brief flash of oxygen plasma. PEIE had previously been diluted in 2-methoxyethanol (0.025 wt % for OPV with Al electrodes, 0.05 wt % for Ag, 0.1 wt % for Au) and magnetically stirred overnight before spin coating. The PEIE solution was spin-coated on top of P3HT:ICBA in air (13 mm diameter filter, filter pore size 0.20 µm, 5000 RPM, 60 s, 928 RPM/s), after which the slides were transferred back into the glove box and thermally annealed (150 °C, 10 min).

3.1.6 Buried ITO Electrode Liberation

Since the photoactive layer was coated on the entire area of the slide, a portion of it was removed in order to allow contact to be made to the buried ITO electrode. A piece of non-woven polyester/cellulose paper was folded and clamped in a pair of Teflon forceps and then wet with chlorobenzene. A portion of the photoactive layer was dissolved by wiping with the paper.

3.1.7 Top Electrode Deposition

The slides were then mounted on a sample holder with Kapton tape and placed in contact with a shadow mask, through which the top metal electrode deposition was conducted. The mask defined 5 individual "finger" electrodes, in addition to a rectangular pad that made contact to the ITO. The active area of the OPV and photodetectors was 0.1 cm^2.

The top metal electrodes were deposited by vacuum thermal evaporation (Kurt J. Lesker SPECTROS). The evaporator was integrated to the nitrogen-filled glovebox, such that the door to the vacuum chamber opened to the glovebox and was never exposed to ambient atmosphere. All depositions were conducted at a pressure less than 10^{-6} Torr and a deposition rate between 0.5 and 1.5 Å/s.

For OPV, the top metal electrode used was 150 nm of Al, Ag, or Au. For photodetectors, 10 nm MoO_3 was first deposited as the charge extraction layer, followed by 150 nm of the top electrode Ag. A photograph of a finished sample is shown in Figure 3.3.

Figure 3.3. Photograph of a completed sample.

3.2 Characterization Procedures

3.2.1 Film Thickness Characterization

The thickness of the photoactive layer was characterized using two different methods: stylus profilometry (Veeco Dektak) and variable angle spectroscopic ellipsometry (J. A. Woollam Co., Inc. M2000).

Profilometry is a physical approach of thickness measurement in which the displacement of a stylus tip is recorded as it moves across hills and valleys in a film.

Ellipsometry is an optical approach of thickness measurement in which the change in polarization of light after reflecting off of the sample is recorded both as a function of the light source wavelength and angle of the light source. Based on the nature of the film (absorbing, non-absorbing, metallic, etc.), the polarization data can be fit to an appropriate model, in which the thickness is a fitting parameter.

For stylus profilometry, a scratch was made in the soft organic films deposited on glass slides and then a stylus was scanned across the trench created by the scratch. The recorded displacement of the stylus allowed the thickness to be determined.

For variable angle spectroscopic ellipsometry, the relevant film was first deposited on a glass substrate. Then, tape was adhered to the backside of the glass to eliminate backside reflections contributing to the detected reflected signal. The change in polarization data was fit to a Cauchy model [55] for transparent films between wavelengths of 1200 nm to 1600 nm where the organic semiconductor did not absorb.

3.2.2 Room Temperature Current-Voltage Characterization

Following top-metal electrode deposition, samples were transferred into another nitrogen containing glove box for electrical characterization. Current density-voltage ($J-V$) curves were collected in the dark and under illumination using a custom-written LabVIEW program that interfaced with a digital source-measurement unit (Keithley Model 2400 SourceMeter). Illumination was provided by a solar simulator (Oriel 91160) equipped with a 300 Watt xenon arc lamp (Newport 6258) and an Air Mass 1.5 Global filter. The illumination irradiance was calibrated to 100 mW/cm^2 using a silicon photodiode (Hamamatsu S1133).

3.2.3 Electrical Characterization as a Function of Irradiance and Temperature

Variable irradiance and temperature electrical characterization of the photodetector samples was conducted inside a cryostat (Janis VPF-500). The cryostat was loaded into a nitrogen-filled glovebox, where thermal grease (DuPont Krytox LVP High Vacuum Grease) was applied to its cold-finger sample holder. The sample was mounted on the cold-finger, probe tips were used to make contact with all six electrodes, and the cryostat was sealed. After removing the cryostat from the glovebox, it was connected to

an integrated scroll / turbo pump system (Edwards EXPT Pumping Station), using which, the pressure of the cryostat was reduced to less than 4×10^{-7} Torr.

The temperature of the cryostat cold finger was controlled by means of a LakeShore 331 Temperature Controller, which interfaced with a resistive heater built into the base of the cold finger. Current-voltage data was collected for temperatures of 297 K (no heat supplied), 320 K, 340 K, and 360 K. To ensure the temperature had stabilized, current was constantly monitored at a fixed applied voltage bias. Current-voltage data at the new temperature set point was acquired once the current had stabilized.

Electrical connections to the sample inside the cryostat were routed to an electrometer (Keithley 6517A), which supplied voltage and measured current. The data acquisition was controlled by a custom-written LabVIEW program.

Optical illumination to the sample was provided through a window in the cryostat, using the output of a white LED (Super Bright LEDs RL5-W8045), which was driven by a DC power supply (Agilent 3647A).The drive voltage was reduced to lower the irradiance of the LED.

3.2.4 Spectral Responsivity and External Quantum Efficiency Characterization

The optical output of a lamp (CVI Spectral Products CERMAX) coupled with a monochromator (CVI Spectral Products CM110) was focused using optical lenses and mirrors onto the photodetector active area mounted inside a cryostat. An electrometer (Keithley 6517A) was used to make electrical contact to the sample inside the cryostat. A custom-written LabVIEW program was used to communicate with the monochromator over serial connection to vary the wavelengths. An optical power meter (OPHIR)

equipped with a calibrated silicon photodiode was used to measure the optical power at each wavelength right outside the cryostat window. High wavelength pass filters were placed in the beam path to avoid multiple frequency harmonic. The spectral responsivity was obtained by normalizing the photogenerated current measured at each wavelength by the optical power.

3.2.5 Ionizing Radiation Detection

The detector was used to detect ionizing radiation using the experimental test set up shown in Figure 3.4 below:

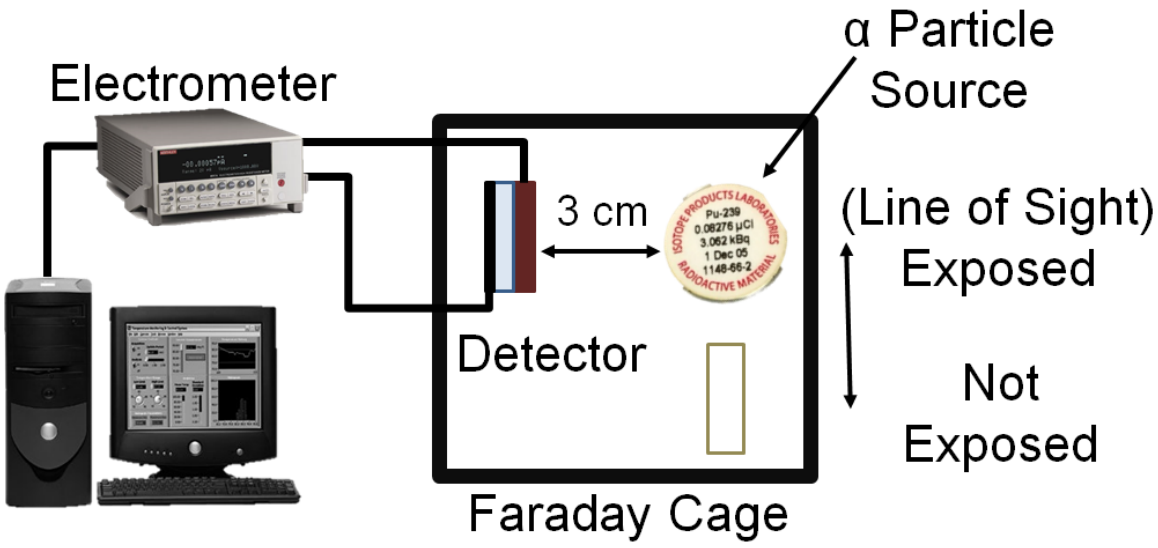

Figure 3.4. Experimental set up used to sense ionizing radiation.

The sample was mounted inside a Faraday cage and contacted via alligator clips that interfaced to a Keithley 6517A electrometer. The current was measured as a function of time using a custom-written LabVIEW program that could also source voltage to the

terminals of the detector. A plutonium-239 alpha particle source was mounted 3 cm away from the sample, facing the metal electrodes side. The alpha particle source was then moved out of line of sight and changes to the output current of the detector were monitored. The entire experimental test setup was housed underneath an optical dark cloth to eliminate any ambient room light contribution to the current output of the detector.

CHAPTER 4

ENHANCING THE ENVIRONMENTAL STABILITY OF ORGANIC SEMICONDUCTOR PHOTOVOLTAIC CELLS

The environmental stability of OPV is an important area of study, especially as the technology is maturing from academic research toward adoption in commercial products. This chapter describes the novel OPV structures that were conceived and implemented as part of the research to enhance the operating lifetime of OPV while maintaining the power conversion efficiency.

4.1 The Use of Calcium in OPV

As discussed in Chapter 2, the photoactive layer in bulk heterojunction OPV is composed of a blend of a donor and acceptor material, distributed throughout the volume of the film and sandwiched between electron- and hole-collecting electrodes. A large contrast between the work function of the electron- and hole-collecting electrodes is necessary so as not to limit the V_{OC} generated by the cell. Therefore, Ca is often employed as the electron-collecting electrode because of its low work function of 2.7 eV [56].

4.2 Disadvantages of Using Calcium Electron-Collecting Electrodes

The use of Ca electrodes in OPV leads to two major disadvantages. First, Ca readily reacts with oxygen in air, upon which, it converts to calcium oxide according to:

$$2\mathrm{Ca} + \mathrm{O}_2 \rightarrow 2\mathrm{CaO} \tag{4.1}$$

The following video shows the effects of air exposure on a 200 nm film of Ca deposited on a glass substrate, when it is removed from a nitrogen-filled glovebox. Starting out as reflective and shiny, the film becomes increasingly transparent within seconds.

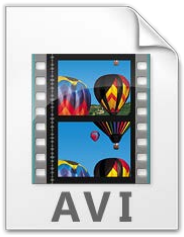

Figure 4.1. Rapid oxidation of a 200 nm thick film of calcium upon exposure to air. (CalciumInAir.avi, 7.03 MB)

Secondly, Ca has a smaller reflectance than other metals such as Al and Ag [57]. As a result, fewer photons are absorbed in the photoactive layer during the second pass after reflection from the top metal electrode, thereby reducing J_{SC}. Therefore, it is important to develop efficient OPV that do not contain Ca.

4.3 Approach to Replace Calcium Electron-Collecting Electrodes

In previous work in our research group, it has been demonstrated that the work function of a wide variety of conductors, including metals, metal oxides, and conducting polymers, was substantially reduced by coating ethoxylated polyethylenimine (PEIE) atop them [58]. This technique directly lent itself to the fabrication of inverted geometry

OPV, where other functional layers were deposited upon the polymer-modified low-work-function electrode surfaces.

In the course of our research project, it was discovered that the low-work-function interface could also be produced by reversing the order of deposition, i.e., by depositing various conductors on top of PEIE, facilitating the development of Ca-free conventional geometry OPV [59]. As a result, efficient electron collection was achieved with a variety of electrode metals such as Al, Ag, and Au, in the OPV structure glass / ITO / PEDOT:PSS / P3HT:(ICBA or $PC_{61}BM$ or $PC_{71}BM$) / PEIE / (Al or Ag or Au), as shown in Figure 4.2 (a).

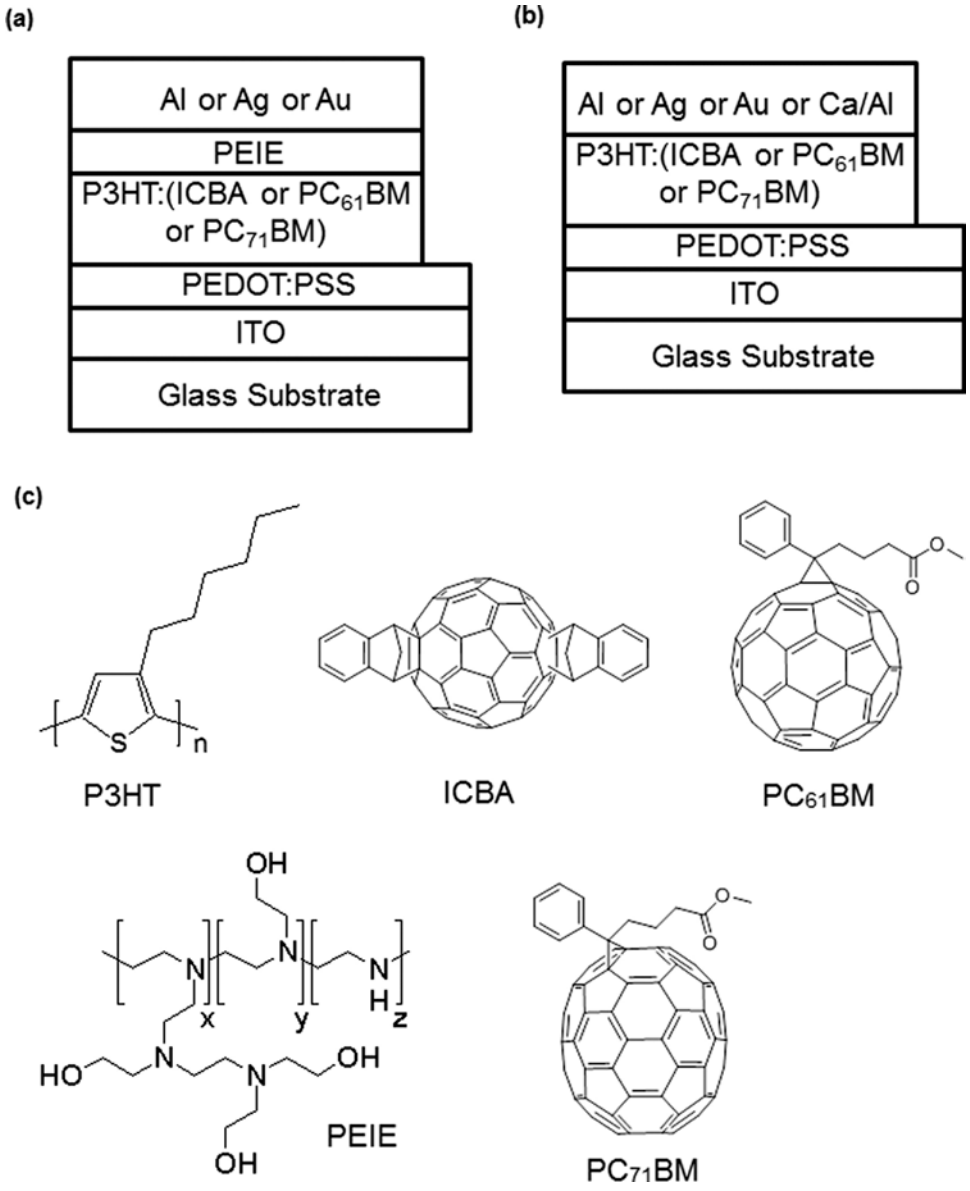

Figure 4.2. (a) Structure of OPV with PEIE interfacial modification.
(b) Structure of the reference OPV.
(c) Chemical structures of the materials used in this study.

(Reprinted with permission from Talha M. Khan et al. *ACS Applied Materials & Interfaces* **2014** *6* (9), 6202-6207. Copyright (2014) American Chemical Society)

4.4 Results

4.4.1 Development of a Methodology to Deposit PEIE on the Hydrophobic Photoactive Layer Surface

The deposition of PEIE from 2-methoxyethanol solvent on the hydrophobic surface of P3HT-based photoactive layers required prior surface treatment, such as a brief flash of oxygen plasma, to turn the surface more hydrophilic. Figure 4.A shows XPS surveys conducted on the surface of pristine P3HT:ICBA, P3HT:ICBA on which PEIE was spun without plasma treatment, and P3HT:ICBA on which PEIE was spun with prior oxygen plasma treatment. The emergence of the N 1s peak confirms the presence of PEIE on the surface. Nitrogen is an appropriate identifier element because it is not present in the chemical structures of either P3HT or ICBA. As shown in Figure 4.3, N 1s is only observed when PEIE was spun on the oxygen plasma-treated P3HT:ICBA surface.

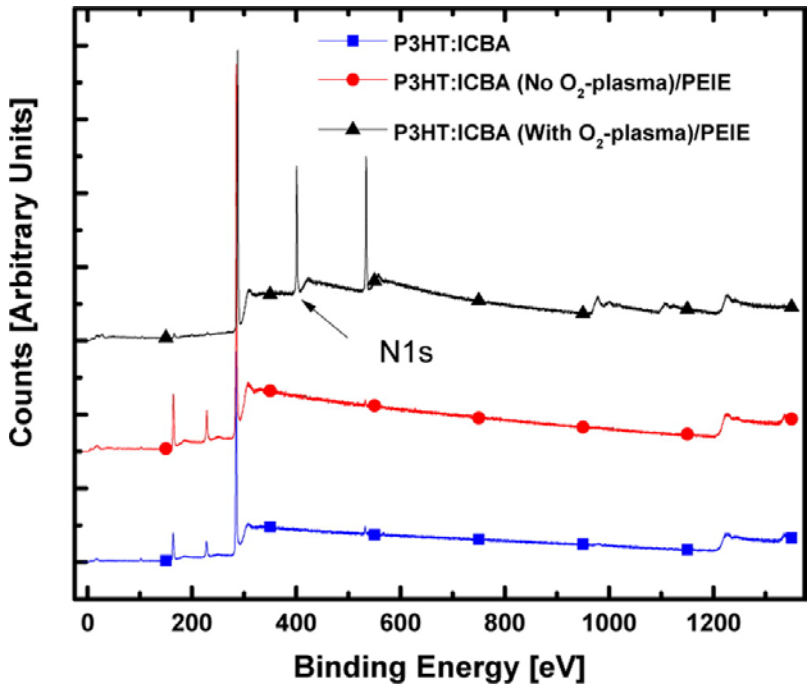

Figure 4.3. XPS spectra taken on the surface of pristine P3HT:ICBA (blue squares), P3HT:ICBA with PEIE spin-coated on top without surface treatment (red circles), and P3HT:ICBA when PEIE was spin-coated on top with a brief flash of O_2-plasma (black triangles).

(Reprinted with permission from Talha M. Khan et al. *ACS Applied Materials & Interfaces* **2014** *6* (9), 6202-6207. Copyright (2014) American Chemical Society)

4.4.2 Calcium-Free OPV with PEIE-Modified Aluminum Electron-Collecting Electrodes

A study of the performance of OPV with both P3HT:ICBA and P3HT:PCBM as the active layers with Al electron-collecting electrodes is first presented. ICBA is widely used as the acceptor material in OPV because it yields higher V_{OC} as compared to PCBM, when blended with P3HT [60].

4.4.2.1 Effects of Thermal Annealing on Glass / ITO / PEDOT:PSS / P3HT:ICBA /Al OPV

It has previously been shown that OPV based on P3HT:$PC_{61}BM$ with the structure ITO / PEDOT:PSS / P3HT:$PC_{61}BM$ / Al demonstrated a high fill factor (FF) of 68% without using Ca or other interfacial modifiers by thermally annealing the completed OPV at 150 °C, after the Al top metal electrode deposition, for 30 min [33]. However, P3HT:ICBA-based OPV with the analogous structure ITO / PEDOT:PSS / P3HT:ICBA / Al, were found to yield poor FF when the OPV were either thermally annealed before Al top electrode deposition ("pre-annealing"; FF = 0.41 ± 0.01) or after ("post-annealing"; FF = 0.55 ± 0.01). Representative *J–V* characteristics of these OPV are respectively shown in Figure 4.4 (a) and (b). The OPV exhibited poor rectification in the dark and inflection in the curves under illumination. This illustrates the poor electron collection of the Al electrode in OPV containing P3HT:ICBA photoactive layers.

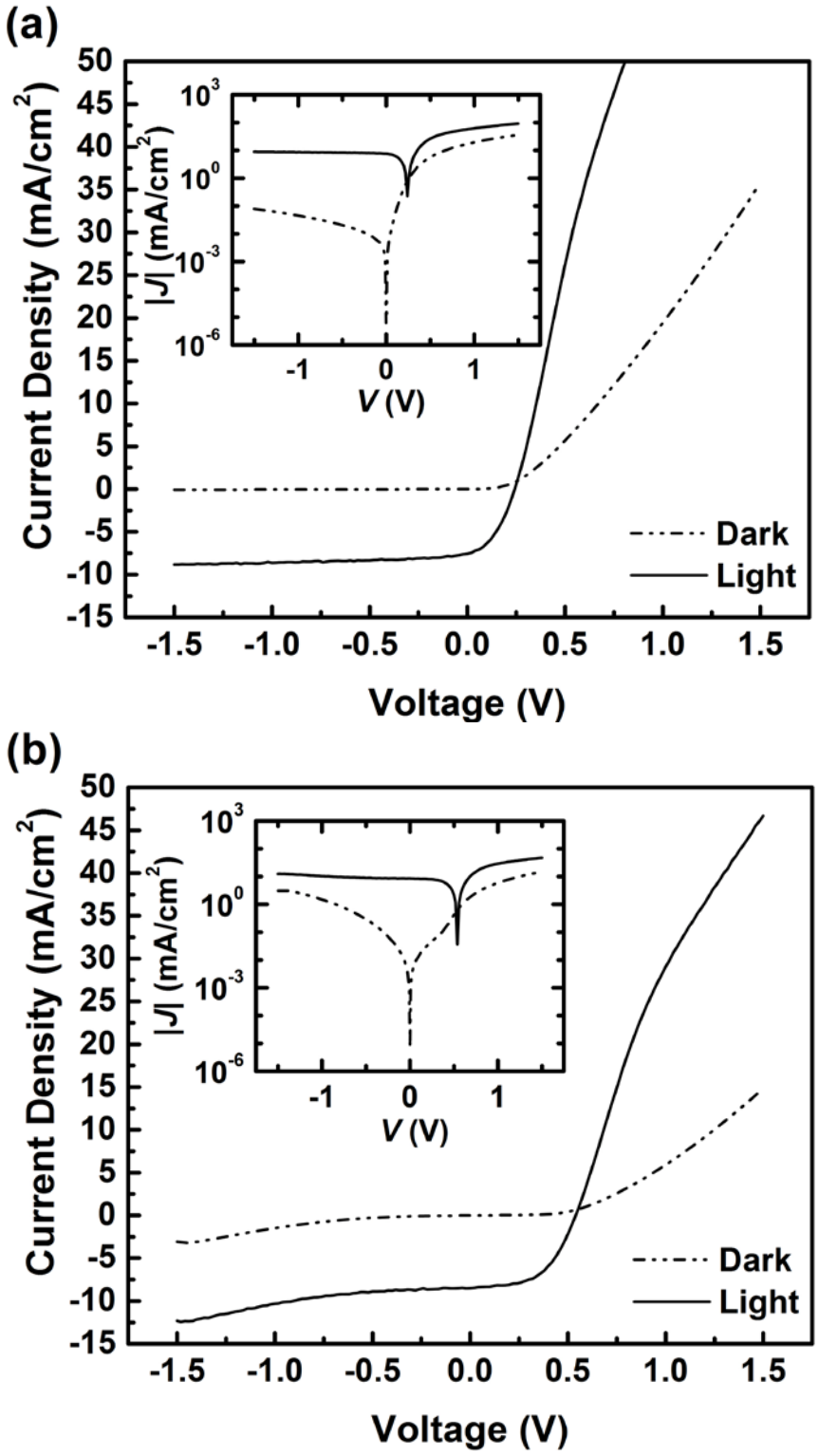

Figure 4.4. Representative *J–V* characteristics for OPV in the structure glass / ITO / PEDOT:PSS / P3HT:ICBA / Al where the sample was thermally annealed (a) before top metal deposition and (b) after top metal deposition. The insets show the *J–V* characteristics on a semilogarithmic scale.

(Adapted with permission from Talha M. Khan et al. *ACS Applied Materials & Interfaces* **2014** *6* (9), 6202-6207. Copyright (2014) American Chemical Society)

4.4.2.2 Improvement of Electron Collection at the Aluminum Top Electrode with PEIE

Figure 4.5 shows representative *J–V* characteristics for OPV with the structure ITO / PEDOT:PSS / P3HT:ICBA / PEIE / Al, in which PEIE was spin-coated on the O_2-plasma treated P3HT:ICBA photoactive layer prior to deposition of Al as the electron-collecting top metal electrode.

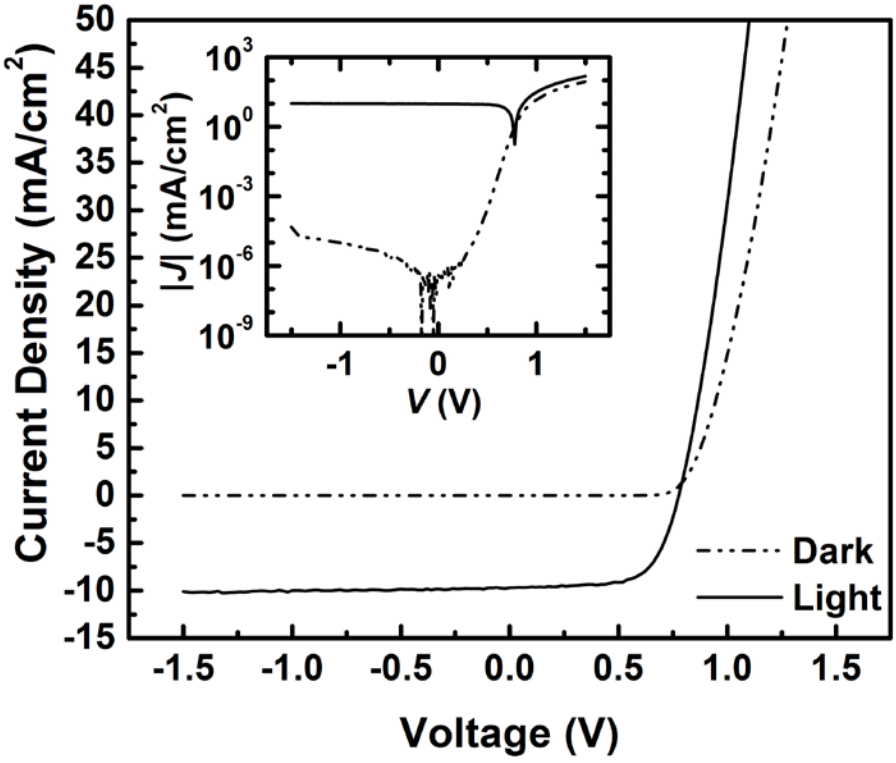

Figure 4.5. Representative *J–V* characteristics for OPV with structure glass / ITO / PEDOT:PSS / P3HT: ICBA / PEIE / Al. The inset shows the *J–V* characteristics on a semilogarithmic scale.

(Adapted with permission from Talha M. Khan et al. *ACS Applied Materials & Interfaces* **2014** *6* (9), 6202-6207. Copyright (2014) American Chemical Society)

The presence of PEIE substantially improved the photovoltaic performance as compared to OPV with the structure ITO / PEDOT:PSS / P3HT:ICBA / Al. OPV containing PEIE / Al electron-collecting electrodes yielded average values of V_{OC} = 775 ± 6 mV, J_{SC} = 9.1 ± 0.5 mA cm^{-2}, FF = 0.65 ± 0.01, and PCE = 4.6 ± 0.3% (averaged over five OPV cells. The presence of PEIE at the electron-collecting interface also reduced the dark current under reverse bias by a factor of 1000. Glass / ITO / PEDOT:PSS / P3HT:ICBA / Al OPV averaged a dark current values of of (-7 ± 2) × 10^{-5} A/cm^2 at -1.5 V averaged over ten OPV cells, while glass / ITO / PEDOT:PSS / P3HT:ICBA / PEIE / Al OPV showed a dark current of (-8 ± 6) × 10^{-8} A/cm^2 at -1.5 V, averaged over four OPV cells.

The PCE in OPV containing PEIE-modified Al electron collecting electrodes was comparable to that attained when using Ca electron-collecting top metal electrodes with the structure ITO / PEDOT:PSS / P3HT:ICBA / Ca / Al, for which representative the *J*–*V* characteristics are shown in Figure 4.6:

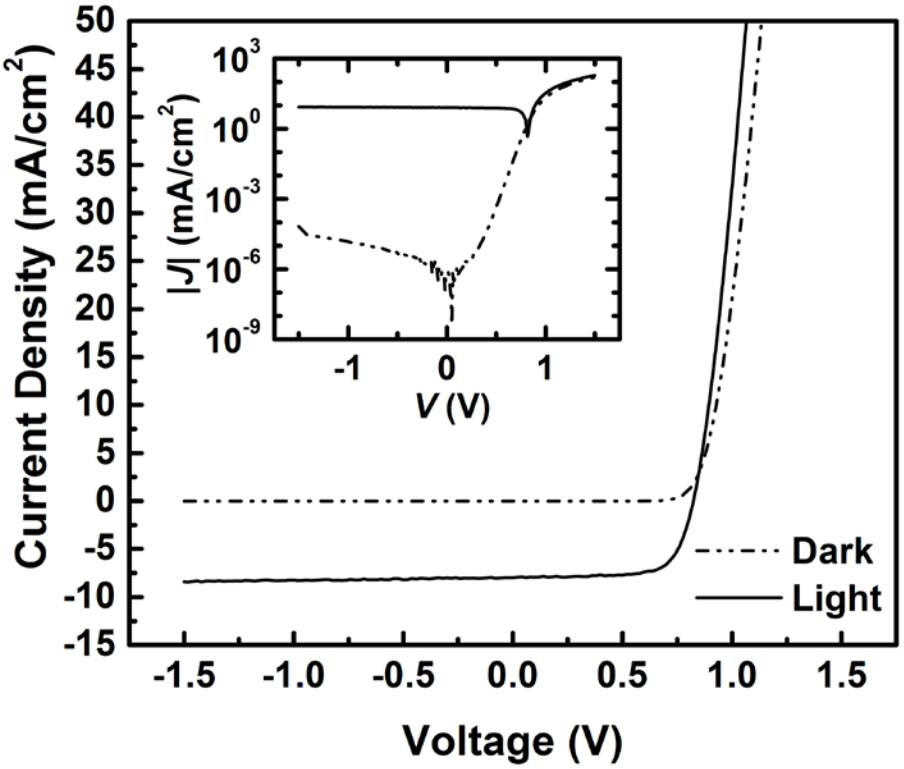

Figure 4.6. Representative *J–V* characteristics for OPV with structure glass / ITO / PEDOT:PSS / P3HT: ICBA / Ca / Al. The inset shows the *J–V* characteristics on a semilogarithmic scale.

Although the V_{OC} obtained in the case of OPV with PEIE / Al electron-collecting electrodes (775 ± 6 mV) was lower than that for OPV with Ca / Al electrodes (822 ± 4 mV), the higher reflectivity of Al resulted in a greater J_{SC} (9.1 ± 0.5 mA/cm^2) compared with OPV containing Ca electrodes (8.0 ± 0.1 mA/cm^2). This is due to an increase in the second pass contribution to J_{SC} after light reflects back into the photoactive layer from the metal electrode, compensating for the lower V_{OC} value.

4.4.2.3 Control Experiments

The deposition of PEIE prior to the evaporation of the Al electron-collecting electrode led to significant improvements in OPV performance, as shown in the previous

section. However, the deposition of PEIE required two additional steps, as compared to reference OPV. The first was the prior flash of oxygen plasma on the photoactive layer surface to make it hydrophilic and allow the deposition of PEIE, and the second was the spin-coating of PEIE from 2-methoxyethanol solvent on the photoactive layer. Two sets of control experiments were thus performed to confirm whether PEIE was indeed responsible for the improvements in OPV performance.

4.4.2.3.1 Effect on OPV Performance of the Flash of Oxygen Plasma on the Photoactive Layer

The effect of the flash of O_2-plasma alone on the photoactive layer without either solvent or PEIE treatment on OPV performance was studied in the structure glass / ITO / PEDOT:PSS / P3HT:ICBA (O_2-Plasma treated) / Al**.** The *J*−*V* characteristics of a representative OPV cell are shown in Figure 4.7. The OPV demonstrated values of V_{OC} = 270 ± 36 mV, J_{SC} = 5.8 ± 0.3 mA cm^{-2}, FF = 0.42 ± 0.02, and PCE = 0.7 ± 0.1 %, averaged over nine OPV cells. The OPV performance was significantly worse than the case in which the photoactive layer O_2-plasma surface treatment was followed by the spin-coating of PEIE from 2-methoxyethanol solvent, leading to the conclusion that the flash plasma treatment alone was not responsible for OPV improvement.

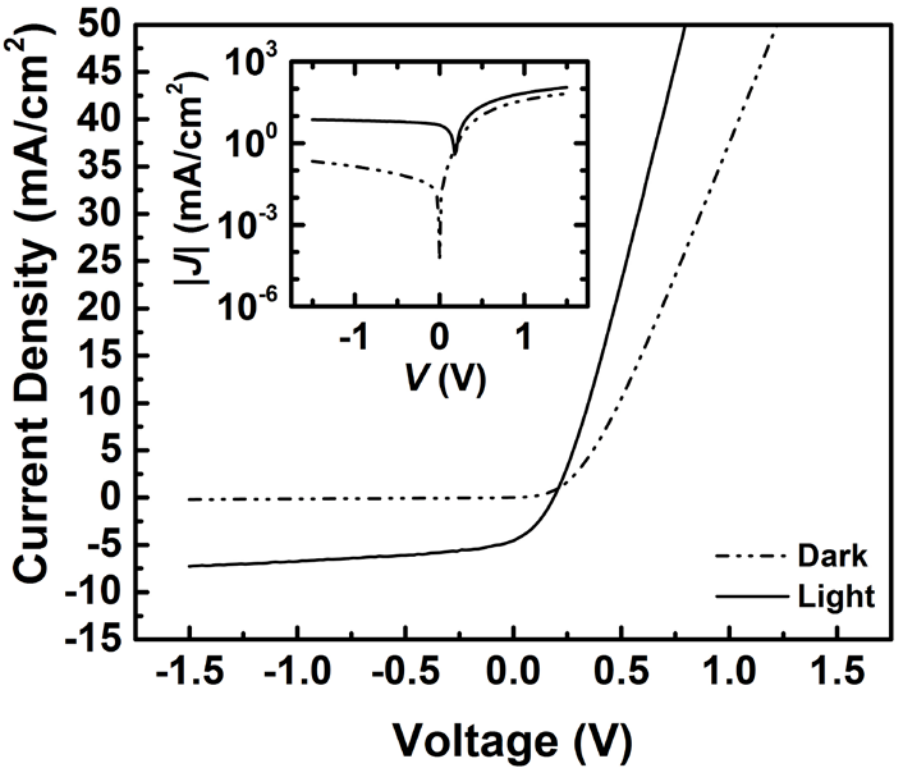

Figure 4.7. Representative *J–V* characteristics for OPV with structure glass / ITO / PEDOT:PSS / P3HT: ICBA (O_2-plasma treated) / Al. The inset shows the *J–V* characteristics on a semilogarithmic scale.

4.4.2.3.2 Effect on OPV Performance of Spin-coating 2-Methoxyethanol Solvent (Not Containing PEIE) on the Photoactive Layer

As a second control experiment, the solvent 2-methoxyethanol, not containing PEIE, was spin-coated on top of the O_2-plasma treated P3HT:ICBA photoactive layer, in the same structure: glass / ITO / PEDOT:PSS / P3HT:ICBA (O_2-Plasma treated + 2-Methoxyethanol) / Al. These OPV demonstrated values of V_{OC} = 428 ± 29 mV, J_{SC} = 6.3 ± 0.2 mA cm^{-2}, FF = 0.51 ± 0.02, and PCE = 1.4 ± 0.2 %, averaged over 10 OPV cells. *J−V* characteristics for a representative OPV cell are shown in Figure 4.8. All OPV parameters were worse than the case when the solvent containing PEIE was spin-coated

on P3HT:ICBA, confirming that PEIE played a critical role in the improvement of the OPV. There was a slight improvement in values of V_{OC} and FF, as compared to the reference OPV where Al electron collecting electrodes were directly deposited on P3HT:ICBA. A number of recent studies have demonstrated OPV improvements by means of a so-called solvent treatment, where a polar solvent is spin-coated on the photoactive layer prior to top metal electrode deposition [61-67]. These studies have postulated a number of reasons leading to improvements in OPV upon spin-coating the polar solvent on top of the photoactive layer, including the passivation of surface traps leading to reduced charge recombination, an increase in hole mobility leading to more balanced charge transport, and a more favorable morphology for charge extraction. Some of the studies specifically ruled out changes in the active layer morphology upon solvent treatment. Regardless, most significant solvent treatment effects are seen specifically in low bandgap polymer systems. The gains of the solvent treatment on its own in the case for P3HT:ICBA were minimal and necessitated the addition of PEIE in the solvent for substantial OPV performance improvements.

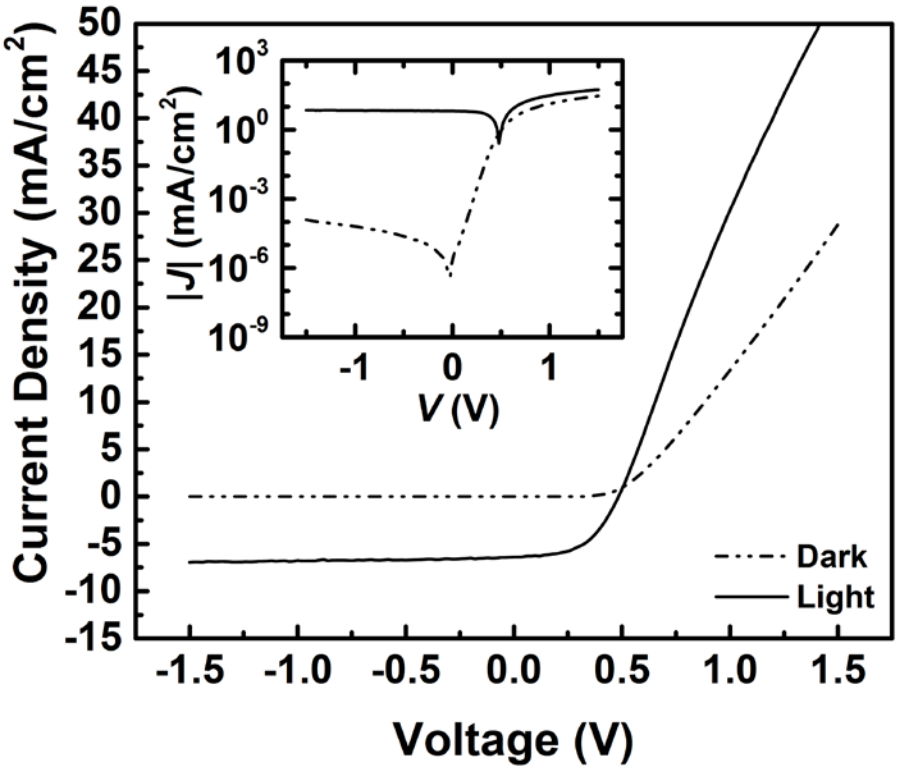

Figure 4.8. Representative *J–V* characteristics for OPV with structure glass / ITO / PEDOT:PSS / P3HT: ICBA (O_2-plasma and 2-methoxyethanol treated) / Al. The inset shows the *J–V* characteristics on a semilogarithmic scale.

4.4.2.4 Application of the Approach to OPV Containing Other Electron Acceptor Materials

Since PEIE was used to modify the electron-collecting interface in the OPV, it was instructive to demonstrate the effectiveness of the method for electron acceptor materials other than ICBA. Therefore, OPV were also fabricated by the same approach using the fullerene-derivatives $PC_{61}BM$ and $PC_{71}BM$. These fullerene derivatives have a larger electron affinity than ICBA [68].

Figures 4.9 (a) and 4.9 (b) show representative *J–V* characteristics for OPV with the structure glass / ITO / PEDOT:PSS / P3HT:$PC_{61}BM$ / Al and glass / ITO / PEDOT:PSS / P3HT:$PC_{61}BM$ / PEIE / Al, respectively.

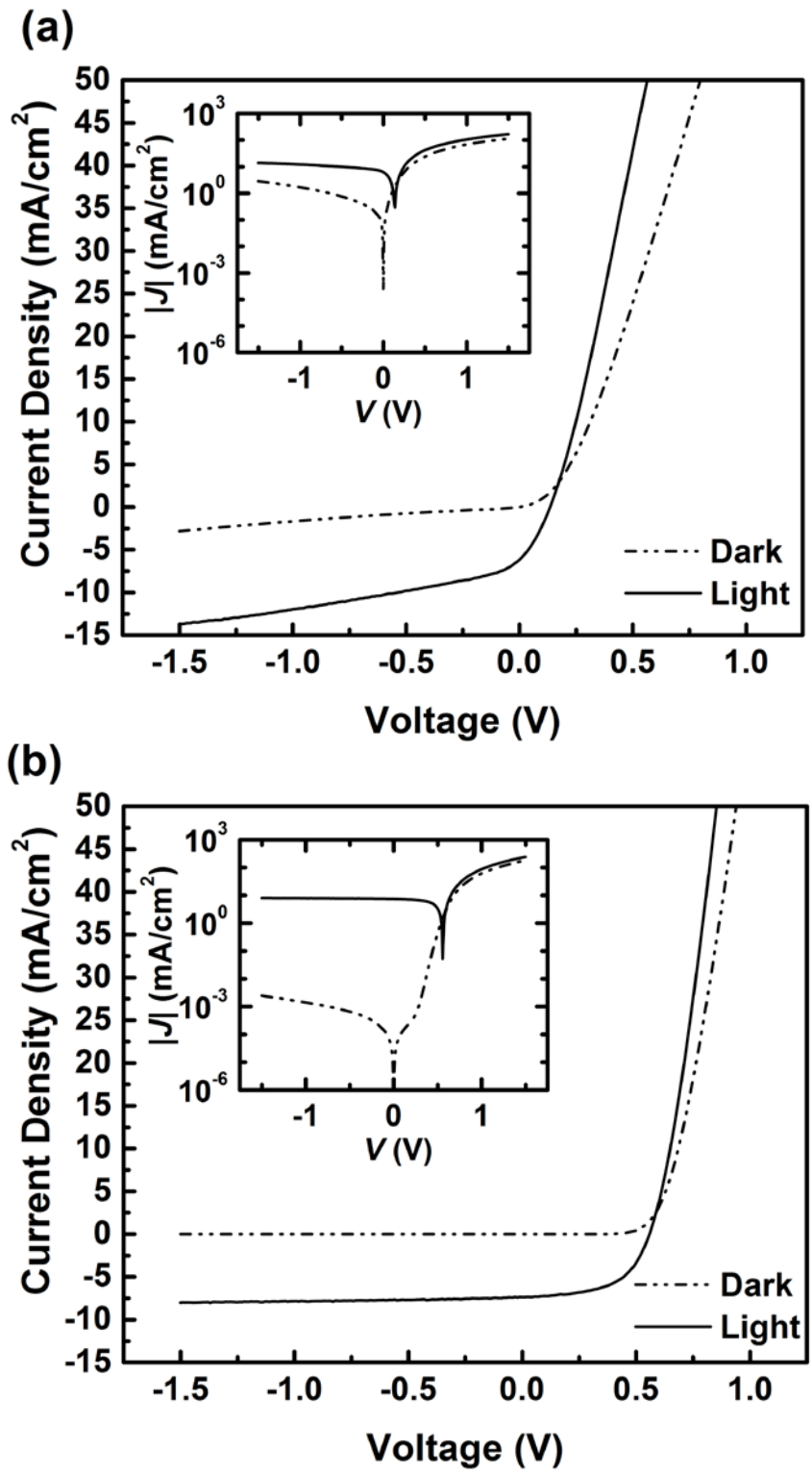

Figure 4.9. Representative *J*–*V* characteristics (a) for OPV with structure glass / ITO / PEDOT:PSS / P3HT:$PC_{61}BM$ / Al and (b) for OPV with structure glass / ITO / PEDOT:PSS / P3HT: $PC_{61}BM$ / PEIE / Al. The insets show the *J*–*V* characteristics on a semilogarithmic scale.

Figures 4.10 (a) and (b) respectively show representative *J*−*V* characteristics for OPV with the structure glass / ITO / PEDOT:PSS / P3HT:$PC_{71}BM$ / Al and glass / ITO / PEDOT:PSS / P3HT:$PC_{71}BM$ / PEIE / Al.

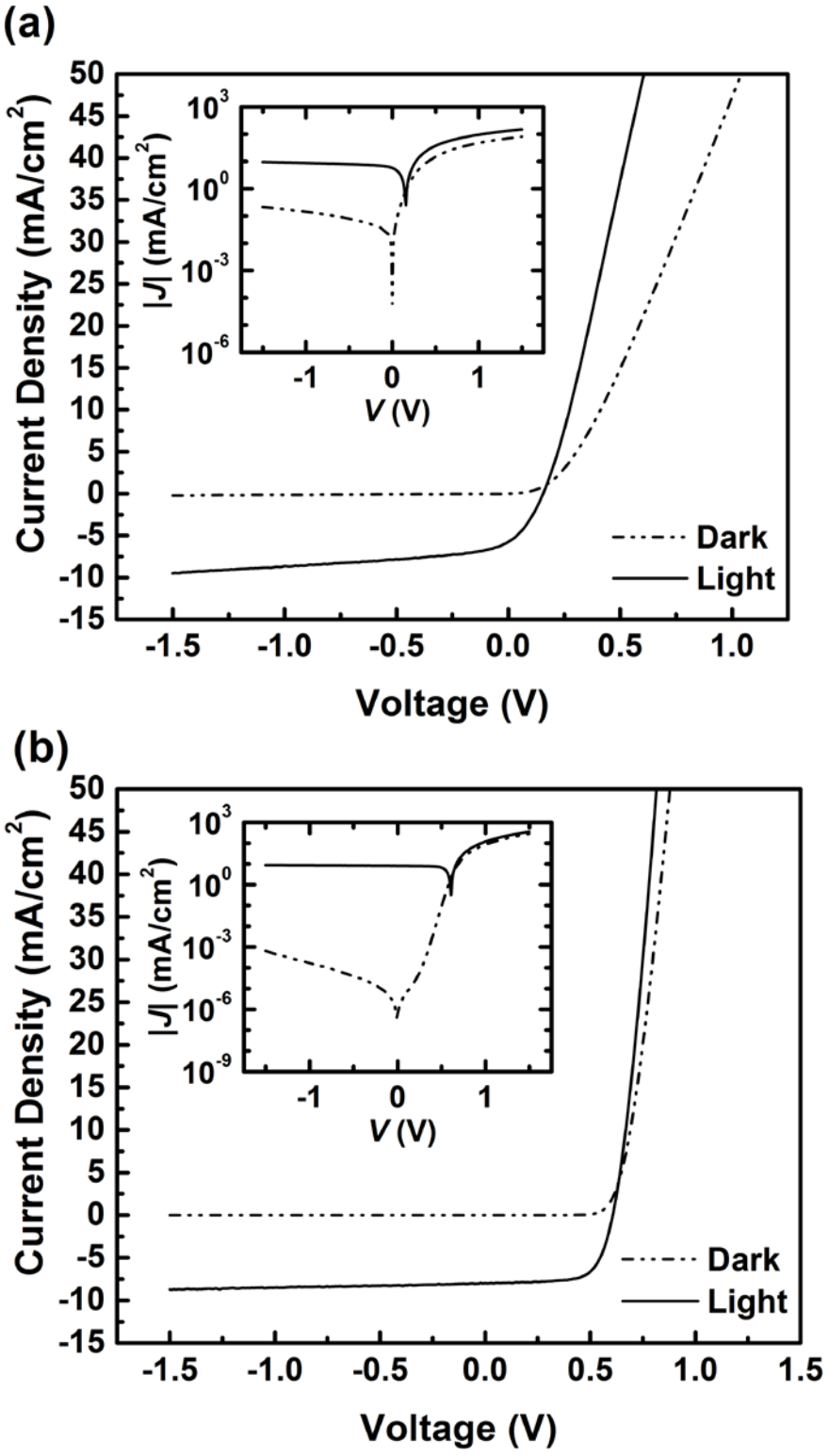

Figure 4.10. Representative *J–V* characteristics (a) for OPV with structure glass / ITO / PEDOT:PSS / P3HT:$PC_{71}BM$ / Al and (b) for OPV with structure glass / ITO / PEDOT:PSS / P3HT: $PC_{71}BM$ / PEIE / Al. The insets show the *J–V* characteristics on a semilogarithmic scale.

A substantial improvement in performance over OPV with the structure ITO/PEDOT:PSS/P3HT:($PC_{61}BM$ or $PC_{71}BM$)/Al was observed, both for OPV with $PC_{61}BM$ and $PC_{71}BM$ acceptors, after inserting PEIE prior to the Al metal deposition (Table 2), indicating broad applicability of the method. The dark current at -1.5 V was reduced from a value of $(-2.4 \pm 0.7) \times 10^{-3}$ A/cm^2 at -1.5 V to $(-2.8 \pm 4.5) \times 10^{-6}$ A/cm^2 over five OPV cells in the case of $PC_{61}BM$, again an improvement of three orders of magnitude. In the case of $PC_{71}BM$, the dark current at -1.5 V was reduced from a value of $(-1.6 \pm 0.4) \times 10^{-4}$ A/cm^2 at -1.5 V to $(-4.9 \pm 6.0) \times 10^{-6}$ A/cm^2 averaged over ten OPV cells, a decrease of two orders of magnitude.

4.4.3 Calcium-Free OPV with PEIE-Modified Silver Electron-Collecting Electrodes

In addition to using the electrode modifier PEIE with Al, it was also applied in conjunction with Ag top electrodes. Ag is more stable in air than Al, which readily forms an oxide. Ag also possesses a higher reflectance than Al above 400 nm, which should further enhance the second-pass current contribution. Figure 4.11 shows representative *J*−*V* curves for (a) OPV with the structure glass / ITO / PEDOT:PSS / P3HT:ICBA / Ag and (b) glass / ITO / PEDOT:PSS / P3HT:ICBA / PEIE / Ag. In this case again, there was a substantial enhancement in the value of V_{OC} (446 ± 27 mV to 762 ± 5 mV) as well as the *FF* (0.38 ± 0.01 to 0.63 ± 0.01) after PEIE incorporation (Table 2). Indeed, the greater reflectance of Ag manifested in higher J_{SC} (9.4 ± 0.2 mA cm^{-2}) as compared to the case where aluminum electrodes were used.

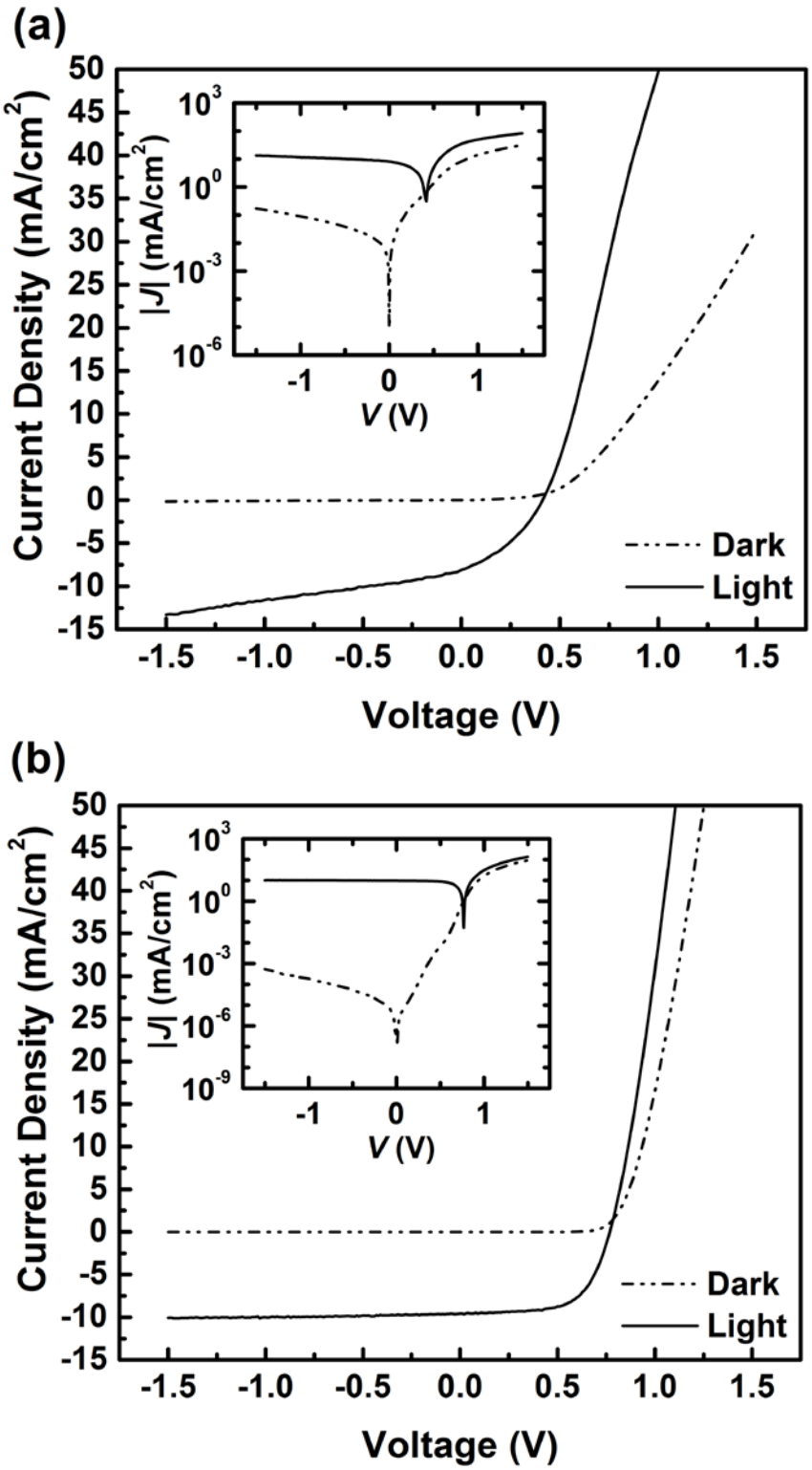

Figure 4.11. Representative *J–V* characteristics (a) for OPV with structure glass / ITO / PEDOT:PSS / P3HT:ICBA / Ag and (b) for OPV with structure glass / ITO / PEDOT:PSS / P3HT:ICBA / PEIE / Ag. The insets show the *J–V* characteristics on a semilogarithmic scale.

As was in the case for PEIE-modified Al top electron-collecting electrodes, a reduction in dark current was also seen in PEIE-modified Ag top electron-collecting electrodes. For OPV with the direct deposition of Ag on P3HT:ICBA, the dark current was $(1.9 \pm 1.6) \times 10^{-4}$ A/cm^2, averaged over 10 OPV cells. For glass / ITO / PEDOT:PSS / P3HT:ICBA / PEIE / Ag OPV, the dark current was $(3.7 \pm 6.8) \times 10^{-6}$ A/cm^2, averaged over four OPV cells.

4.4.4 Calcium-Free OPV with PEIE-Modified Gold Electron-Collecting Electrodes

To demonstrate the versatility of the method, experiments were also repeated using Au electrodes to show that OPV could be fabricated with high-work-function metals acting as the top metal electron-collecting electrode. Representative *J*–*V* characteristics of OPV with structure glass / ITO / PEDOT:PSS / P3HT:ICBA / Au and glass / ITO / PEDOT:PSS / P3HT:ICBA / PEIE / Au are shown in Figure 4.12. Enhancements were seen in V_{OC}, J_{SC}, and FF for the case of glass / ITO / PEDOT:PSS / P3HT:ICBA / PEIE / Au as shown in Table 4.1.

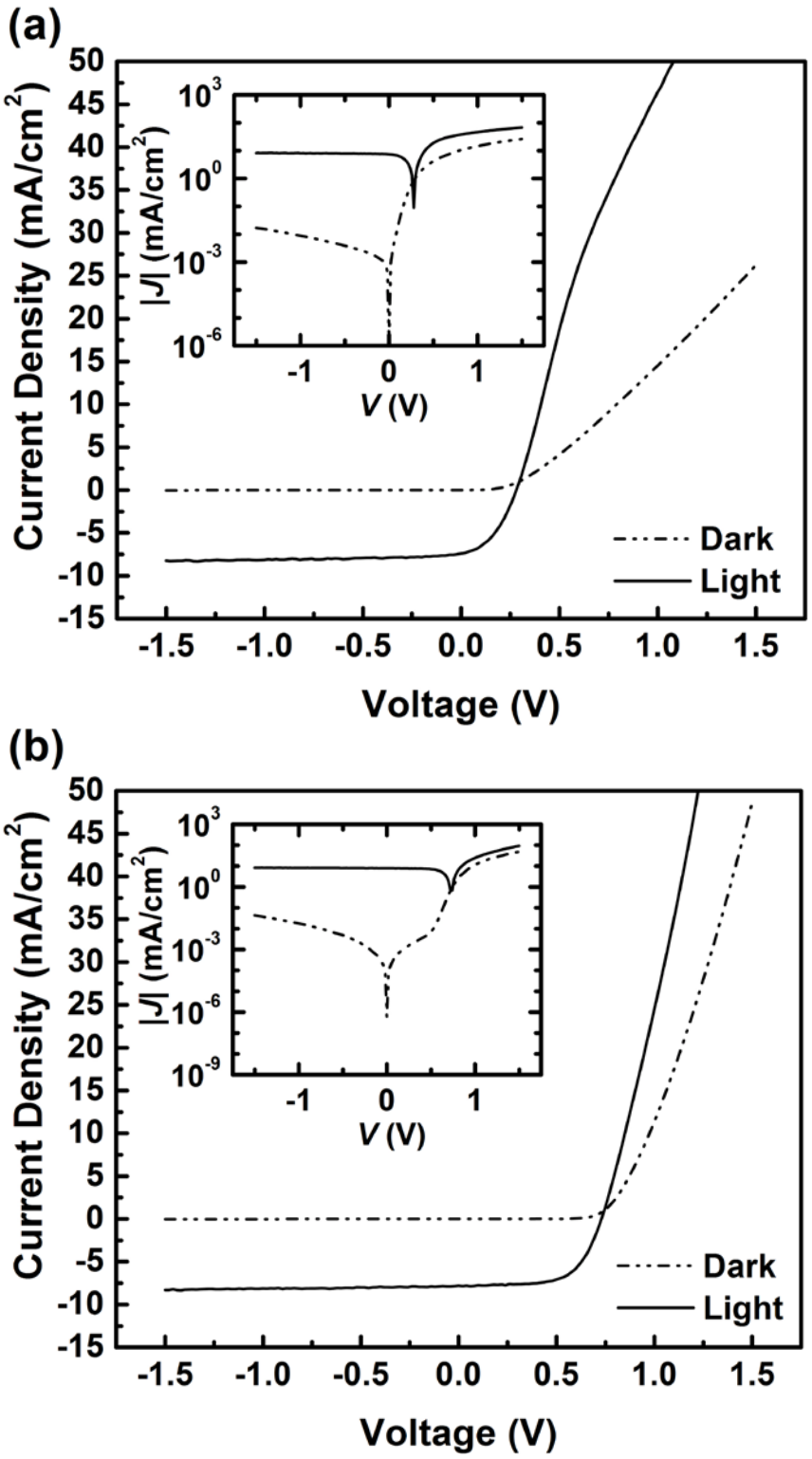

Figure 4.12. Representative *J–V* characteristics (a) for OPV with structure glass / ITO / PEDOT:PSS / P3HT:ICBA / Au and (b) for OPV with structure glass / ITO / PEDOT:PSS / P3HT:ICBA / PEIE / Au. The insets show the *J–V* characteristics on a semilogarithmic scale.

(Reprinted with permission from Talha M. Khan et al. *ACS Applied Materials & Interfaces* **2014** *6* (9), 6202-6207. Copyright (2014) American Chemical Society)

4.4.5 OPV with PEIE-Modified Calcium Electron-Collecting Electrodes

Although the objective of the study was to use PEIE to facilitate electron collection in air-stable metal electrodes, the impact of PEIE modification in conjunction with Ca electrodes was also studied. Representative *J*−*V* curves for OPV in the structure glass / ITO / PEDOT:PSS / P3HT:ICBA / PEIE / Ca / Al are shown in Figure 4.13. These OPV yielded values of V_{OC} = 828 ± 4 mV, J_{SC} = 8.3 ± 0.3 mA cm^{-2}, FF = 0.73 ± 0.01, and PCE = 5.0 ± 0.2 %, averaged over 14 OPV cells, which is an improvement over the reference OPV in the same structure without PEIE.

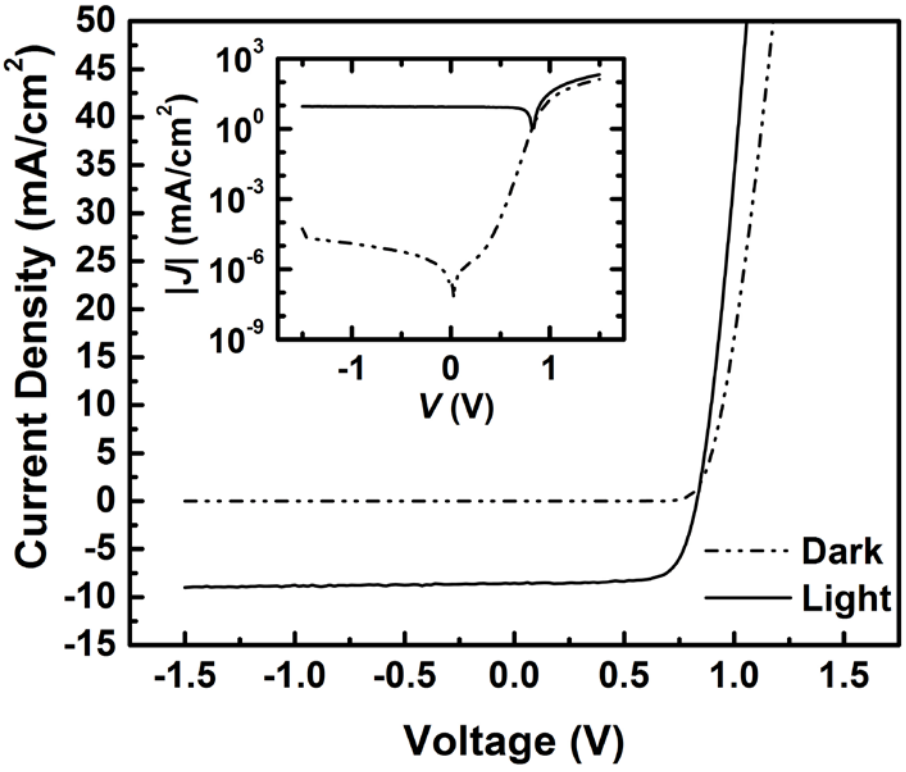

Figure 4.13. Representative *J–V* characteristics for OPV with structure glass / ITO / PEDOT:PSS / P3HT:ICBA / PEIE / Ca. The inset shows the *J–V* characteristics on a semilogarithmic scale.

Table 4.1 presents a summary of the performance statistics under simulated 1 sun illumination for all novel OPV structures tested as part of the study.

Table 4.1. OPV Performance Statistics under Simulated 100 mW cm^{-2} AM 1.5 G Illumination for P3HT:Acceptor/Electron-Collecting Electrode Bulk Heterojunction OPV with a 200 nm Thick Photoactive Layer

Acceptor/electrode (no. of OPV cells data is averaged over)	V_{OC} **(mV)**	J_{SC} **(mA cm^{-2})**	**FF**	**PCE (%)**	J_{Dark} **at -1.5 V (A cm^{-2})**
ICBA / O_2-Plasma / Al (5)	191 ± 14	4.5 ± 0.2	0.35 ± 0.01	0.3 ± 0.1	$(-3.0 \pm 1.1) \times 10^{-4}$
ICBA / Al (10)	246 ± 14	7.5 ± 0.3	0.41 ± 0.01	0.8 ± 0.1	$(-7.0 \pm 1.5) \times 10^{-5}$
ICBA / (solvent) / Al (10)	428 ± 29	6.3 ± 0.2	0.51 ± 0.02	1.4 ± 0.2	$(-6.3 \pm 18) \times 10^{-6}$
ICBA / PEIE / Al (5)	775 ± 6	9.1 ± 0.5	0.65 ± 0.01	4.6 ± 0.3	$(-8.2 \pm 5.6) \times 10^{-8}$
$PC_{61}BM$ / Al (5)	105 ± 18	5.4 ± 0.5	0.29 ± 0.01	0.2 ± 0.1	$(-2.4 \pm 0.7) \times 10^{-3}$
$PC_{61}BM$ / PEIE / Al (5)	551 ± 5	7.3 ± 0.1	0.56 ± 0.01	2.2 ± 0.1	$(-2.8 \pm 4.5) \times 10^{-6}$
$PC_{71}BM$ / Al (4)	200 ± 34	5.8 ± 0.1	0.34 ± 0.01	0.4 ± 0.1	$(-1.6 \pm 0.4) \times 10^{-4}$
$PC_{71}BM$ / PEIE / Al (10)	607 ± 3	7.9 ± 0.2	0.68 ± 0.01	3.3 ± 0.1	$(-4.9 \pm 6.0) \times 10^{-6}$
ICBA / Ag (10)	446 ± 27	7.9 ± 0.2	0.38 ± 0.01	1.4 ± 0.1	$(-1.9 \pm 1.6) \times 10^{-4}$
ICBA / PEIE / Ag (4)	762 ± 5	9.4 ± 0.2	0.63 ± 0.01	4.5 ± 0.2	$(-3.7 \pm 6.8) \times 10^{-6}$
ICBA / Au (8)	277 ± 5	7.1 ± 0.3	0.42 ± 0.01	0.8 ± 0.1	$(-2.0 \pm 1.9) \times 10^{-5}$
ICBA / PEIE / Au (9)	733 ± 8	7.5 ± 0.3	0.64 ± 0.01	3.5 ± 0.1	$(-1.7 \pm 2.4) \times 10^{-5}$
ICBA / Ca / Al (5)	822 ± 4	8.0 ± 0.1	0.71 ± 0.01	4.6 ± 0.1	$(-6.6 \pm 3.1) \times 10^{-8}$
ICBA / PEIE / Ca / Al (4)	831 ± 1	8.4 ± 0.2	0.73 ± 0.01	5.1 ± 0.1	$(-5.5 \pm 0.7) \times 10^{-8}$

4.5 Discussion

PEIE reduces the work function of conductors on which it is coated due to the formation of a surface dipole [58]. Similarly, the improvement in performance for OPV with structure glass / ITO / PEDOT:PSS / P3HT:(ICBA or $PC_{61}BM$ or $PC_{71}BM$) / PEIE / (Al or Ag or Au) as compared to OPV without PEIE with structures ITO / PEDOT:PSS / P3HT:(ICBA or $PC_{61}BM$ or $PC_{71}BM$) / (Al or Ag or Au), to the formation of surface dipoles that arise because of a partial electron transfer from the amine groups of PEIE to the respective metals deposited on them. The surface dipoles, with a slight negative charge toward the metals and the corresponding positive charge toward the active layer, result in the lowering of the vacuum level of the metals. The vacuum level shift is the source of the metal work function reduction, allowing the formation of a low-work-function contact between ICBA and the respective metals. The results of a recent report [69] also allow us to infer that such a work function reduction could lead to improved OPV performance by means of decreased surface recombination of holes in P3HT at the PEIE/metal interface, as a result of increased band bending. This hypothesis could be appropriate since studies [68] have shown that P3HT preferentially segregates toward the top of the P3HT:ICBA film, which is the surface where PEIE was deposited in the experiments described here.

The photoactive layer morphology of bulk heterojunction OPV generally depends on a number of factors, including the solvent from which the film is spin-coated, the underlying substrate including any surface treatments, spin coating speed and other parameters, and film drying time. These parameters were kept uniform across all OPV studied. The only difference introduced in the test OPV was a very brief flash of oxygen

plasma and the spin-coating of PEIE from 2-methoxyethanol solvent, followed by the typical thermal annealing conducted on P3HT-based films. Significant changes to active layer morphology resulting from the momentary plasma exposure are not expected. On the basis of the insolubility of P3HT and ICBA in 2-methoxyethanol, again no change in photoactive layer morphology is expected. The only difference that could rise may result from the thermal annealing process of P3HT:ICBA with and without the presence of PEIE on top. It is possible that the anneal step might cause some degree of migration of PEIE into the photoactive layer.

4.6 Impact

The results are particularly significant for the electron acceptor material, ICBA, which does not form an Ohmic contact with Al, as evidenced by the low fill factor in OPV where Al was directly deposited on the photoactive layer, regardless of the annealing sequence with respect to metal deposition, thereby necessitating the presence of a low-work-function metal such as Ca. These developments reduce the reliance on Ca for efficient OPV and open up the possibilities of novel structures including conventional geometry tandem OPV and modules [70]. The results show that the method, by which the work function of air-stable electrodes is significantly reduced by amine-containing polymers such as PEIE, is independent of the order of deposition of the surface modifier and the conductor.

The preliminary research, published in [59] has garnered 15 citations in the scientific literature at the time of writing of this thesis. In addition to being cited as part of review papers, it has also led to the development of novel perovskite-type PV. In [71],

the authors employed the approach of coating PEIE above an organic semiconductor layer in the perovskite solar cell architecture. For the structure glass / ITO / PEDOT:PSS / $CH_3NH_3PBI_{3-X}Cl_X$ / PCBM / Ag, the authors reported PCE of 8.53%, whereas, in the structure glass / ITO / PEDOT:PSS / $CH_3NH_3PBI_{3-X}Cl_X$ / PCBM / PEIE / Ag, the authors reported an enhanced PCE of 12.01%.

CHAPTER 5

DESIGN RULES FOR THE DEVELOPMENT OF ORGANIC PHOTODETECTORS INSPIRED BY ORGANIC PHOTOVOLTAICS

This chapter of the dissertation describes design rules, inspired by the study of organic photovoltaic cells, for the fabrication of high specific detectivity (> 10^{14} Jones) organic semiconductor-based photodetectors. Photodetectors are similar to photovoltaic cells in that they both convert an input optical signal into an output electrical signal. The main difference between the devices is that photovoltaic cells are optimized to maximize the output photogenerated electrical power, while in photodetectors, the ability to detect low levels of light illumination is particularly critical.

5.1 Relevant Metrics for Photodetectors

An important metric for photodetectors is the responsivity, *R*, the ratio of the photogenerated current or voltage to the incident optical power (units: A/W or V/W). The photogenerated current (voltage) is the difference between the current (voltage) under illumination and the current (voltage) measured in the dark. *R* is proportional to the device external quantum efficiency, and is a function of wavelength, dropping off as the semiconductor absorption decreases at longer wavelength.

The noise current is another important photodetector metric. For semiconductor photodetectors studied in this work, the current measured in the dark, J_{Dark}, at the applied reverse bias of operation (when operated in the so-called photoconductive mode) is

considered to be the noise current. The dark current under reverse bias is a measure of the sensitivity of the device to illumination, placing a floor on the detection limit, since the detection of photons is manifested in an increase in current as shown in Figure 5.1 (left panel). If the device has a high dark leakage current (Figure 5.1, right panel), the contribution of absorbed photons at low illumination levels may remain masked in the dark current, thereby resulting in the photons going undetected.

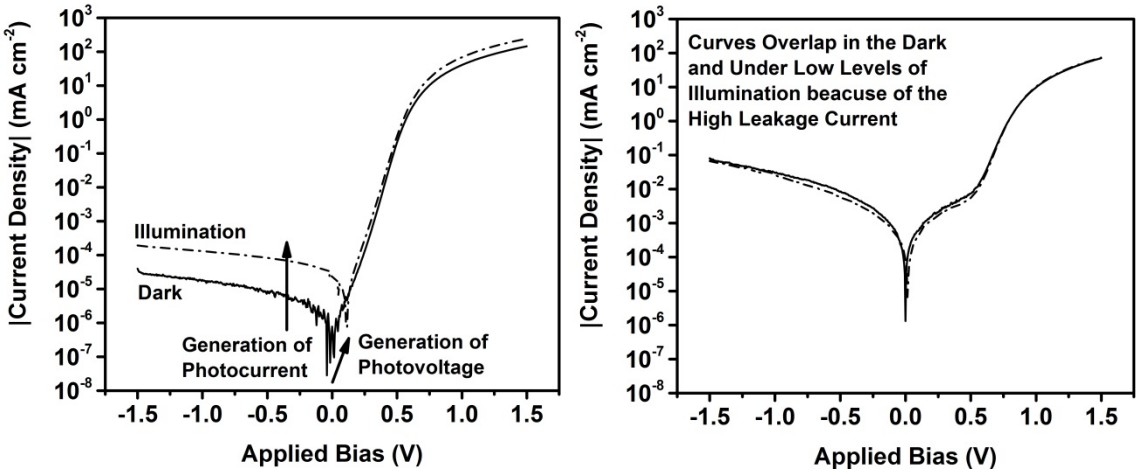

Figure 5.1. *J–V* curves in semilogarithmic scale showing the response to low level of incident light for a device with (left) low dark current, and (right) high dark current.

The noise equivalent power, NEP, is the ratio of the output noise to the responsivity and provides a measure of the smallest detectable input. The smaller the NEP, the more sensitive the photodetector is.

The detectivity, *D*, is the inverse of the NEP, thereby providing a metric that increases with better detector performance, as opposed to the NEP. A related metric is the specific detectivity, *D** (units: cm $Hz^{1/2}$ W^{-1} or Jones), in which the detectivity is

normalized by the product of the detector area and observation bandwidth. If the dark current is considered to be the dominant source of noise, the specific detectivity can be expressed as [72]:

$$D^* = \frac{R}{\sqrt{2qJ_{\text{Dark}}}} \tag{5.1}$$

where D^* is the specific detectivity, R is the responsivity, q is the elementary charge, and J_{Dark} is the current density in the dark.

The linear dynamic range is a measure of the linearity of the photogenerated current with increasing incident optical power, and is expressed in dB.

The frequency response is the response of the photodetector when the input optical signal is modulated in frequency. The frequency at which the output power is halved is the 3 dB cut off frequency.

The range of operation in wavelength describes which part of the electromagnetic spectrum the photodetectors can operate in. For semiconductor photodetectors, this depends upon the absorption spectrum / bandgap of the semiconductor material.

5.2 Dark Current in Organic Semiconductor Diodes

The current generated by a photodiode in the dark provides meaningful information about thermal generation, recombination, and injection of carriers inside the device. As described in sections 2.4.2 and 2.4.4 in Chapter 2, the current measured in the dark under reverse bias has contributions from two sources: the inherent reverse

saturation current, J_0, of the diode resulting from the thermal generation of carriers and a parasitic shunt resistance-limited leakage current.

The dark current under reverse bias in organic solar cells, where photoactive layers are typically 100 - 200 nm thick, is often dominated by leakage current through shunt paths between the electrodes of the device rather than the intrinsic reverse saturation current of the diode. Researchers frequently misidentify the dark current measured under reverse bias as J_0 and present misguided conclusions based on this, such as attempting to link increases in V_{OC} to the dark leakage current (rather than J_0) [69].

5.3 Conventional Approach of Designing Organic Photodetectors: The Use of Charge Blocking Layers

The conventional approach of designing organic photodetectors emphasizes the role of so-called charge blocking layers at the electrodes that reduce the dark current under reverse bias [72, 73]. The blocking layers employed are typically wide bandgap materials so as to minimize the absorption of incident photons, which should be absorbed in the donor - acceptor photoactive layer. In addition to the added complexity introduced to the device structure, the other disadvantage of employing charge blocking layers is that they do not reduce the inherent reverse saturation current of the diode, J_0, which is related to interactions between the donor and acceptor materials that make up the photoactive layer.

5.4 Novel Approach Implemented to Reduce the Dark Current

A two-pronged approach was implemented as part of this work to design high specific detectivity ($D^* > 10^{14}$ Jones) photodetectors. The first part of the approach involved the reduction of the reverse saturation current by optimizing the donor-acceptor pair in the photoactive layer to have a large intermolecular charge-transfer state energy. The second part of the approach involved the optimization of device processing so as to increase the shunt resistance and decrease the parasitic leakage current.

5.4.1 Materials Systems with Large Charge-Transfer State Energy

In organic semiconductor systems consisting of a donor and acceptor material, intermolecular interactions at the donor-acceptor interface result in the formation of a so called charge-transfer state, as illustrated on the molecular scale in Figure 5.2.

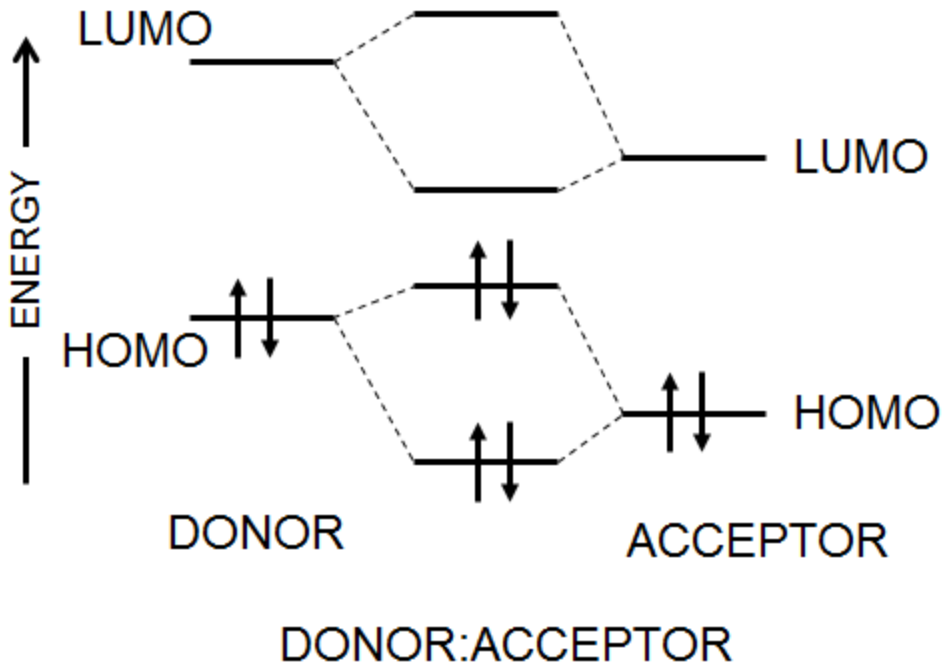

Figure 5.2. Illustration of the molecular interaction at the donor-acceptor interface that leads to the formation of a charge-transfer state.

In the case of organic solids, the discrete levels are replaced by bands. The charge transfer state can be probed experimentally in donor:acceptor blends by sub-band gap absorption [74]. In OPV, the role of the charge-transfer state has been gaining much attention, as it has been correlated with the cell V_{OC} [75].

An additional consequence of the charge-transfer state being the effective energy gap of the system is that it is also relevant for the thermal generation of carriers, and therefore the reverse saturation current. This important observation is often ignored in the context of photodetectors. More energy is required for the thermal generation of charge carriers contributing to current when the charge-transfer state energy (or effective band gap) is larger and the reverse saturation current is therefore smaller. In this work, high specific detectivity photodetectors were fabricated based on the combination of the donor

P3HT and the acceptor ICBA. The combination of P3HT and ICBA in OPV gives rise to a high V_{OC} at one sun at room temperature (V_{OC} > 830 mV) [60] compared to many other materials systems as a result of the large charge-transfer state energy in this system as shown ahead.

Since the reverse saturation current is often dominated by the leakage current, a secondary approach was also employed in conjunction with the reduction of the reverse saturation current to obtain high specific detectivity photodetectors with very low dark current. The complementary approach is the reduction of the parasitic shunt resistance-limited leakage current in devices.

5.4.2 Decreasing the Parasitic Shunt Resistance-Limited Leakage Current

The parasitic shunt resistance-limited leakage current in an organic semiconductor diode results from shunt paths between the hole and electron-collecting electrodes of the device. Imperfections, such as pinholes in the photoactive layer that form during the film coating process, are an example of a shunt path. In the fabrication of organic semiconductor devices, functional layers (with thickness on the order of tens to hundreds of nm) are typically deposited one atop another by methods such as spin-coating. Therefore, a defect in the film formation of one functional layer can affect the formation of subsequent films.

One approach to minimize defects that contribute to such shunt paths has been through the deposition of films via film transfer lamination rather than spin-coating [76]. In film transfer lamination, films are not spin-coated atop one another sequentially, but rather are transferred on to the target substrate having been spin-coated on a separate

substrate. This approach led to a reduction in the parasitic shunt resistance-limited leakage current due to the misalignment of defects that would otherwise vertically propagate. The disadvantage of film transfer lamination is that the delamination from the initial substrate and then the subsequent lamination on the target substrate has potential to damage the films.

In this work, the shunt resistance-limited leakage current between the hole and electron-collecting electrodes was minimized by increasing thickness of the photoactive layer. Larger photoactive layer film thickness reduces the likelihood of the presence of pinholes or other defects that propagate between the electrodes. In spin-coating, increasing the layer thickness is trivial and can be accomplished by increasing the concentration of the donor and acceptor components within the solvent used to spin-coat from. In optimized OPV, the typical film thickness is around 100 - 200 nm, and larger film thicknesses tend to degrade OPV device performance due to increased series resistance stemming from the low conductivity of the photoactive layer. For the detectors developed in this work, the photoactive layer film thickness was varied between 500 - 1000 nm. While the larger film thickness might have an adverse effect on the responsivity, the orders of magnitude decrease in the reverse bias leakage current compensates for it, leading to high specific detectivity in the photodetectors.

In addition to increasing the photoactive layer film thickness, the post spin-coating film drying process was optimized to enhance the film crystallinity. By spin-coating the P3HT:ICBA photoactive layer from 1,2-dichlorobenzene, a solvent with a boiling point of 180.5 °C, the resulting cast films were wet and allowed to slowly dry within the atmosphere of the solvent [77] in a so-called solvent annealing step. Studies

have shown that the slow drying of the P3HT-based film results in a high crystallinity, which enhances the photodetector responsivity.

Lastly, the P3HT:ICBA photoactive layer was sandwiched between electron and hole collecting electrodes with a large work function contrast. ITO modified by PEIE has been shown to yield a surface with a low average work function of 3.60 eV (as measured by Kelvin probe in air) [58]. Freshly-evaporated MoO_3 in vacuum has a high work function of 6.9 eV (as measured by UPS in vacuum) [78]. The use of these electrode materials obviates the need for so-called charge-blocking layers.

The device structure of the high specfic detectivity photodetectors is shown in Figure 5.3:

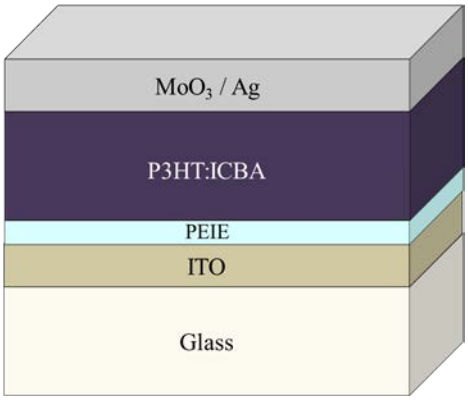

Figure 5.3 Structure of the high specific detectivity organic photodetector.

5.5 Results and Discussion

5.5.1 Electrical and Optical Characterization

A representative *J-V* characteristic taken in the dark for a photodetector with device structure glass / ITO / PEIE / P3HT:ICBA / MoO_3 / Ag is shown in Figure 5.4.

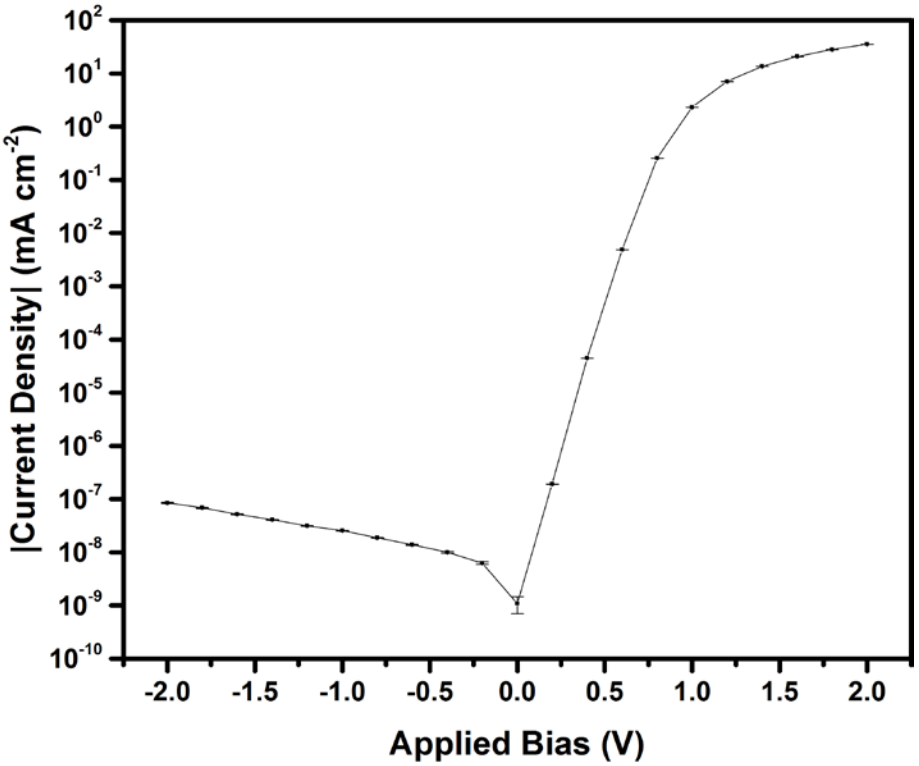

Figure 5.4 *J–V* characteristic in the dark in semilogarithmic scale, for the glass / ITO / PEIE / P3HT:ICBA / MoO_3 / Ag photodetector.

Most notable from the *J-V* characteristic is the low current density under reverse bias. At an applied bias of 0 *V*, the average current density in the dark was (1.1 ± 0.4) pA/cm^2. As a result, the devices were very sensitive to low levels of optical power. The photocurrent generated by the device in response to varying power output of a 532 nm neodymium yttrium vanadate laser is shown in Figure 5.5.

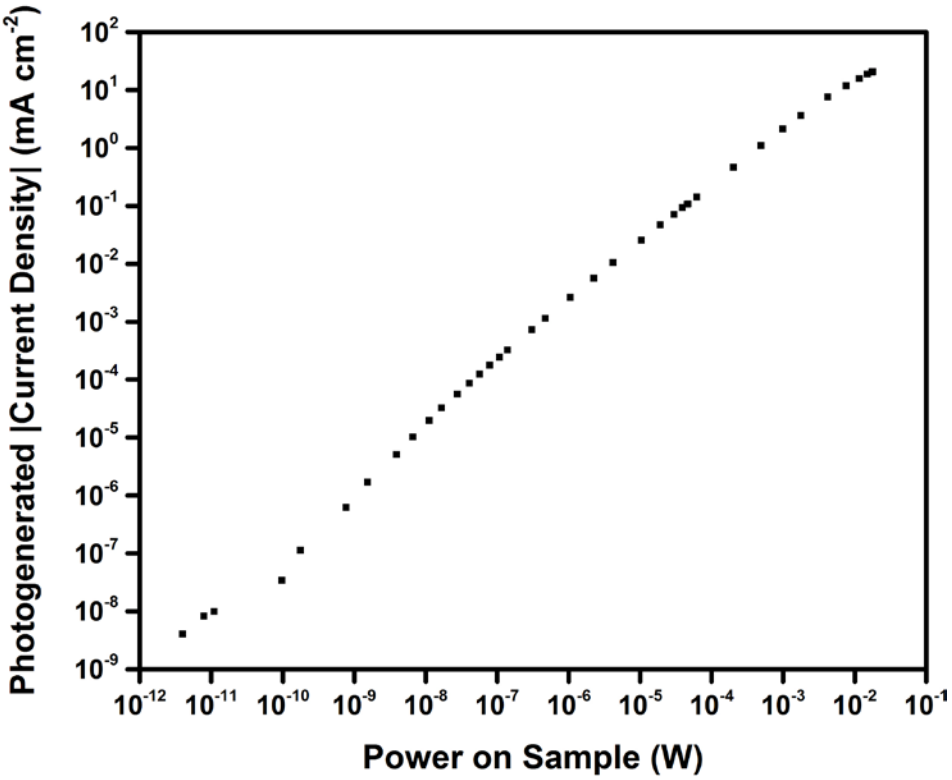

Figure 5.5. Photogenerated current density in response to varying incident optical power from a 532 nm laser in a log-log scale for the glass / ITO / PEIE / P3HT:ICBA / MoO_3 / Ag photodetector.

The photodetectors were able to generate a detectable photo-response across 9 orders of magnitude of decreasing optical power.

In order to characterize the spectral response of the photodetector, the laser was replaced by a broadband light source coupled with a monochromator and the photo-generated current was measured across the visible spectrum into the near infrared. By normalizing the measured photogenerated current from the photodetector by the incident optical power, as measured by a power meter, the spectral responsivity for the photodetector at an applied bias of 0 V was obtained and is shown below in Figure 5.6.

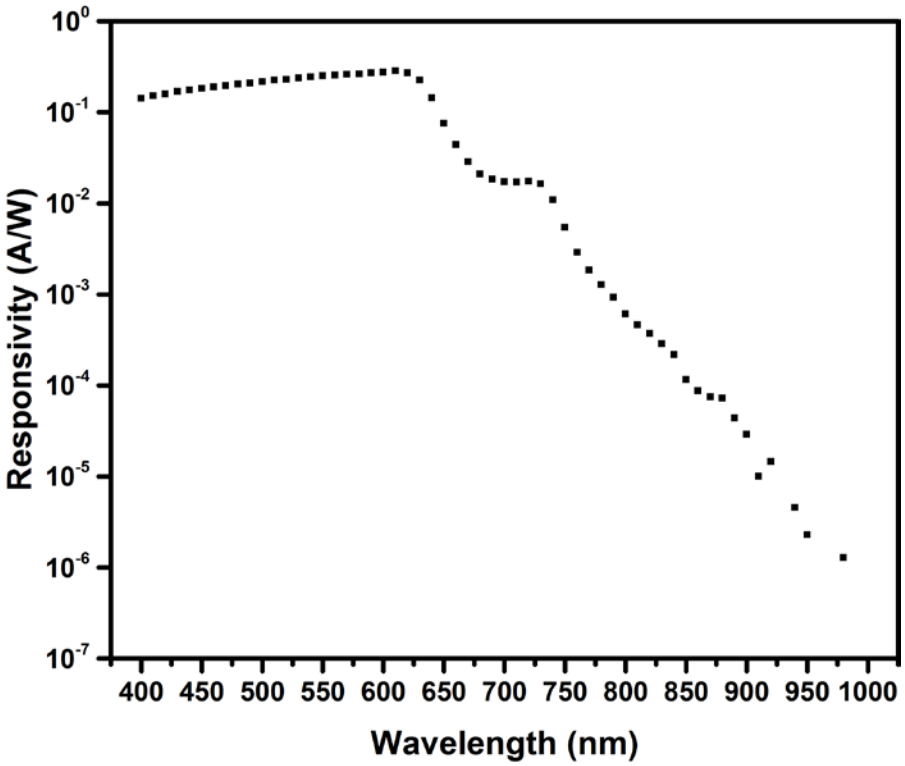

Figure 5.6. Responsivity at an applied bias of 0 V for the glass / ITO / PEIE / P3HT:ICBA / MoO_3 / Ag photodetector.

The responsivity monotonically increased beyond 400 nm, reaching the peak of 0.28 A/W at a wavelength of 610 nm, after which it begins to drop following the absorption tail of P3HT.

Finally, the specific detectivity at an applied bias of 0 *V* is shown in Figure 5.7.

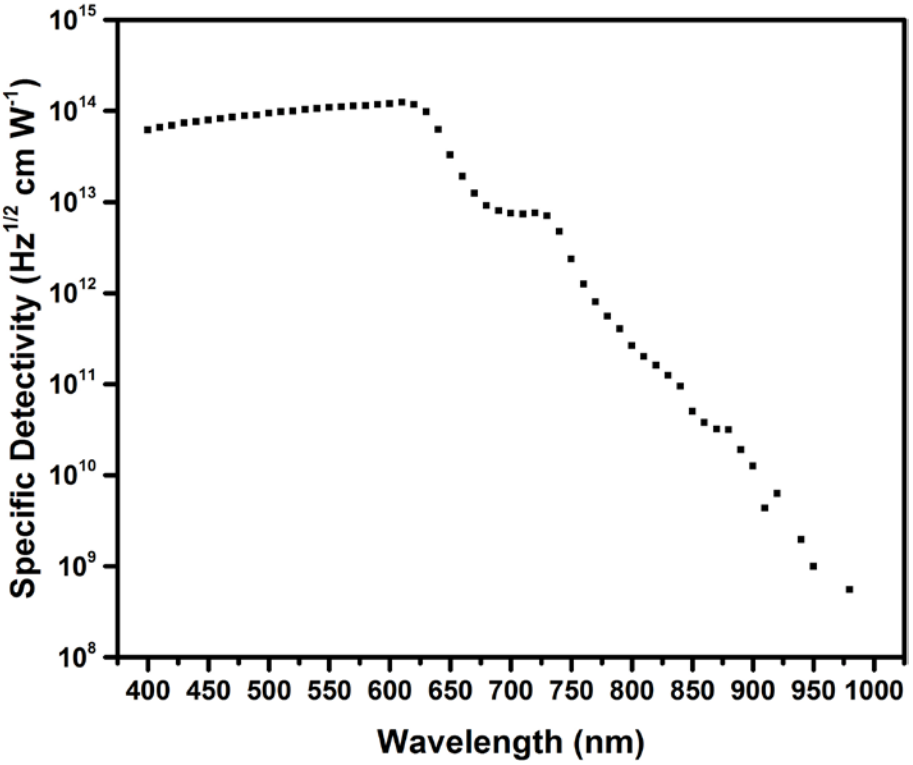

Figure 5.7. Specific detectivity at an applied bias of 0 V for the glass / ITO / PEIE / P3HT:ICBA / MoO_3 / Ag photodetector.

The peak specific detectivity of 1.25×10^{14} Jones is two orders of magnitude higher than that obtained with silicon photodetectors [72]. In addition, this high specific detectivity was obtained in room temperature samples and did not require active cooling.

5.5.2 Linking the Energy of the Charge-Transfer State to the Reverse Saturation Current

As mentioned in section 5.4.1, the energy of the charge transfer state is the effective gap that is relevant for the thermal generation of carriers that contribute to the

reverse saturation current. This section presents the experimental approach that was taken to provide evidence for this.

Previous work [79] has shown that the thermal generation of carriers is a thermally activated process and J_0 follows an Arrhenius relationship given by:

$$J_0 = J_{00} \exp\left(-\frac{\phi_B}{kT}\right) \tag{5.2}$$

where J_0 is the reverse saturation current density, J_{00} is a pre-factor, k is Boltzmann's Constant, T is the absolute temperature, and ϕ_B is the activation energy. Measuring J_0 over a range of different temperature values allows for the extraction of the ϕ_B activation energy.

5.5.3 Extraction of J_0 from Variable Irradiance J-V Measurements

The approach to extract J_0 is now described. From section 2.4, recall that:

$$J = J_0\left[\exp\left(\frac{V - JR_S A}{\frac{nkT}{e}}\right) - 1\right] + \frac{V - JR_S A}{R_P A} - J_{ph} \tag{5.3}$$

By rearrangement, the equation can be expressed as:

$$V = \frac{nkT}{e}\ln\left(\frac{J}{J_0} + \frac{J_{ph}}{J_0} - \left(\frac{V - JR_S A}{J_0 R_P A}\right) + 1\right) + JR_S A \tag{5.4}$$

At the open-circuit voltage, $V = V_{OC}$, and the current density across the terminals, J, is zero ($J = 0$):

$$V_{OC} = \frac{nkT}{e} \ln\left\{1 + \frac{J_{ph}}{J_0}\left(1 - \frac{V_{OC}}{J_{ph} R_P A}\right)\right\} \tag{5.5}$$

Since the photodetectors have large shunt resistance values, the following simplification can be applied:

$$\frac{V_{\mathrm{OC}}}{J_{\mathrm{ph}} R_{\mathrm{P}} A} << 1 \tag{5.6}$$

In this case,

$$V_{OC} \approx \frac{nkT}{e} \ln\left\{1 + \frac{J_{ph}}{J_0}\right\} \tag{5.7}$$

For typical devices, the photogenerated current can be approximated by the short circuit current, yielding:

$$V_{OC} \approx \frac{nkT}{e} \ln\left\{1 + \frac{J_{SC}}{J_0}\right\} \tag{5.8}$$

Since the reverse saturation current of a device due to thermal generation of carriers is usually much smaller than the short-circuit current:

$$\frac{J_{\mathrm{SC}}}{J_0} >> 1 \tag{5.9}$$

$$V_{\mathrm{OC}} \approx \frac{nkT}{q} \ln\left\{\frac{J_{\mathrm{SC}}}{J_0}\right\} \tag{5.10}$$

$$V_{OC} \approx \frac{nkT}{q}\left(\ln J_{SC} - \ln J_0\right) \tag{5.11}$$

$$V_{OC} \approx \frac{nkT}{q}\ln J_{SC} - \frac{nkT}{q}\ln J_0 \tag{5.12}$$

Plotting V_{OC} against ln (J_{SC}) over a range of different irradiance values should yield a straight line, the intercept of which, allows for the determination of the reverse saturation current density, J_0. Representative *J-V* characteristics for the glass / ITO / PEIE / P3HT:ICBA / MoO_3 / Ag photodetector under varying irradiance at a temperature of 320 K are shown in Figure 5.8.

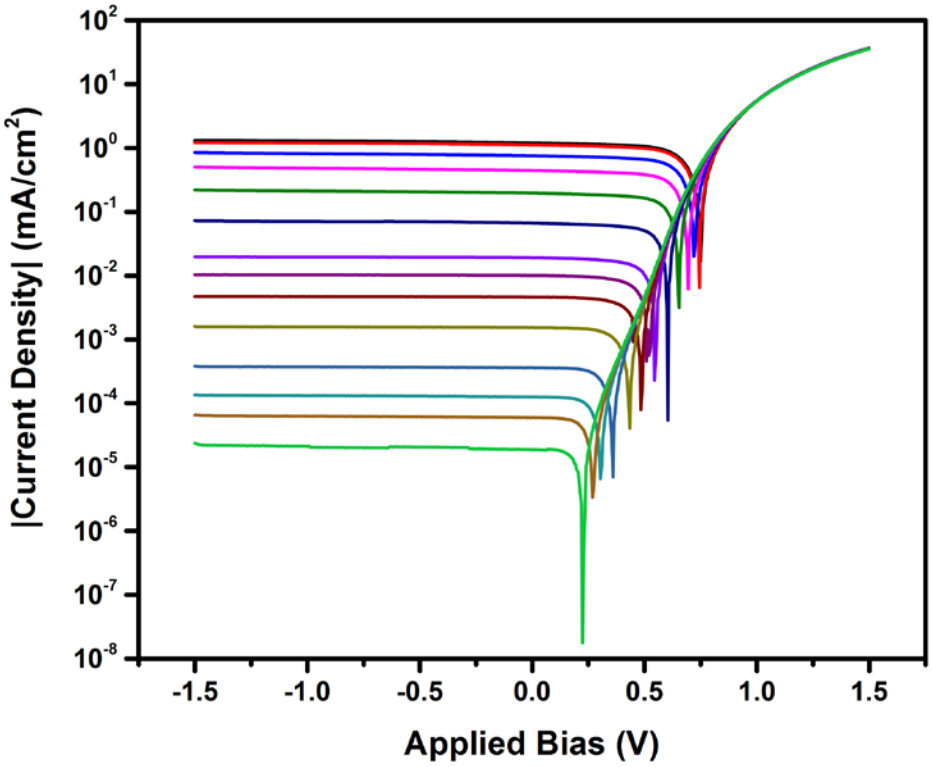

Figure 5.8. Representative *J–V* characteristics under varying irradiance at a temperature of 320 K for the glass / ITO / PEIE / P3HT:ICBA / MoO_3 / Ag photodetector.

Similar *J-V* characteristics for T = 200, 260, 297, 340, and 360 K are shown in Appendix A.

The V_{OC}-J_{SC} plots for all six temperature points are shown together in Figure 5.9. The (V_{OC}, J_{SC}) points fall on a straight line on the semi-logarithmic scale as predicted by the equivalent circuit model with assumptions.

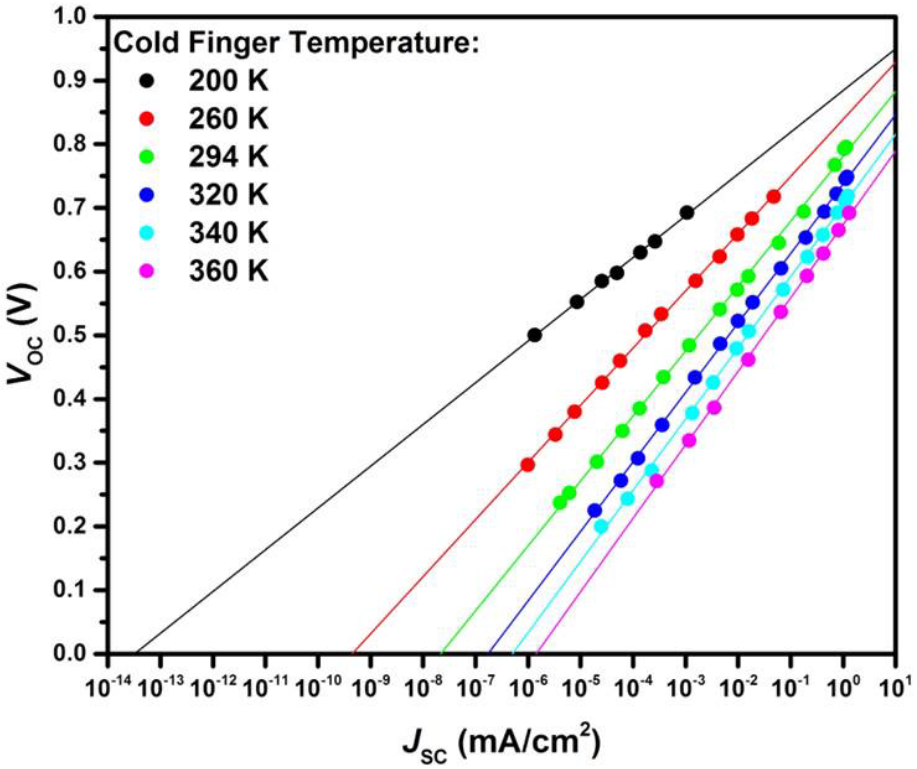

Figure 5.9. Open-circuit voltage plotted against the short-circuit current density on a semilogarithmic scale as obtained via electrical characterization under variable irradiance and temperature for the glass / ITO / PEIE / P3HT:ICBA / MoO_3 / Ag photodetector.

The reverse saturation current density, J_0, for each temperature can be read off by extrapolating the exponential fits of the data to the J_{SC} axis. J_0 varies over 8 orders of magnitude in the range of temperature over which measurements were made, since its origin is a thermally activated process.

Plotting the J_0 values for each temperature against inverse temperature on a semilogarithmic scale allowed for the energy barrier for thermal activation, ϕ_B, to be extracted, as shown in Figure 5.10.

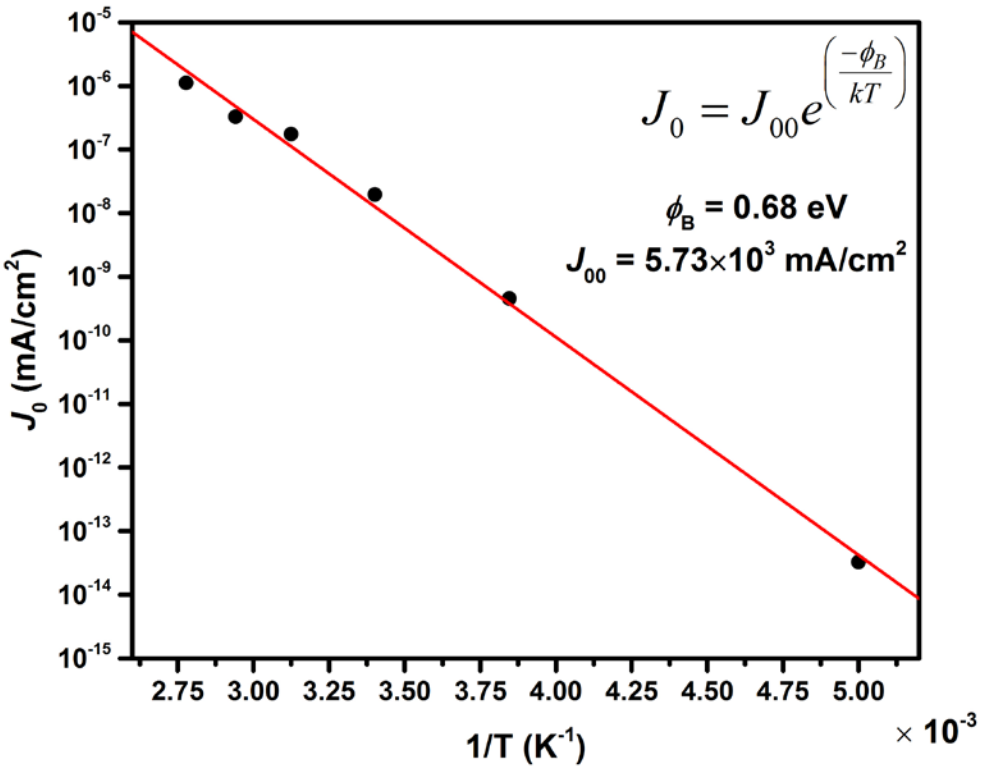

Figure 5.10. Reverse saturation current density as a function of inverse temperature on a semilogarithmic scale for the glass / ITO / PEIE / P3HT:ICBA / MoO_3 / Ag photodetector.

The extracted energy barrier height ϕ_B = 0.68 eV was then compared to the value of the energy of the charge transfer state, as obtained in the sub-band gap region in the EQE spectrum.

5.5.4 Measuring the Energy of the Charge-Transfer State

The energy of the charge-transfer state formed between the donor and acceptor can be determined by performing a Gaussian peak decomposition of the reduced external quantum efficiency (EQE) spectrum plotted on a semilogarithmic scale against incident photon energy [80]. The Gaussian peak centered at the lowest energy can be fit to the following equation derived from Marcus theory [81, 82]:

$$EQE(h\nu)\times h\nu = \frac{f}{\sqrt{4\pi\lambda kT}}\exp\left(-\frac{\left[E_{\mathrm{CT}}+\lambda-h\nu\right]^2}{4\lambda kT}\right) \qquad (5.14)$$

where *EQE* is the external quantum efficiency, $h\nu$ is the incident photon energy, f is a parameter related to the strength of the interaction between donor and acceptor, E_{CT} is the energy of the charge-transfer state, λ is the reorganization energy related to the absorption of the charge-transfer state, k is Boltzmann's Constant, and T is the absolute temperature.

A comparison of the Gaussian peak decomposition of reduced EQE spectra for P3HT:ICBA and P3HT:PCBM at an applied bias of 0 V are shown in Figure 5.11.

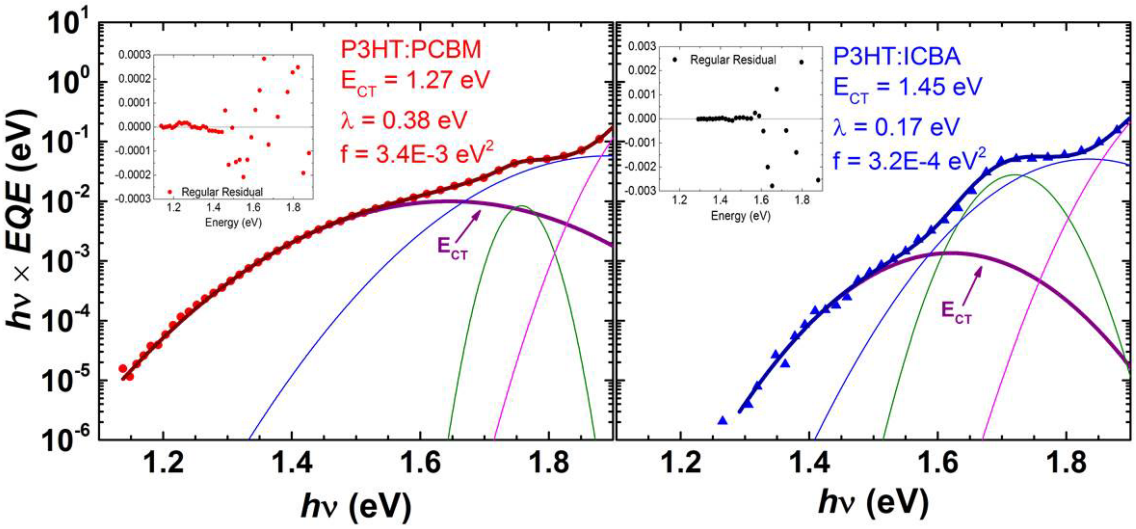

Figure 5.11. Comparison of the charge transfer state energy in P3HT:PCBM and P3HT:ICBA, as obtained by a Gaussian peak decomposition of the sub-band gap absorption region in the reduced EQE spectrum.

From Figure 5.11, the energy of the charge transfer state, E_{CT} (P3HT:ICBA) = 1.45 eV. From the variable temperature and irradiance measurements described in the previous section, the effective barrier energy was calculated to be ϕ_B (P3HT:ICBA) = 0.68 eV. The factor of one-half is consistent with the expression for the intrinsic carrier concentration in a semiconductor:

$$n_i = \sqrt{N_C N_V}\exp\left(-\frac{E_G}{2}\frac{1}{kT}\right) \tag{5.15}$$

where n_i is the intrinsic carrier concentration, N_C is the effective density of states in the conduction band, N_V is the effective density of states in the valence band, E_G is the energy bandgap, k is Boltzmann's Constant and T is temperature.

5.5.5 Dark Current in Photodetectors Based on a Materials System with a Smaller Charge-Transfer State Energy (P3HT:PCBM)

From Figure 5.11, the E_{CT} (and as follows, the V_{OC} under illumination) in P3HT:PCBM devices was smaller than that in P3HT:ICBA. Therefore, the effective energy gap to overcome for the thermal generation of carriers should also be smaller, resulting in a larger reverse saturation current. The dark current measured in an identical device structure but containing PCBM instead of ICBA is shown in Figure 5.12:

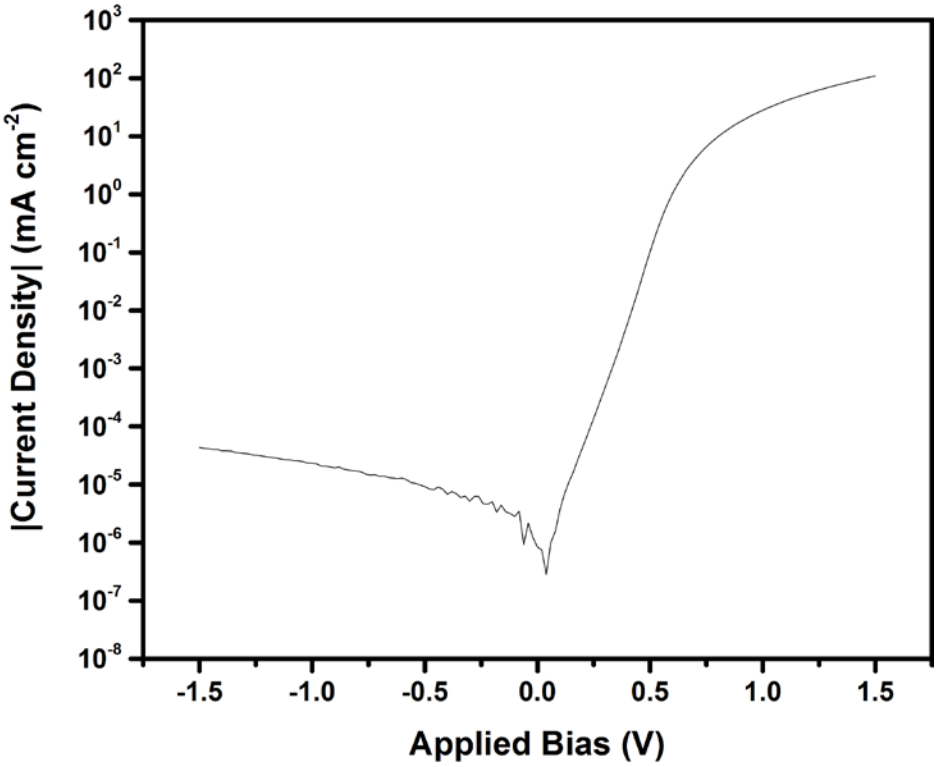

Figure 5.12 *J–V* characteristic in the dark in semilogarithmic scale, for the glass / ITO / PEIE / P3HT:PCBM / MoO_3 / Ag photodetector.

As compared to photodetectors containing P3HT:ICBA, where the average dark current at 0 *V* was 1.1 pA cm^{-2}, the devices containing P3HT:PCBM photoactive layer showed a dark current of 840 pA cm^{-2} at an applied bias of 0 *V*, almost two orders of magnitude higher. A comparison of the open-circuit voltage generated by P3HT:ICBA and P3HT:PCBM-based photodetectors under variable irradiance is shown in Figure 5.13.

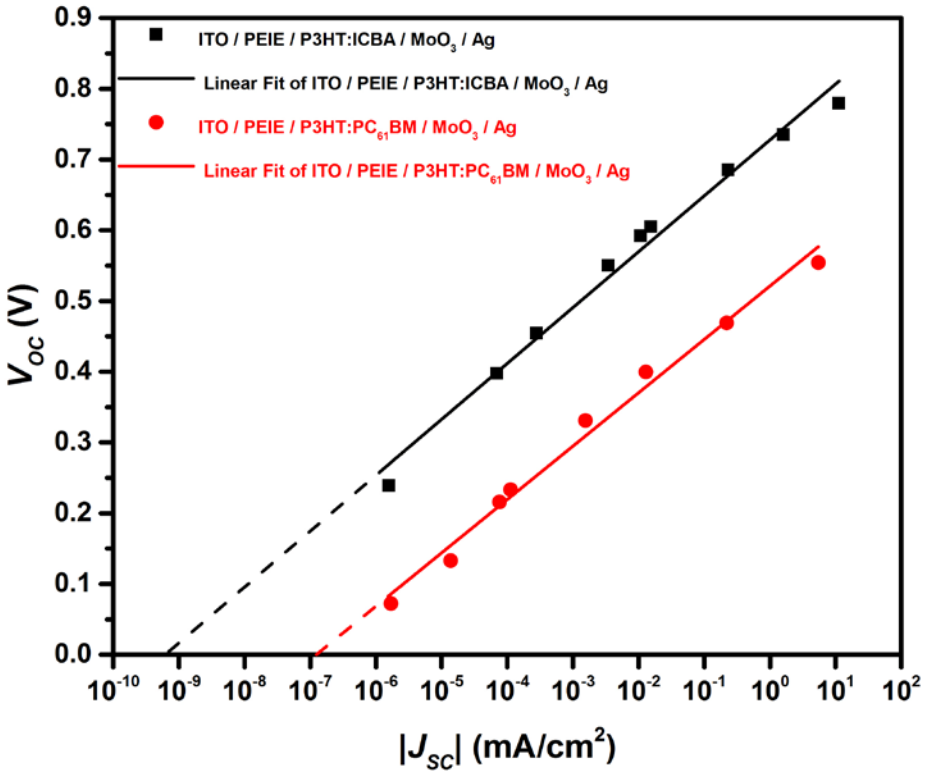

Figure 5.13. Comparison of the open-circuit voltage as a function of irradiance for glass / ITO / PEIE / P3HT:(ICBA or PCBM) / MoO_3 / Ag photodetectors.

For similar irradiance values, P3HT:ICBA-based devices show larger V_{OC} than those containing P3HT:PCBM by virtue of the larger E_{CT} and a smaller J_0 as a result.

5.5.6 Temporal Response in the High Specific Detectivity Photodetectors

An important observation made during the course of the research was the slow temporal response of the detector in response to the application or removal of perturbations, such as a voltage bias. It was found that the amount of time required to reach the steady state varied, depending upon the bias applied, and could even be on the order of tens of minutes for biases close to 0 V, as shown in Figure 5.14.

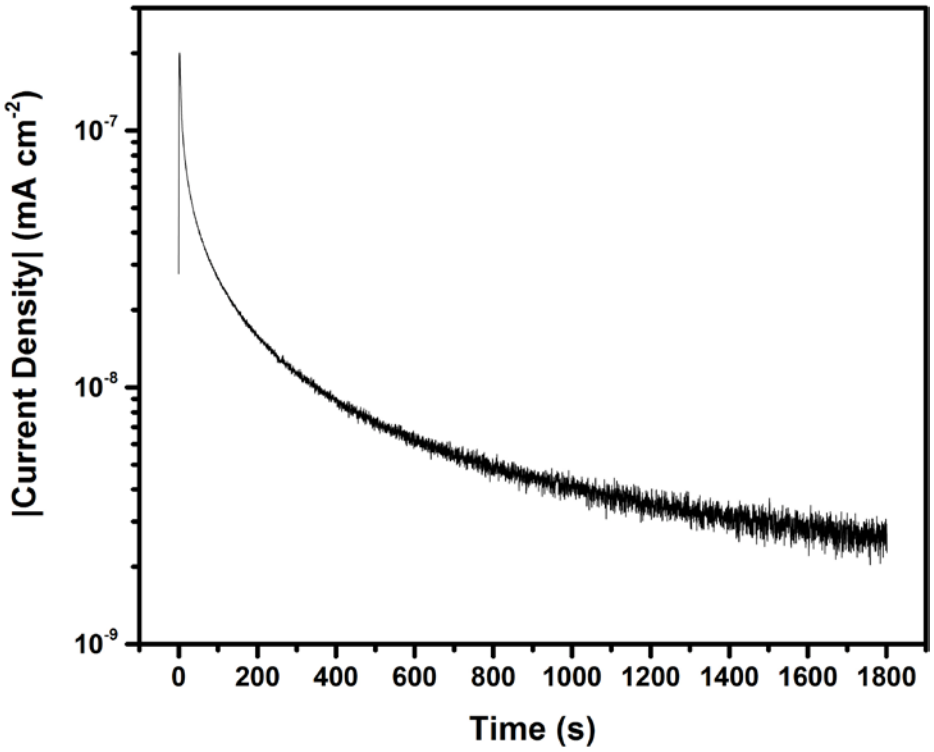

Figure 5.14. Temporal response of the device when a voltage bias of 0 V is applied at time $T = 0$.

An implication of the slow device response to an applied bias, particularly near 0 *V*, was that running an automated voltage sweep where the dwell time between consecutive voltage steps varies between ms to a few s did not record the true steady-state current, as demonstrated in Figure 5.15. Therefore, this work also reveals the importance of allowing sufficient time for the device to reach steady state when characterizing the device, particularly, near 0 V in the dark and around V_{OC} under illumination.

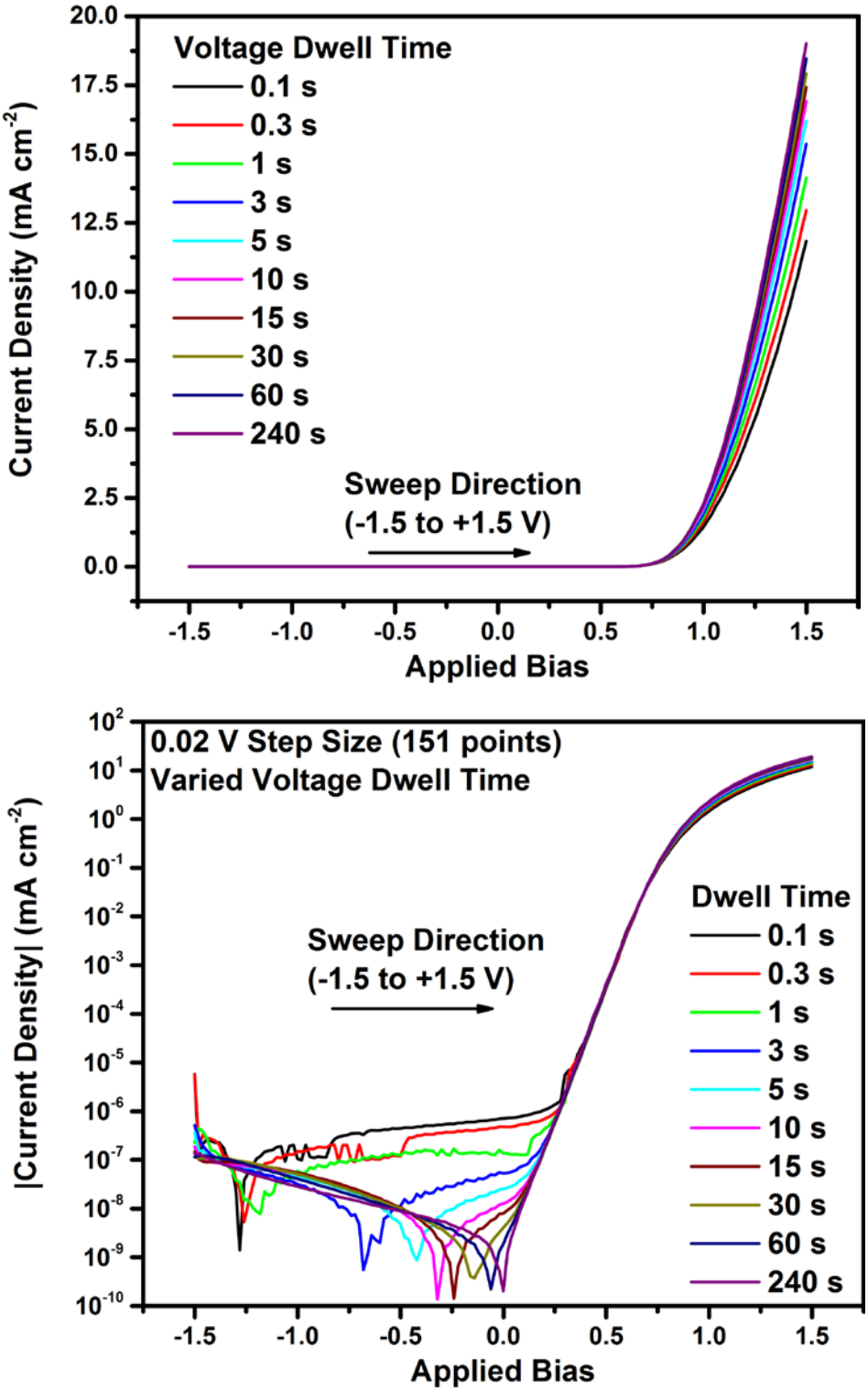

Figure 5.15. Effect of sweep voltage dwell time on the current measured in glass / ITO / PEIE / P3HT:ICBA / MoO_3 / Ag photodetector.

5.5.7 Application of the High Specific Detectivity Detectors to Ionizing Radiation Detection

Finally, the low dark current in the P3HT:ICBA-based photodetectors was exploited in the application of a novel ionizing radiation detection system. The detection of ionizing radiation is a priority for national security, environmental monitoring, and healthcare, among other applications. However, the detection of ionizing radiation is a challenging problem, since the radiation signal decreases with the square of the distance to the source. Conventional systems of ionizing radiation detection typically rely upon scintillators that convert incident radiation into light, which is then detected by a photomultiplier tube (PMT). PMTs are vacuum-tube based devices that operate at high voltage, typically requiring a stable voltage supply of 1 to 2 kV [83]. In addition, PMTs are bulky and expensive ($631 per unit, Model R11194 according to a quote from Hamamatsu Photonics). Therefore, there is a pressing need for large-area low cost ionizing radiation detectors.

Figure 5.16 shows the current measured across the terminals of the detector at an applied bias of 0.1 V as a plutonium-239 radioactive source of activity 3.062 kBq was moved into and out of the line-of-sight of the device. Because of the small penetration depth of the alpha particles through glass, the detector was exposed to the radiation source through the metal electrode side, unlike the previously described case for photodetection applications, in which samples were illuminated through the transparent bottom electrode.

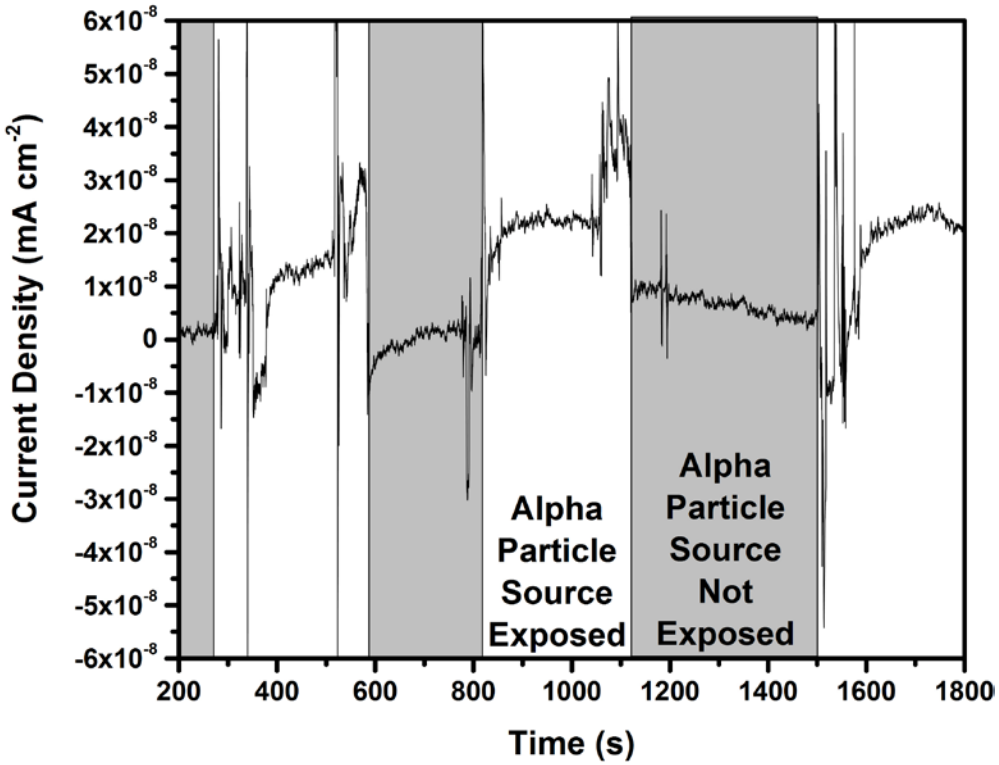

Figure 5.16. Change in current measured upon exposure of a Pu-239 alpha particle source on the glass / ITO / PEIE / P3HT:PCBM / MoO_3 / Ag detector at an applied bias of -0.1 *V*.

A noticeable increase in the current was observed when the radiation source was moved into line of sight of the detector. The current of the detector was on the order of 2×10^{-11} A cm^{-2} when exposed to the alpha particle source and one order of magnitude smaller when unexposed, indicating that the samples were just sensitive enough to detect the ionizing radiation.

5.6 Impact

The work described in this chapter of the dissertation developed a new understanding that guides the design of organic semiconductor photodetectors. The

significance of the interaction between the donor and acceptor components of the photoactive layer in the context of the energy of the charge transfer state was highlighted. In particular, the reverse saturation current was related to the thermal generation of carriers across the effective band gap defined by the energy of the charge transfer state. It was demonstrated that dedicated charge blocking layers at the electrodes were not necessary in photodetector design and that their function was to enhance the shunt resistance, which could also be achieved by increasing the photoactive layer film thickness, optimizing the film drying procedure, and employing electron and hole collecting electrodes with a large work function contrast. The photodetectors developed in this work define the state-of-the-art in terms of the dark current and specific detectivity in organic semiconductor-based photodetectors.

The importance of understanding the temporal response of the device was emphasized, and the pitfalls of collecting data by automated voltage sweeps were underscored.

Lastly, the high specific detectivity photodetectors were employed in a novel application: scintillator-free detectors for ionizing radiation. The development of this could lead to large area, flexible, low cost detectors for ionizing radiation.

CHAPTER 6

CONCLUSIONS AND RECOMMENDATIONS FOR FUTURE WORK

This chapter presents the conclusions that were arrived to during the course of the research described in this dissertation. In addition, some of the directions in which the scope of the performed work can be extended are outlined.

6.1 Conclusions

The world is going through an energy revolution. It is becoming increasingly clear that the conventional fossil fuel-based means of energy generation are not sustainable. Within this very decade, the amount of energy generated by means of solar photovoltaics has grown by over 3500%. Although crystalline silicon-based solar cells have been carrying the banner for photovoltaics on the commercial scale, organic semiconductor-based photovoltaic cells, with their potential to become a disruptive technology, have become a topic of great interest in academic research. As is the case for any emerging technology, organic solar cells also face challenges that researchers are diligently working to address.

Chapter 4 of this dissertation contained details of the approach implemented to tackle the environmental instability of organic solar cells in air as imparted by the degradation of the electrodes. Calcium, although widely used as the electron-collecting electrode in high efficiency organic solar cells because of its low work function, is particularly unstable because of its proclivity to react in air to form calcium oxide.

Through the course of this research, calcium-free organic solar cells were fabricated by creating a low work function interface by means of the non-conjugated aliphatic polymer, polyethylenimine, in conjunction with air stable electrodes, such as, aluminum, silver, and gold. A methodology was developed to deposit polyethylenimine from the solvent 2-methoxyethanol onto the hydrophobic P3HT-based photoactive layer through surface modification by means of a flash of oxygen plasma, allowing the fabrication of devices in the structure glass / ITO / PEDOT:PSS / P3HT:(ICBA or $PC_{61}BM$ or $PC_{71}BM$) / PEIE / (Al or Ag or Au). These devices demonstrated comparable overall power conversion efficiency (4.6% ± 0.3%) to the devices containing unstable calcium electrodes.

Chapter 5 of this dissertation introduced novel design rules for the fabrication of high specific detectivity ($D^* > 10^{14}$ Jones) organic photodetectors, as inspired from organic photovoltaics. As opposed to the conventional approach of using so-called charge blocking layers to reduce the current in the dark under reverse bias, the judicious choice of donor and acceptor materials with large charge-transfer state energy, in conjunction with the optimization of processing to yield devices with high shunt resistance, were identified as being critical to the fabrication of photodetectors with high specific detectivity of 1.25×10^{14} Jones. The charge transfer state energy, as measured by sub-band gap absorption, was identified as the effective gap for the thermal generation of carriers that leads to the reverse saturation current. Finally, the devices were successfully implemented in a novel application as scintillator-free detectors for ionizing radiation.

6.2 Recommendations for Future Work

The scope of the work presented in this dissertation can be extended in a number of directions to further elucidate physical mechanisms occurring within the organic semiconductor devices, in addition to targeting new applications.

6.2.1 Studying the Nature of the Interactions of PEIE with P3HT and Fullerenes

Calcium-free organic solar cells were developed by coating polyethylenimine on top of the P3HT:(ICBA or $PC_{61}BM$ or $PC_{71}BM$) photoactive layers. In addition to the reduction of the work function of the metals coated atop PEIE, previous reports have shown that PEIE dopes the fullerene material [58]. Other reports have also shown that PEIE can be mixed within the bulk of the photoactive layer to produce a low work function interface due to vertical phase separation [84]. Therefore, more studies on the exact nature of the interaction between PEIE and the organic semiconductor components, including if any, with P3HT, would be beneficial.

6.2.2 Development of Calcium-Free Conventional Geometry Devices using High Efficiency Materials Systems

In this work, calcium-free OPV were demonstrated using prototypical P3HT-based photoactive layers. Because of the energetics of P3HT [85], the short circuit current density in P3HT-based OPV systems is limited to around 10 mA/cm^2 under one sun illumination. New generations of high efficiency polymers, such as donor-acceptor polymers, have led to OPV with short-circuit current density values around 20 mA/cm^2

[86]. A possible extension of this work is to develop calcium-free conventional geometry OPV using new polymer systems.

6.2.3 Understanding Device Dynamics in P3HT:ICBA-based Diodes

One of the observations in the P3HT:ICBA-based photodetector samples was a slow response to a change in applied bias or the removal of illumination. Measuring and modeling the time constants for the change in current as a function of time could provide insight into the behavior of charge carriers, particularly in the context of the filling of deep traps. Studying the time constants as a function of temperature would also add to the understanding of the dynamics.

Since ICBA is a mixture of isomers, one hypothesis for the slow dynamics is a high level of disorder between P3HT and the fullerene molecules. Many research groups have also developed single isomer versions of ICBA [87] that would be interesting to study in the context of dynamics.

6.2.4 Measuring the Dark Current in P3HT:ICBA-based Diodes at Low Temperature in the Cryostat

The dark current measured in P3HT:ICBA-based diodes was at the detection limit of the equipment currently available. The design of a new characterization set up with better shielding would be necessary in order to accurately record the current with tighter error bars. For variable temperature measurements conducted inside the cryostat, the noise introduced by the resistive heater cables was masking the sub-pA level of current.

Therefore, the design of a low noise system for the accurate characterization of sub-pA current is essential to extend the photodetector work.

6.2.5 Incorporating the Photodetector into an Imaging Array

From a practical applications standpoint, the next logical step in the development of the low leakage current photodetectors would be the incorporation into an imaging array. For the imaging array, a detailed study on the uniformity of the P3HT:ICBA films across the sample will become important.

6.2.6 High Specific Detectivity Photodetectors with Response in the Near-Infrared

The high detectivity photodetectors developed in this work operate in the visible wavelength range by virtue of the absorption profile of the polymer, P3HT. By employing polymers with a narrower bandgap than P3HT, high detectivity photodetectors that sense infrared radiation can be developed for other applications.

6.2.7 Discrimination of Detected Ionizing Radiation

The work involving the application of organic diodes as scintillator-free detectors of ionizing radiation can be expanded by discriminating the source of the ionizing radiation. While Pu-239 was used as the alpha-particle source, gamma radiation is usually ejected in addition to the alpha particles. Therefore, it would be instructive to determine the nature of the radiation being sensed. In addition, the mechanism of the increase in current in the detector when exposed to ionizing radiation should be clarified in future studies.

APPENDIX A

VARIABLE IRRADIANCE AND TEMPERATURE CURRENT DENSITY - VOLTAGE SCANS FOR THE PHOTODETECTORS

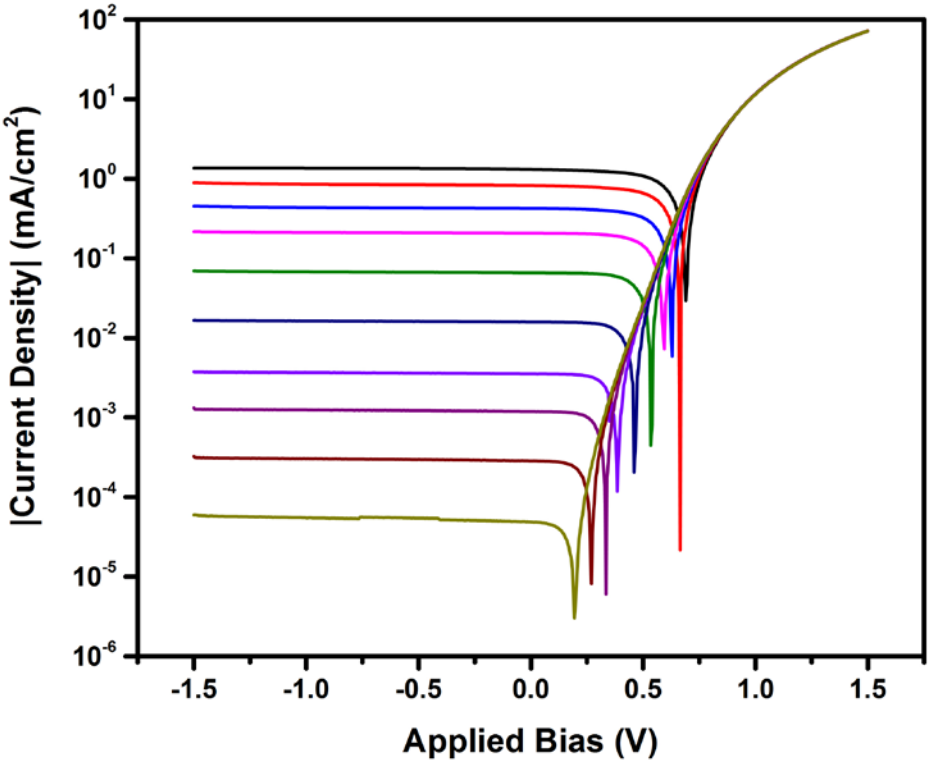

Figure A.1. Representative *J–V* characteristics under varying irradiance at a temperature of 360 K for the glass / ITO / PEIE / P3HT:ICBA / MoO_3 / Ag photodetector.

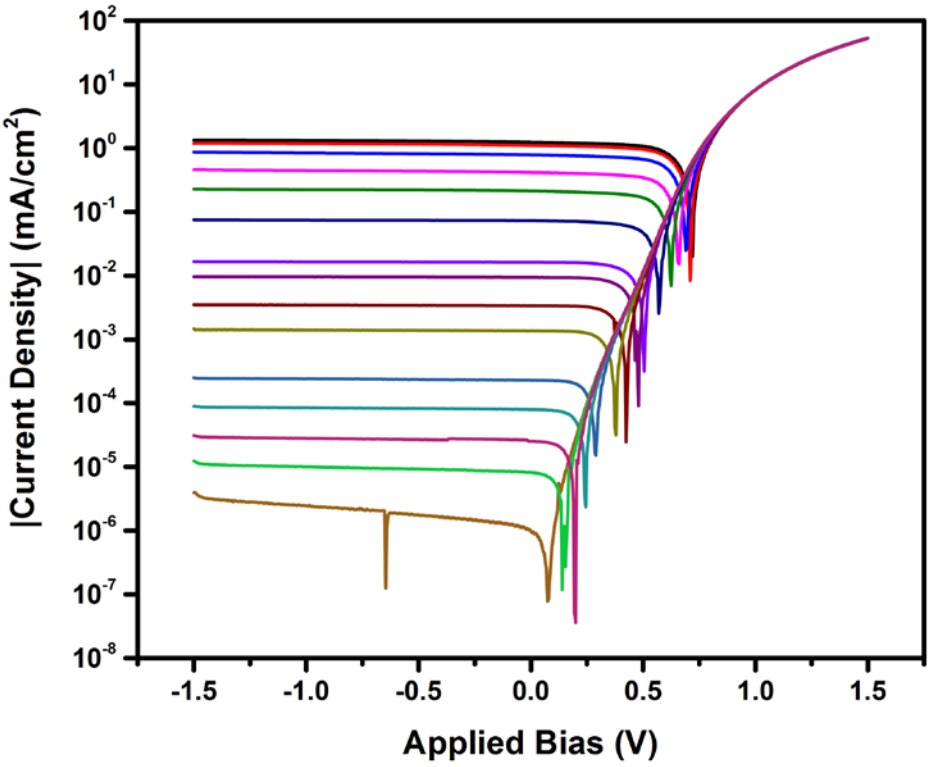

Figure A.3. Representative *J–V* characteristics under varying irradiance at a temperature of 340 K for the glass / ITO / PEIE / P3HT:ICBA / MoO_3 / Ag photodetector.

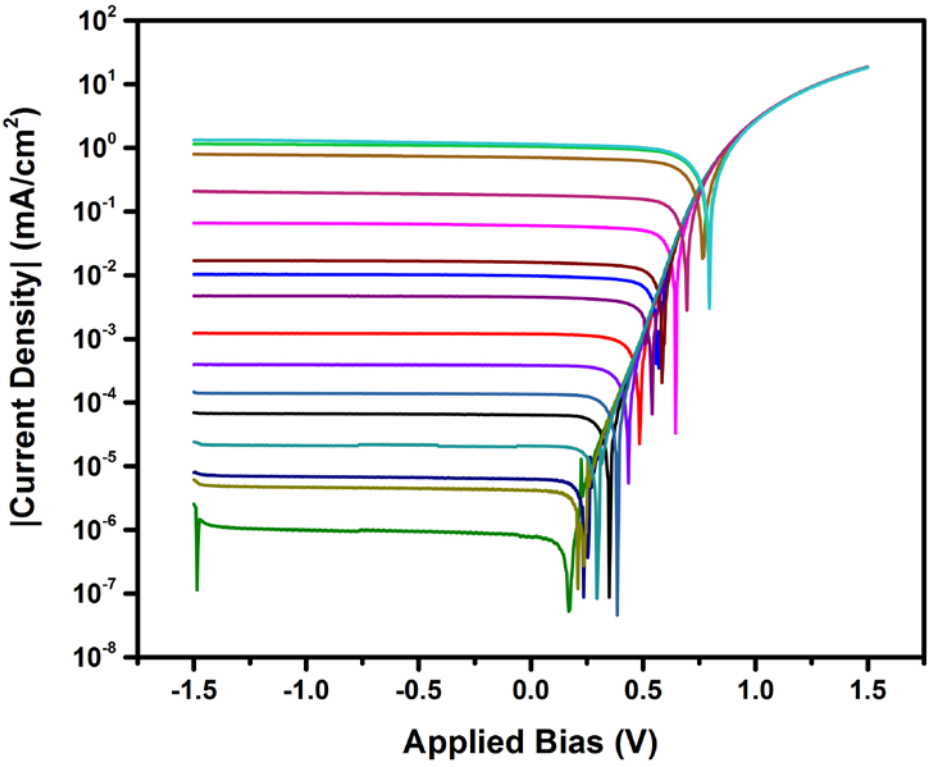

Figure A.4. Representative *J–V* characteristics under varying irradiance at a temperature of 294 K for the glass / ITO / PEIE / P3HT:ICBA / MoO_3 / Ag photodetector.

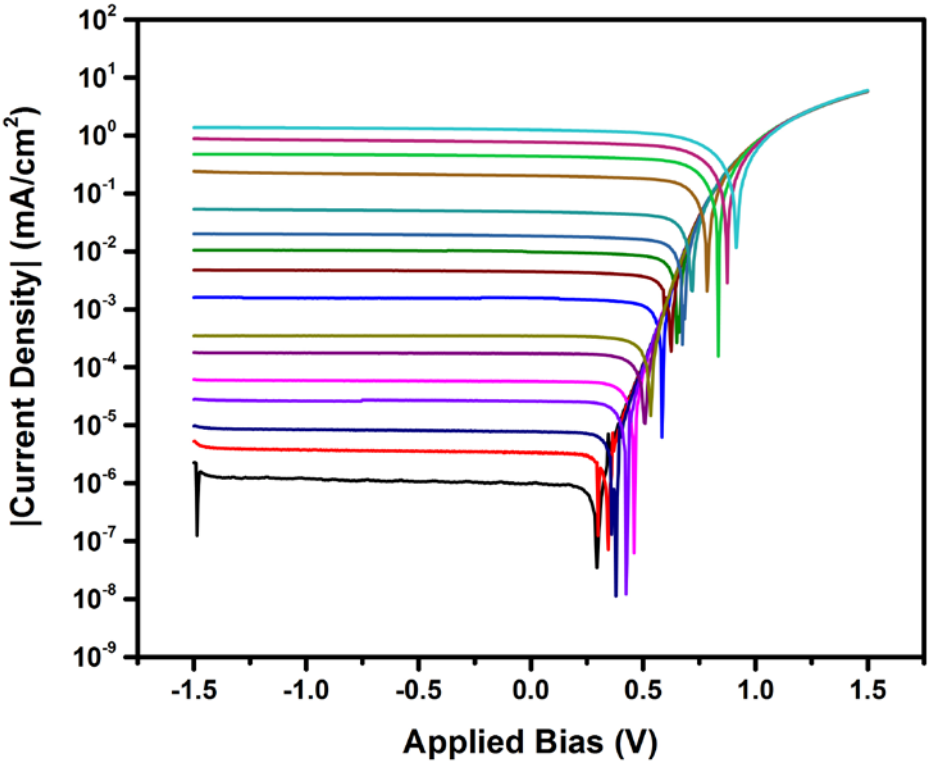

Figure A.5. Representative *J–V* characteristics under varying irradiance at a temperature of 260 K for the glass / ITO / PEIE / P3HT:ICBA / MoO_3 / Ag photodetector.

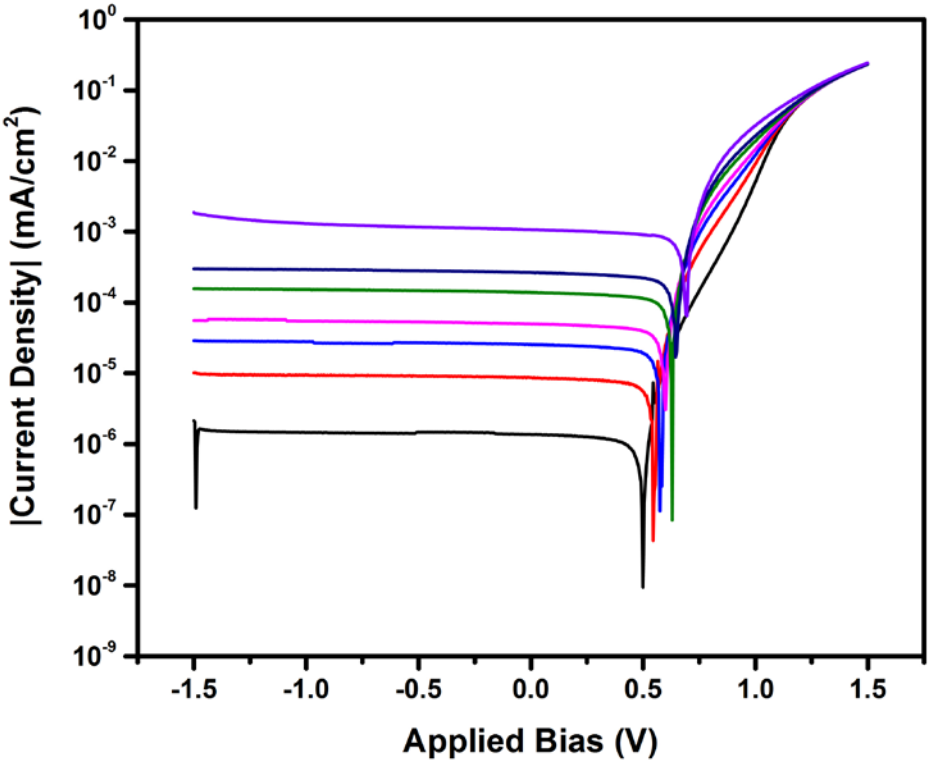

Figure A.5. Representative *J–V* characteristics under varying irradiance at a temperature of 200 K for the glass / ITO / PEIE / P3HT:ICBA / MoO_3 / Ag photodetector.

REFERENCES

[1] R. Hankey, "Electric Power Monthly with Data for December 2015," US Energy Information Administration, 2016.

[2] "DRAFT Inventory of U.S. Greenhouse Gas Emissions and Sinks: 1990-2014," U.S. Environmental Protection Agency EPA 430-R-16-002, 2016.

[3] N. R. E. Laboratory. (2016, 02/27/2016). *Best Research-Cell Efficiencies*. Available: http://www.nrel.gov/ncpv/images/efficiency_chart.jpg

[4] "Photovoltaics Report," Fraunhofer Institute for Solar Energy Systems, ISE11/17/2015 2015.

[5] H. Hoppe and N. S. Sariciftci, "Organic solar cells: An overview," *Journal of Materials Research,* vol. 19, pp. 1924-1945 (2004).

[6] A. E. Becquerel, "Mémoire sur les effets électriques produits sous l'influence des rayons solaires," *Comptes Rendus des Séances Hebdomadaires,* vol. 9, pp. 561-567 (1839).

[7] A. T. Vartanyan, "Photoconductivity of Thin Films of Organic Dyes In The Solid State," *Zhurnal Fizicheskoy Khimii,* vol. 20, pp. 1065-1080 (1946).

[8] D. D. Eley, "Phthalocyanines as Semiconductors," *Nature,* vol. 162, p. 819 (1948).

[9] H. Akamatu and H. Inokuchi, "On the Electrical Conductivity of Violanthrone, Iso-Violanthrone, and Pyranthrone," *The Journal of Chemical Physics,* vol. 18, pp. 810-811 (1950).

[10] D. M. Chapin, C. S. Fuller, and G. L. Pearson, "A New Silicon p-n Junction Photocell for Converting Solar Radiation into Electrical Power," *Journal of Applied Physics,* vol. 25, pp. 676-677 (1954).

[11] H. Inokuchi, Y. Maruyama, and H. Akamatu, "The Photovoltaic Behavior in Organic Compounds," *Bulletin of the Chemical Society of Japan,* vol. 34, pp. 1093-1096 (1961).

[12] L. E. Lyons and O. M. G. Newman, "Photovoltages In Tetracene Films," *Australian Journal of Chemistry,* vol. 24, p. 13 (1971).

[13] A. K. Ghosh and T. Feng, "Rectification, Space-Charge-Limited Current, Photovoltaic And Photoconductive Properties Of Al-Tetracene-Au Sandwich Cell," *Journal of Applied Physics,* vol. 44, pp. 2781-2788 (1973).

[14] A. K. Ghosh, D. L. Morel, T. Feng, R. F. Shaw, and C. A. Rowe, "Photovoltaic and rectification properties of Al/Mg phthalocyanine/Ag Schottky-barrier cells," *Journal of Applied Physics,* vol. 45, pp. 230-236 (1974).

[15] C. W. Tang and A. C. Albrecht, "Chlorophyll-A Photovoltaic Cells," *Nature,* vol. 254, pp. 507-509 (1975).

[16] C. W. Tang and A. C. Albrecht, "Photovoltaic Effects of Metal-Chlorophyll-A-Metal Sandwich Cells," *Journal of Chemical Physics,* vol. 62, pp. 2139-2149 (1975).

[17] C. W. Tang and A. C. Albrecht, "Transient Photovoltaic Effects In Metal-Chlorophyll-A-Metal Sandwich Cells," *Journal of Chemical Physics,* vol. 63, pp. 953-961 (1975).

[18] V. Y. Merritt and H. J. Hovel, "Organic Solar-Cells of Hydroxy Squarylium," *Applied Physics Letters,* vol. 29, pp. 414-415 (1976).

[19] F. J. Kampas and M. Gouterman, "Porphyrin Films .3. Photovoltaic Properties of Octaethylporphine and Tetraphenylporphine," *Journal of Physical Chemistry,* vol. 81, pp. 690-695 (1977).

[20] F. R. Fan and L. R. Faulkner, "Photo-Voltaic Effects of Metal-Free And Zinc Phthalocyanines .2. Properties of Illuminated Thin-Film Cells," *Journal of Chemical Physics,* vol. 69, pp. 3341-3349 (1978).

[21] D. L. Morel, A. K. Ghosh, T. Feng, E. L. Stogryn, P. E. Purwin, R. F. Shaw, *et al.*, "High-Efficiency Organic Solar-Cells," *Applied Physics Letters,* vol. 32, pp. 495-497 (1978).

[22] D. Kearns and M. Calvin, "Photovoltaic Effect and Photoconductivity in Laminated Organic Systems," *The Journal of Chemical Physics,* vol. 29, pp. 950-951 (1958).

[23] P. J. Reucroft and W. H. Simpson, "Photoelectronic Effects in Organic Materials .I. Chlorophyll-Chloranil Lamellar Systems," *Photochemistry and Photobiology,* vol. 10, pp. 79-86 (1969).

[24] K. Kudo and T. Moriizumi, "Photoelectric p-n-Junction Cells Using Organic-Dyes," *Japanese Journal of Applied Physics,* vol. 20, pp. L553-L556 (1981).

[25] G. A. Chamberlain, "Organic p-n-Junction Solar-Cells," *Molecular Crystals and Liquid Crystals,* vol. 93, pp. 369-379 (1983).

[26] Y. Harima, K. Yamashita, and H. Suzuki, "Spectral Sensitization in an Organic p-n Junction Photovoltaic Cell," *Applied Physics Letters,* vol. 45, pp. 1144-1145 (1984).

[27] C. W. Tang, "2-Layer Organic Photovoltaic Cell," *Applied Physics Letters,* vol. 48, pp. 183-185 (1986).

[28] N. S. Sariciftci, D. Braun, C. Zhang, V. I. Srdanov, A. J. Heeger, G. Stucky, *et al.*, "Semiconducting Polymer-Buckminsterfullerene Heterojunctions: Diodes, Photodiodes, and Photovoltaic cells," *Applied Physics Letters,* vol. 62, pp. 585-587 (1993).

[29] G. Yu, J. Gao, J. C. Hummelen, F. Wudl, and A. J. Heeger, "Polymer Photovoltaic Cells - Enhanced Efficiencies Via A Network of Internal Donor-Acceptor Heterojunctions," *Science,* vol. 270, pp. 1789-1791 (1995).

[30] S. E. Shaheen, C. J. Brabec, N. S. Sariciftci, F. Padinger, T. Fromherz, and J. C. Hummelen, "2.5% Efficient Organic Plastic Solar Cells," *Applied Physics Letters,* vol. 78, pp. 841-843 (2001).

[31] F. Padinger, R. S. Rittberger, and N. S. Sariciftci, "Effects of Postproduction Treatment on Plastic Solar Cells," *Advanced Functional Materials,* vol. 13, pp. 85-88 (2003).

[32] G. Li, V. Shrotriya, Y. Yao, and Y. Yang, "Investigation of Annealing Effects And Film Thickness Dependence Of Polymer Solar Cells Based on Poly(3-hexylthiophene)," *Journal of Applied Physics,* vol. 98, p. 043704 (2005).

[33] W. L. Ma, C. Y. Yang, X. Gong, K. Lee, and A. J. Heeger, "Thermally Stable, Efficient Polymer Solar Cells With Nanoscale Control of The Interpenetrating Network Morphology," *Advanced Functional Materials,* vol. 15, pp. 1617-1622 (2005).

[34] M. D. Irwin, D. B. Buchholz, A. W. Hains, R. P. H. Chang, and T. J. Marks, "p-Type Semiconducting Nickel Oxide as an Efficiency-Enhancing Anode Interfacial Layer in Polymer Bulk-Heterojunction Solar Cells," *Proceedings of the National Academy of Sciences,* vol. 105, pp. 2783-2787 (2008).

[35] S. H. Park, A. Roy, S. Beaupre, S. Cho, N. Coates, J. S. Moon, *et al.*, "Bulk Heterojunction Solar Cells with Internal Quantum Efficiency Approaching 100%," *Nature Photonics,* vol. 3, pp. 297-303 (2009).

[36] N. Blouin, A. Michaud, and M. Leclerc, "A Low-Bandgap Poly(2,7-Carbazole) Derivative for Use in High-Performance Solar Cells," *Advanced Materials,* vol. 19, pp. 2295-2300 (2007).

[37] H. Y. Chen, J. H. Hou, S. Q. Zhang, Y. Y. Liang, G. W. Yang, Y. Yang, *et al.*, "Polymer Solar Cells With Enhanced Open-Circuit Voltage And Efficiency," *Nature Photonics,* vol. 3, pp. 649-653 (2009).

[38] Y. Y. Liang, Z. Xu, J. B. Xia, S. T. Tsai, Y. Wu, G. Li, *et al.*, "For the Bright Future-Bulk Heterojunction Polymer Solar Cells with Power Conversion Efficiency of 7.4%," *Advanced Materials,* vol. 22, pp. E135-E138 (2010).

[39] Z. He, C. Zhong, X. Huang, W.-Y. Wong, H. Wu, L. Chen, *et al.*, "Simultaneous Enhancement of Open-Circuit Voltage, Short-Circuit Current Density, and Fill Factor in Polymer Solar Cells," *Advanced Materials,* vol. 23, pp. 4636-4643 (2011).

[40] Z. He, C. Zhong, S. Su, M. Xu, H. Wu, and Y. Cao, "Enhanced power-conversion efficiency in polymer solar cells using an inverted device structure," *Nature Photonics,* vol. 6, pp. 591-595 (2012).

[41] Y. Liu, J. Zhao, Z. Li, C. Mu, W. Ma, H. Hu, *et al.*, "Aggregation and Morphology Control Enables Multiple Cases of High-Efficiency Polymer Solar Cells," *Nature Communications,* vol. 5, article 5293 (2014).

[42] "Heliatek Sets New Organic Photovoltaic World Record Efficiency of 13.2%," ed. Dresden, Germany, 2016. Available: http://www.heliatek.com/en/press/press-releases/details/heliatek-sets-new-organic-photovoltaic-world-record-efficiency-of-13-2

[43] T. W. G. Solomons and C. B. Fryhe, *Organic Chemistry*. Asia: John Wiley & Sons (Asia) Pte. Ltd. (2011).

[44] (02/27/2016). *Center for Materials and Devices for Information Technology Research (CMDITR) Photonics Wiki*. Available: photonicswiki.org/images/f/fa/Ethylene_energy.jpg

[45] J.-L. Brédas, J. Cornil, and A. J. Heeger, "The Exciton Binding Energy In Luminescent Conjugated Polymers," *Advanced Materials,* vol. 8, pp. 447-452 (1996).

[46] R. F. Pierret, *Semiconductor Device Fundamentals*. India: Dorling Kindersley (India) Pvt. Ltd. (2006).

[47] P. Wurfel, *Physics of Solar Cells: From Basic Principles to Advanced Concepts*. Weinheim, Germany: Wiley-VCH Verlag GmbH & Co. KGaA (2009).

[48] M. A. Green, *Solar Cells: Operating Principles, Technology and System Applications*. Kensington, NSW, Australia: The University of New South Wales (1998).

[49] (02/27/2016). *Reference Solar Spectral Irradiance: ASTM G-173*. Available: http://rredc.nrel.gov/solar/spectra/am1.5/ASTMG173/ASTMG173.html

[50] Y. H. Zhou, J. W. Shim, C. Fuentes-Hernandez, A. Sharma, K. A. Knauer, A. J. Giordano, *et al.*, "Direct Correlation Between Work Function of Indium-Tin-Oxide Electrodes And Solar Cell Performance Influenced by Ultraviolet Irradiation And Air Exposure," *Physical Chemistry Chemical Physics*, vol. 14, pp. 12014-12021 (2012).

[51] H. Cheun, C. Fuentes-Hernandez, Y. Zhou, W. J. Potscavage, S.-J. Kim, J. Shim, *et al.*, "Electrical and Optical Properties of ZnO Processed by Atomic Layer Deposition in Inverted Polymer Solar Cells," *The Journal of Physical Chemistry C*, vol. 114, pp. 20713-20718 (2010).

[52] S. Yoo, B. Domercq, and B. Kippelen, "Efficient Thin-Film Organic Solar Cells Based on Pentacene/C-60 Heterojunctions," *Applied Physics Letters*, vol. 85, pp. 5427-5429 (2004).

[53] N. D. Treat and M. L. Chabinyc, "Phase Separation in Bulk Heterojunctions of Semiconducting Polymers and Fullerenes for Photovoltaics," *Annual Review of Physical Chemistry*, vol. 65, pp. 59-81 (2014).

[54] M. B. Prince, "Silicon Solar Energy Converters," *Journal of Applied Physics*, vol. 26, pp. 534-540 (1955).

[55] (02/27/2016). *Spectroscopic Ellipsometry Tutorial Optical Constants - J. A. Woollam Co.* Available: http://www.jawoollam.com/tutorial_7.html

[56] E. A. Mechtly, "4 - Properties of Materials A2 - Valkenburg, Wendy M. MiddletonMac E. Van," in *Reference Data for Engineers (Ninth Edition)*, ed Woburn: Newnes, 2002, pp. 4-5.

[57] J. A. Dobrowolski, Coatings and Filters. In *Handbook of Optics*; Driscoll, W. G.; Vaughan, W., Eds.; McGraw-Hill: New York, 1978; p. 92.

[58] Y. H. Zhou, C. Fuentes-Hernandez, J. Shim, J. Meyer, A. J. Giordano, H. Li, *et al.*, "A Universal Method to Produce Low-Work Function Electrodes for Organic Electronics," *Science*, vol. 336, pp. 327-332 (2012).

[59] T. M. Khan, Y. Zhou, A. Dindar, J. W. Shim, C. Fuentes-Hernandez, and B. Kippelen, "Organic Photovoltaic Cells with Stable Top Metal Electrodes Modified with Polyethylenimine," *ACS Applied Materials & Interfaces*, vol. 6, pp. 6202–6207 (2014).

[60] G. Zhao, Y. He, and Y. Li, "6.5% Efficiency of Polymer Solar Cells Based on Poly(3-hexylthiophene) and Indene-C_{60} Bisadduct by Device Optimization," *Advanced Materials,* vol. 22, pp. 4355-4358 (2010).

[61] Z. Kai, H. Zhicheng, D. Chunhui, Y. Lei, H. Fei, and C. Yong, "The Effect Of Methanol Treatment on The Performance of Polymer Solar Cells," *Nanotechnology,* vol. 24, p. 484003 (2013).

[62] X. Liu, W. Wen, and G. C. Bazan, "Post-Deposition Treatment of an Arylated-Carbazole Conjugated Polymer for Solar Cell Fabrication," *Advanced Materials,* vol. 24, pp. 4505-4510 (2012).

[63] S. Nam, J. Jang, H. Cha, J. Hwang, T. K. An, S. Park, *et al.*, "Effects of Direct Solvent Exposure on The Nanoscale Morphologies And Electrical Characteristics Of PCBM-Based Transistors And Photovoltaics," *Journal of Materials Chemistry,* vol. 22, pp. 5543-5549 (2012).

[64] O. Synooka, F. Kretschmer, M. D. Hager, U. Schubert, G. Gobsch, and H. Hoppe, "Impact of Methanol Top-Casting or Washing on The Polymer Solar Cell Performance," *Proceedings of SPIE,* vol. 8811, pp. 881117-1 - 881117-7 (2013).

[65] Y. Wang, Y. Liu, S. Chen, R. Peng, and Z. Ge, "Significant Enhancement of Polymer Solar Cell Performance via Side-Chain Engineering and Simple Solvent Treatment," *Chemistry of Materials,* vol. 25, pp. 3196-3204 (2013).

[66] B.-W. Yang, M.-Y. Tsai, W.-H. Cheng, J.-S. Chen, S. L.-C. Hsu, and W.-Y. Chou, "Synergistic Amplification of Short-Circuit Current for Organic Solar Cells via Modulation of P3HT:PCBM Spatial Distribution with Solvent Treatment," *The Journal of Physical Chemistry C,* vol. 117, pp. 14472-14478 (2013).

[67] H. Zhou, Y. Zhang, J. Seifter, S. D. Collins, C. Luo, G. C. Bazan, *et al.*, "High-Efficiency Polymer Solar Cells Enhanced by Solvent Treatment," *Advanced Materials,* vol. 25, pp. 1646-1652 (2013).

[68] Z.-L. Guan, J. Bok Kim, Y.-L. Loo, and A. Kahn, "Electronic Structure of The Poly(3-hexylthiophene):indene-C60 Bisadduct Bulk Heterojunction," *Journal of Applied Physics,* vol. 110, p. 043719 (2011).

[69] K. M. Knesting, H. Ju, C. W. Schlenker, A. J. Giordano, A. Garcia, O. N. L. Smith, *et al.*, "ITO Interface Modifiers Can Improve VOC in Polymer Solar Cells and Suppress Surface Recombination," *The Journal of Physical Chemistry Letters,* vol. 4, pp. 4038-4044 (2013).

[70] A. Dindar, "Microfabrication of Organic Electronic Devices: Organic Photovoltaic Module with High Total-Area Efficiency," Doctor of Philosophy

Dissertation, School of Electrical and Computer Engineering, Georgia Institute of Technology (2015).

[71] H. Zhang, H. Azimi, Y. Hou, T. Ameri, T. Przybilla, E. Spiecker, *et al.*, "Improved High-Efficiency Perovskite Planar Heterojunction Solar Cells via Incorporation of a Polyelectrolyte Interlayer," *Chemistry of Materials,* vol. 26, pp. 5190-5193 (2014).

[72] X. Gong, M. Tong, Y. Xia, W. Cai, J. S. Moon, Y. Cao, *et al.*, "High-Detectivity Polymer Photodetectors with Spectral Response from 300 nm to 1450 nm," *Science,* vol. 325, pp. 1665-1667 (2009).

[73] X. Gong, M.-H. Tong, S. H. Park, M. Liu, A. Jen, and A. J. Heeger, "Semiconducting Polymer Photodetectors with Electron and Hole Blocking Layers: High Detectivity in the Near-Infrared," *Sensors,* vol. 10, p. 6488 (2010).

[74] T. Drori, C. X. Sheng, A. Ndobe, S. Singh, J. Holt, and Z. V. Vardeny, "Below-Gap Excitation of pi-Conjugated Polymer-Fullerene Blends: Implications for Bulk Organic Heterojunction Solar Cells," *Physical Review Letters,* vol. 101, p. 037401 (2008).

[75] Y. Zou and R. J. Holmes, "Correlation between the Open-Circuit Voltage and Charge Transfer State Energy in Organic Photovoltaic Cells," *ACS Applied Materials & Interfaces,* vol. 7, pp. 18306-18311 (2015).

[76] Y. Zhou, T. M. Khan, J. W. Shim, A. Dindar, C. Fuentes-Hernandez, and B. Kippelen, "All-Plastic Solar Cells with A High Photovoltaic Dynamic Range," *Journal of Materials Chemistry A,* vol. 2, pp. 3492-3497 (2014).

[77] G. Li, Y. Yao, H. Yang, V. Shrotriya, G. Yang, and Y. Yang, ""“Solvent Annealing” Effect in Polymer Solar Cells Based on Poly(3-hexylthiophene) and Methanofullerenes," *Advanced Functional Materials,* vol. 17, pp. 1636-1644 (2007).

[78] M. Kröger, S. Hamwi, J. Meyer, T. Riedl, W. Kowalsky, and A. Kahn, "Role of the Deep-Lying Electronic States of MoO_3 in The Enhancement Of Hole-Injection in Organic Thin Films," *Applied Physics Letters,* vol. 95, p. 123301 (2009).

[79] W. J. Potscavage, S. Yoo, and B. Kippelen, "Origin of the Open-Circuit Voltage in Multilayer Heterojunction Organic Solar Cells," *Applied Physics Letters,* vol. 93, p. 193308 (2008).

[80] K. Vandewal, A. Gadisa, W. D. Oosterbaan, S. Bertho, F. Banishoeib, I. Van Severen, *et al.*, "The Relation Between Open-Circuit Voltage and the Onset of Photocurrent Generation by Charge-Transfer Absorption in Polymer: Fullerene

Bulk Heterojunction Solar Cells," *Advanced Functional Materials*, vol. 18, pp. 2064-2070 (2008).

[81] I. R. Gould, D. Noukakis, L. Gomezjahn, R. H. Young, J. L. Goodman, and S. Farid, "Radiative And Nonradiative Electron-Transfer In Contact Radical-Ion Pairs," *Chemical Physics*, vol. 176, pp. 439-456 (1993).

[82] R. A. Marcus, "Relation Between Charge-Transfer Absorption And Fluorescence-Spectra And The Inverted Region," *Journal of Physical Chemistry*, vol. 93, pp. 3078-3086 (1989).

[83] "Photomultiplier Tubes: Basics and Applications, Third Edition (Edition 3a)," Hamamatsu Photonics (2007). Available: https://www.hamamatsu.com/resources/pdf/etd/PMT_handbook_v3aE.pdf

[84] H. Kang, J. Lee, S. Jung, K. Yu, S. Kwon, S. Hong, *et al.*, "Self-Assembly of Interfacial and Photoactive Layers Via One-Step Solution Processing for Efficient Inverted Organic Solar Cells," *Nanoscale*, vol. 5, pp. 11587-11591 (2013).

[85] Z.-L. Guan, J. B. Kim, H. Wang, C. Jaye, D. A. Fischer, Y.-L. Loo, *et al.*, "Direct Determination of The Electronic Structure of the Poly(3-hexylthiophene):phenyl-[6,6]-C61 Butyric Acid Methyl Ester Blend," *Organic Electronics*, vol. 11, pp. 1779-1785 (2010).

[86] J. Zhao, Y. Li, G. Yang, K. Jiang, H. Lin, H. Ade, *et al.*, "Efficient Organic Solar Cells Processed From Hydrocarbon Solvents," *Nature Energy*, vol. 1, p. 15027 (2016).

[87] W. W. H. Wong, J. Subbiah, J. M. White, H. Seyler, B. L. Zhang, D. J. Jones, *et al.*, "Single Isomer of Indene-C-70 Bisadduct-Isolation and Performance in Bulk Heterojunction Solar Cells," *Chemistry of Materials*, vol. 26, p. 1686 (2014).

VITA

TALHA M. KHAN

Talha Khan was born in Lahore, Pakistan, on November 03, 1986. He completed his secondary education in Rawalpindi, Pakistan at the Roots School System. This was followed by the attainment of the Bachelor of Science degree in Electrical Engineering, with Highest Honor and the Cooperative Plan designation, from the Georgia Institute of Technology, Atlanta, Georgia, in 2009. As part of the Cooperative Education Program, he completed four semester-long rotations as a Systems Test Engineer in the Design Verification and Qualification group at EG Technology (later acquired by ARRIS Group Inc.). In May 2011, he received the Master of Science degree in Electrical and Computer Engineering, also at Georgia Tech. He has recently accepted an engineering position at Intel Corporation in Aloha, OR. When he is not working on his research, Mr. Khan enjoys watching cricket and spending time with his family and cat Marjorie.